INVESTIGATION OF PROPAGATING FRACTURES WITH SHEAR AND NORMAL STRESSES USING LOW-FREQUENCY DISTRIBUTED ACOUSTIC SENSING

A Thesis

by

TERESA REID

Submitted to the Graduate and Professional School of
Texas A&M University
in partial fulfillment of the requirements for the degree of

MASTER OF SCIENCE

Chair of Committee,	Ding Zhu
Co-Chair of Committee,	Alfred Dan Hill
Committee Member,	Hiroko Kitajima
Head of Department,	Akhil Datta-Gupta

May 2023

Major Subject: Petroleum Engineering

ABSTRACT

Low-frequency distributed acoustic sensing (LF-DAS) can be used as a monitoring tool for hydraulic fracture propagation using measured values of strain. To understand subsurface conditions with shear and normal stresses, a laboratory-scale hydraulic fracture experiment was performed to simulate the LF-DAS response to fracture propagation with embedded distributed optical fiber strain sensors. The objectives of this research were to generate hydraulic fractures of known geometry with shear and normal stresses, measure the strain response along distributed fiber sensors embedded in the sample, and use the results to reveal insights of fracture propagation.

The experiment was performed on a uniaxially-compressed, transparent 8-inch cube of epoxy with a radial initial flaw angled to the applied load. Water was injected into the epoxy block to generate a fracture with shear and normal stresses along the plane of the fracture. These experiments used distributed high-definition fiber optic strain sensors with tight spatial resolutions. The measured strains were compared to experiments with a purely normal stress component to understand how the zero-strain method for fracture geometry apply to the studied case when a shear stress on the fracture plane is introduced.

The experimentally acquired strain and strain-rate waterfall plots with shear and normal stresses on the fracture plane exhibit comparable results to the strain responses of purely normal stresses with a narrowing region of extension surrounded by compression as a fracture approached and intersected a fiber optic cable. However, unlike the experiments

with purely normal stresses on the fracture plane, the introduction of a shear stress created an asymmetrical strain signature over the fracture plane. This dominant strain response on one side of the fracture plane suggests the existence of a shear stress on the plane of the fracture.

DEDICATION

This work is dedicated to God, my family, my friends, and my mentors that have helped me get to where I am today.

ACKNOWLEDGEMENTS

I would like to thank my committee chair, Dr. Ding Zhu, and my co-chair of committee, Dr. Dan Hill for all their guidance and accepting me into their prestigious research group. I would also like to thank my committee member, Dr. Kitajima, for her support during my studies. I want to acknowledge Dr. Leggett for all his assistance and mentorship throughout my research. I am also appreciative of Dr. LeBlanc with Halliburton in Houston, Texas for providing the equipment and associated support needed to conduct my experiments. Thanks to Mr. John Maldonado was of much help in the lab preparing for safety and successful execution of the experiments. Special thank you to Jiayue Chen for his hands in the lab to execute my experiments efficiently and successfully.

My fellow graduate students provided me with support and encouraged me throughout my time in graduate school: Tohoko, Carrie, Travis, Yasu, Gongsheng, Lene, Paula, Aishwarya, Greyson, Shohei, and Riten.

I am also thankful to the Texas A&M Society of Petroleum Engineering student chapter for allowing me to be a part of their highly functional and successful officer team during my studies: Kassem, Darian, Nathan, Courtney, Nikki, and Dr. Blasingame.

Thanks also go to the departmental faculty and staff for ensuring I met the graduation requirements and support throughout the course of this research.

Finally, thanks to my parents and my sister for supporting me during this whole journey.

CONTRIBUTORS AND FUNDING SOURCES

Contributors

This work was supervised by a thesis committee consisting of co-advisor Dr. Ding Zhu, co-advisor Dr. Dan Hill of the Harold Vance Petroleum Engineering Department, and Dr. Hiroko Kitajima of the Department of Geology and Geophysics.

Mr. John Maldonado aided in aligning the mill press to drill holes in the epoxy blocks as reviewed in Chapter 2. Jiayue Chen assisted in constructing the samples and conducting the experiments covered in Chapter 2. The fiber sensing equipment was provided by Halliburton as covered in Chapter 2.

All other work conducted for the thesis dissertation was completed by the student independently.

Funding Sources

Graduate study was supported by a fellowship and graduate research assistantship from the College of Engineering and the Harold Vance Department of Petroleum Engineering.

This work was also made possible in part by the Department of Energy under the Austin Chalk/Eagle for Field Laboratory project number DE_DOA-0001722. Its contents are solely the responsibility of the authors and do not necessarily represent the official views of the awarding offices.

TABLE OF CONTENTS

Page

LIST OF FIGURES

Page

LIST OF TABLES

Page

1. INTRODUCTION

The development of petroleum reservoirs depends on understanding the properties of the subsurface. As technology advanced, the energy industry witnessed the rise of unconventional resources. Hydraulic fracturing facilitated the development of unconventional reservoirs possessing extremely low permeability. Nevertheless, much work remains in hydraulic fracturing optimization. At risk in this optimization are the excessive costs associated with reservoir development. Fiber optic technologies provide diagnostic insights into hydraulic fracturing, allowing engineers to optimize hydraulic fracturing and in turn, reservoir development. In fact, low-frequency distributed acoustic sensing (LF-DAS) data has been revealing insights into hydraulically fractured reservoirs.

This chapter starts with describing the importance of diagnostic technologies for completions related to the development of unconventional reservoirs. It also covers an extensive literature review of multistage hydraulic fracturing, LF-DAS and shear-slip movements during hydraulic fracturing. Finally, the motivation and problem statement of this research are addressed.

1.1. Literature Review

LF-DAS is a fiber optic-based diagnostic technique to measure strains along a fiber optic cable during multi-stage hydraulic fracturing operations. This method typically consists of strain measurements from a fiber optic cable positioned within a wellbore offset to a hydraulic fracturing treatment well. A common technique for deploying fiber optic systems involves clamping an encased fiber to the outside of the production casing and

cementing them in place. Recent breakthroughs demonstrated success with disposable or temporary fibers run in the wellbore with wireline. For a comprehensive introduction to LF-DAS, a background on multi-stage hydraulic fracturing and DAS is provided.

1.1.1. Multistage Hydraulic Fracturing

Hydraulic fracturing is a stimulation method for unconventional reservoirs with ultra-low-permeability, usually on the order of hundreds of nanodarcies. This technique unlocked the world of previously uneconomical unconventional reservoirs. The first hydraulic fracturing treatment was performed in Kansas in 1947 as an experiment by Stanolind shown in Figure 1.1 (Smith & Montgomery, 2015).

Figure 1.1 First experimental hydraulic fracturing treatment in Grant County, Kansas by Stanolind in 1947 (Smith & Montgomery, 2015).

Multi-stage hydraulic fracturing has enabled the production from unconventional reservoirs with long horizontal wellbores located in the pay zone of a geologic formation by performing treatments in stages or intervals along the length of the well. Multistage hydraulic fracturing consists of an isolation method between the well and formation, a

fracture initiation method, an isolation method to separate each fracture interval, and the fracture treatment at each interval (Gutierrez et al., 2014). Plug and perf operations are a multi-stage fracturing technique illustrated in Figure 1.2. This approach consists of setting plugs in between intervals (or stages) to isolate each treatment area along the lateral. To begin a stage, a series of wireline guns are run downhole on a wireline cable with a frac plug on the end. The frac plug is set to create a barrier between the previous and current stage. Then, the perforating guns are fired downhole to create an entry point from the casing to the reservoir and pulled out of the wellbore. Next, the pad volume is pumped with fracturing fluid that is pressurized on the surface and pumped downhole through the wellbore. The pad fluid is composed of water and chemical additives such as friction reducer. Once the fracture initiates, proppant is added to the fluid mixture to create a conductive fracture network, and the stage continues until the designed fluid mixture has been fully pumped in the stage to create a fracture network in the subsurface. This process is repeated along lateral portion of the well that lies in the targeted formation. The fracture network created during the hydraulic fracturing process phase can heavily impact the development of an unconventional reservoirs.

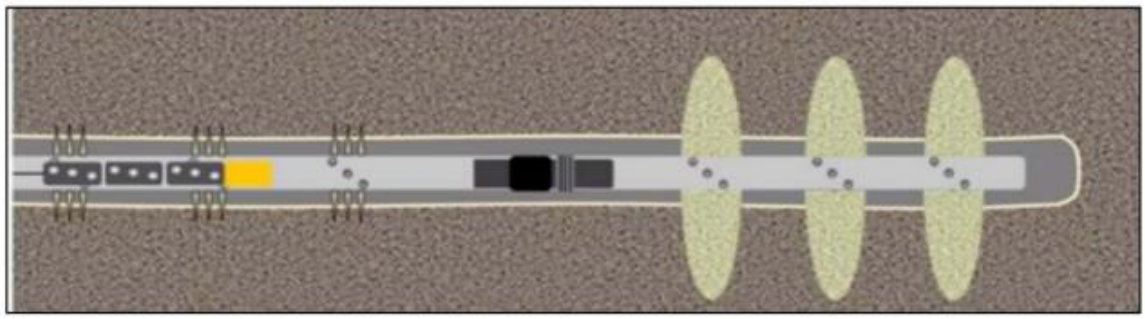

Figure 1.2 An illustration of the plug-and-perf completion technique (Salah et al., 2017).

1.1.2. Distributed Acoustic Sensing

Distributed acoustic sensing (DAS) can measure small acoustic changes over lengths of continuous fiber. The concept was first introduced in the 1980's driven by research on optical time-domain reflectometers (OTDR) that highlighted the ability of a single continuous fiber to capture measurements of tight spatial resolution, with sourced laser pulses replacing conventional single-point sensors (Krohn et al., 2015). Figure 1.3 is an optical interrogator unit that emits a tunable light pulse; and based on designed impurities along the fiber, varying quantities of light are backscattered and measured by an interrogator unit. The introduction of compression or extension along the fiber can affect the backscattered signal (Krohn et al., 2015). Distributed fibers can provide these measurements at tight spatial resolutions along full lengths of the fibers. This technique consists of a spectrum of scattered light resulting in different scattering techniques for various applications.

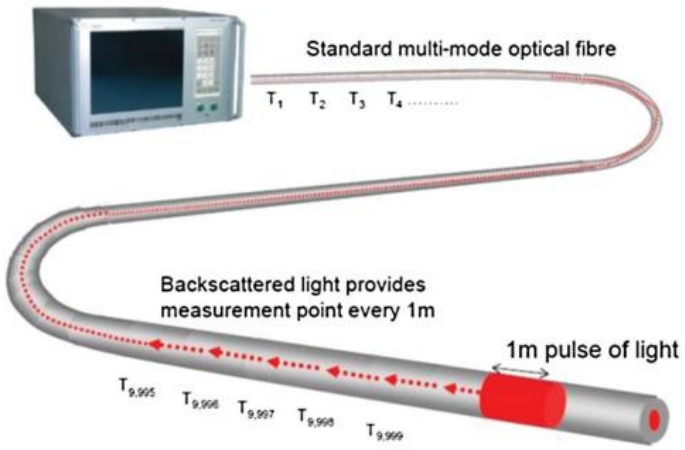

Figure 1.3 Schematic of the distributed acoustic sensing interrogation technology in practice (Krohn et al., 2015).

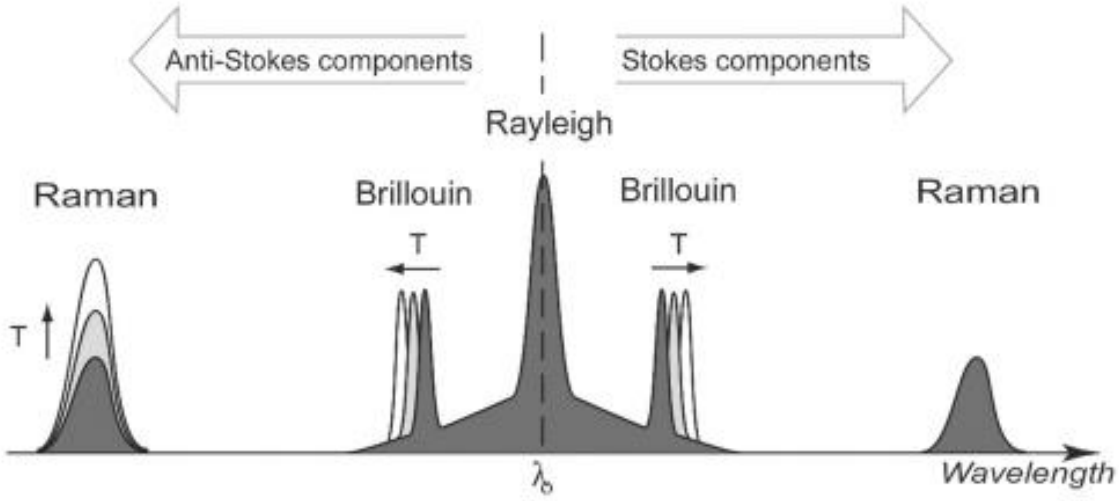

Figure 1.4 Full spectra of backscattered light for Rayleigh, Raman, and Brillouin scattering (Krohn et al., 2015).

1.1.3. DAS in Upstream Oil and Gas Applications

There are numerous fiber technologies capable of deployment to further understand during hydraulic fracturing, such as distributed temperature sensing (DTS), distributed

strain sensing (DSS), and distributed acoustic sensing (DAS). Fiber optic cables in these applications are deployed in treatment wells and/or offset monitoring wells. Treatment well applications utilize cables clamped on the production string and cemented in place of the hydraulic fracturing injection well, while in monitoring well applications the fiber optic sensor cable is clamped on the production string and cemented in place, or temporarily run inside the wellbore on a wireline at a well offset to the injection well. Recent comparisons of these two methods showed similar results, with more decoupling of the fiber from the wellbore casing occurring on the wireline inside the casing than cemented in place on outside of the casing (Richter et al., 2019). Figure 1.5 illustrates fiber applications for treatment and monitoring wells for fiber run on the outside of casing.

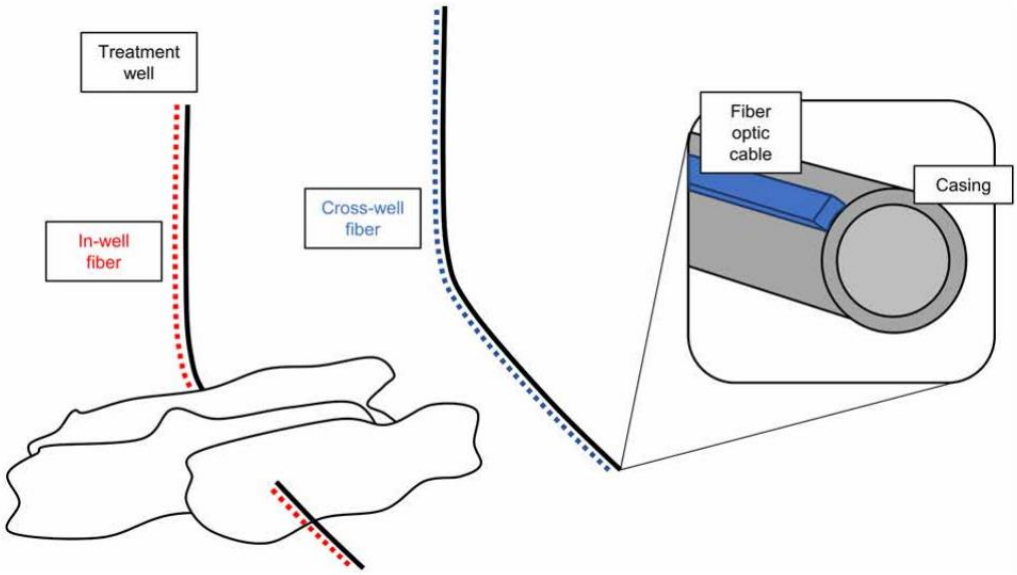

Figure 1.5 Schematic representation of fiber in treatment well (red) and monitoring well (blue) (Leggett et al., 2023).

DAS is studied in both the high and low frequency band. The high frequency band of DAS data reveals insights about fluid flow to individual clusters, shedding light on fluid distribution downhole (Molenaar & Cox, 2013), while the low-frequency band of DAS (<1 Hz) supports studies in the far field around the fracture geometry and growth over time (Jin & Roy, 2017). DAS can also be used to detect microseismic events. This type of diagnostic showed to be more effective than localized seismic arrays for completion diagnostics (Chavarria et al., 2022; Karrenbach et al., 2019).

1.1.4. LF-DAS Field Studies

LF-DAS technologies are most deployed as part of multi-diagnostic field studies. Some of the collaborative approaches involved joint projects between energy companies, academic institutions, fiber optic technology service providers, consulting firms, and government agencies represented by subject matter experts from all backgrounds to study unconventional reservoirs in the hydraulic fracturing space, capable of bringing to bear a formidable collection of diagnostic and monitoring techniques. Such a collaboration permits the collection of key information related to reservoir development that otherwise could not be obtained.

These projects typically include multiple diagnostic technologies such as fiber optics, down hole pressure arrays, seismic monitoring, sealed wellbore pressure monitoring, down hole video camera, caliper logging, and micro-seismic data. These methods reveal reservoir properties and shed light on hydraulic fracturing methods. The synchronized data sets provided from different sources help reduce uncertainty and create a more complete picture of the fractured reservoir. With the results of these experiments,

hydraulic fracture models can be calibrated for further sensitivity analysis of different hydraulic fracturing designs before field execution.

The study of LF-DAS in these field cases revealed characteristics of fractures and their geometry. Published work related LF-DAS signatures to fracture driven interactions at wellbores offset to the treatment well (Jin & Roy, 2017; Ugueto et al., 2019; Ichikawa et al., 2020; Raterman et al., 2020; Kerr et al., 2022). Offset well LF-DAS data with narrowing regions of extension surrounded by areas of compression indicates a fracture is approaching the offset well. During fracture opening there is a consistent area of extension and upon fracture closure, the polarity of the strain response at the fracture flips from extension (red) to compression (blue) as shown in Figure 1.6.

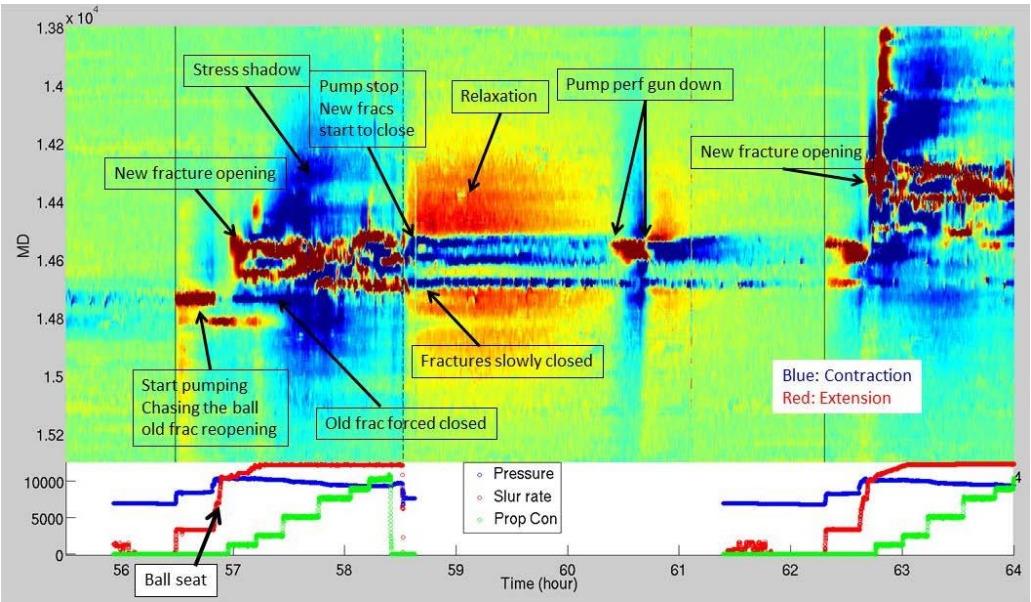

Figure 1.6 LF-DAS waterfall plot during hydraulic fracturing in offset well where the color represents strain (blue for compression and red for extension) (Raterman et al., 2020).

Such diagnostic methods are employed to seek out optimal reservoir development strategies in different unconventional resource plays. Published and studied field scale projects include the Hydraulic Fracturing Test Sites (HFTS) (Pudugramam et al., 2022), Shell's Montney Shale (Ugueto et al., 2019), Devon Energy's Anadarko Basin assets (Haustveit et al., 2020), Hess Corporation's Bakken assets (Cipolla et al., 2023), and SM Energy's Austin Chalk/Eagle Ford assets (Kerr et al., 2022). The HFTS projects in the Permian Basin revealed diagnostic methods including horizontal and vertical well fibers (DTS/DAS/DSS), downhole microseismic arrays, downhole pressure gauges, sealed wellbore pressure monitoring (SWPM), core-through data, image logs, diagnostics fracture injection test, proppant-in-cuttings analysis, interference tests, and production data can be studied and lead to successful calibration of reservoir models that can be used to simulate for optimal hydraulic fracturing designs (Pudugramam et al., 2022). Published work from Shell sheds light on the use of strain signatures in monitoring wells to reveal information about fracture geometries in the far field to optimize their stage offsetting and well azimuth strategies (Ugueto et al., 2019). Furthermore, Devon Energy's publicly available documents highlighted the use of Sealed Wellbore Pressure Monitoring (SWPM) (Haustveit et al., 2020). Recent work compared SWPM and LF-DAS verifying the fracture arrivals in the LF-DAS matched the arrivals from SWPM (Haustveit et al., 2022). Additionally, SM Energy deployed a multi-diagnostic test in one of their developing fields. Their results suggest calibrated models and diagnostic methods are driving efficiencies with their completions designs, well spacing configurations, and real-time and post-stimulation production analyses (Kerr et al.,

2022). These diagnostic case studies are revealing critical insights into the subsurface while also creating a deeper understanding of the diagnostic methods themselves to further the economic development of unconventional reservoirs.

1.1.5. LF-DAS Experimental Investigations

Laboratory-scale experiments performed by Texas A&M University validated the converging extension pattern surrounded by compression to indicate a fracture intersection. A method was developed to estimate fracture geometry from the location of zero-strain along a fiber optic sensor (Leggett et al., 2022).

The experiments consisted of injecting dyed water into an unconfined 8-inch cube of epoxy with a 1-inch radial initial flaw in the middle of sample to initiate a fracture. During injection, the fracture geometry, pressure, and strains were measured. The experiments used an array of fiber Bragg grating (FBG) to measure the strain around the fracture plane, creating quasi-distributed sensors in the sample acting as a distributed sensor for the purposes of the experiment. This laboratory-scale experiment proved successfully LF-DAS responses to a propagating fracture in a laboratory-scale environment.

The experiments led to the development of the zero-strain location method which can dynamically estimate fracture propagation. The experiments determined that the location of zero-strain has a one-to-one correspondence with fracture radius (Leggett et al., 2022). The work was validated with experimental data and field cases. These experiments laid the groundwork for how LF-DAS can be studied in the laboratory and

scaled to field applications. A comprehensive review of the zero-strain location method and its development can be found in Section 2.1.

1.1.6. Shear-Slip Movements During Hydraulic Fracturing

Due to the complexity of the subsurface, hydraulic fracturing can induce shear-slip movements. Literature showed that hydraulically fractures in areas with pre-existing faults or natural fracture are not always created as designed.

For example, a case study in China's Sichuan shale gas basin showed 32 out of 101 wells experience casing deformation. The case study concluded that the cause of casing deformation was hydraulic fracturing induced fault through the use of microseismic monitoring data and caliper logs (Chen et al., 2018). Casing deformation can negatively impact the deliverability of a well. In severe cases, the well can completely close. With an increasing number of diagnostic methods for hydraulic fracture monitoring, LF-DAS being deployed to further to study casing deformation.

1.2. Motivation

Major oil companies, government agencies, and consulting firms published energy outlooks through 2050. While these projections vary slightly, they all align with the premise that oil and natural gas possesses a significant role to play in the energy mix for at least the next three decades. Energy demand is expected to follow the projected increase in population. The projections vary in the relative amounts of oil and gas in the total energy mix; however, none project the total amount oil and gas to significantly change by 2050. Figure 1.7 depicts ExxonMobil's 2022 Outlook for Energy depicting an increased overall energy demand by 2050, with a 15% increase in overall energy

demand based on a population growth of ~2 billon, of which 55% of the global energy mix will be supplied by oil and natural gas.

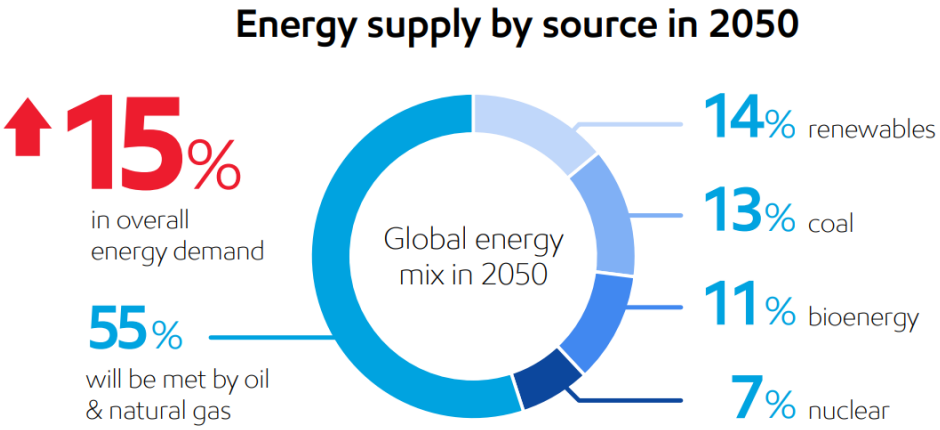

Figure 1.7 Energy Supply by Source in 2050 (ExxonMobil, 2022).

In the Energy Information Agency (EIA)'s Annual Energy Outlook for 2022 in Figure 1.8, the agency depicts the historical and projected energy consumption by fuel source, while highlighting that oil and gas remain the most consumed source of energy in the United States through 2050. The EIA historical and projected energy consumption cases indicate a significant increase in oil and natural gas consumption relative to the few years prior to 2010 when hydraulic fracturing was in its initial stages of development.

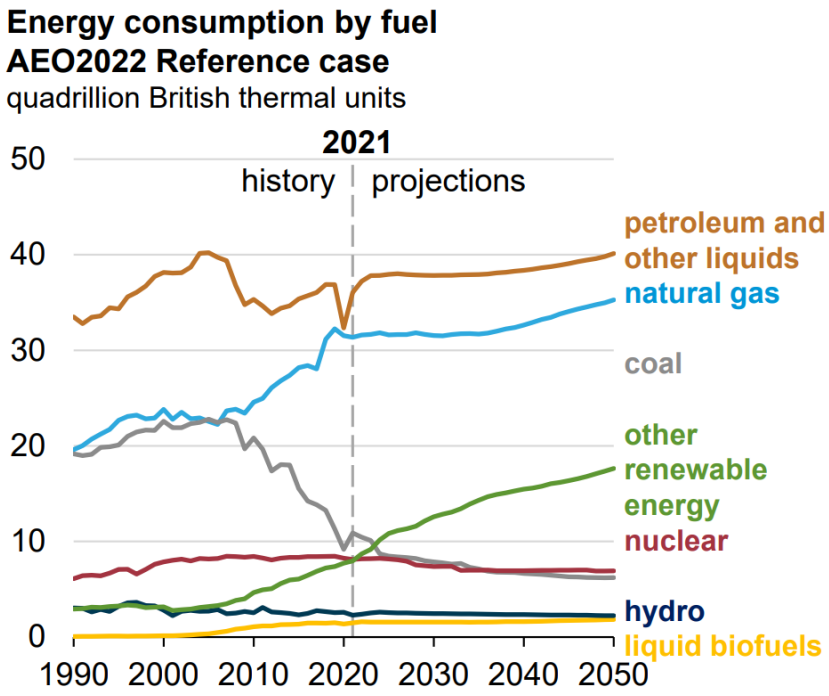

Figure 1.8 Historical and projected energy consumption by fuel source (EIA, 2022).

McKinsey and Company's Energy Insights Global Energy Perspective 2022 projects an increase in energy consumption with a strong emphasis on electric and hydrogen growth, however, fossil fuels remain an integral part of the global mix of energy consumption (Figure 1.9). From these energy outlooks, there is a continuing need for low-cost, reliable, and clean energy. Unconventional reservoirs are playing a tremendous role in providing energy for the world that is steadily meeting this trifecta. With improvements to decarbonizing oil and gas operations, operators are making considerable progress in reducing costs for oil and gas exploration and projection.

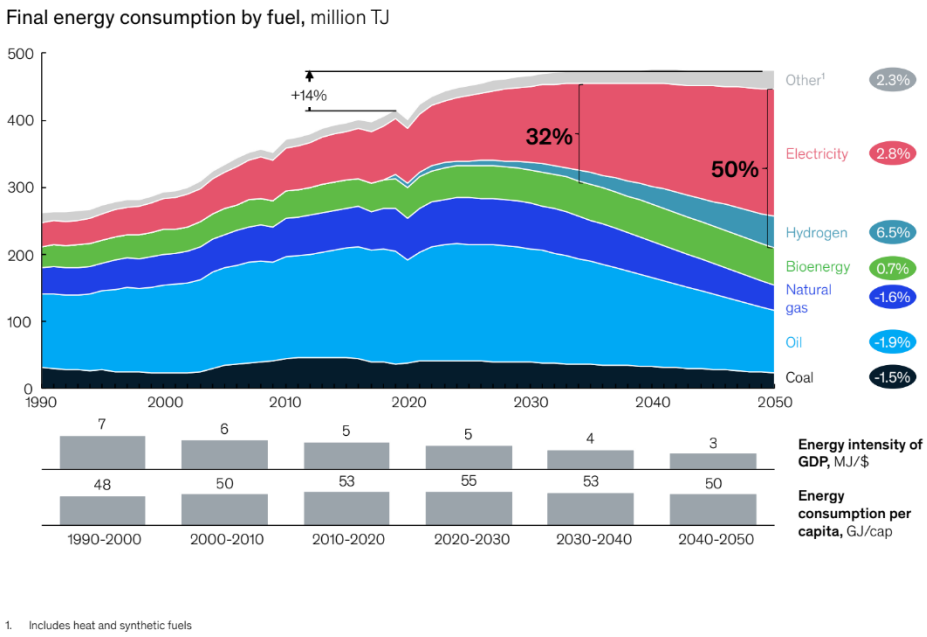

Figure 1.9 Final energy consumption for the global energy mix (McKinsey & Company 2022).

Hydraulic fracturing unlocked the development of unconventional reservoirs. As the production from unconventional reservoirs continues to rise, petroleum engineers constantly seek opportunities to further optimize capital expenditure. The most impacted areas are in hydraulic fracturing optimization for full-scale reservoir development from well spacing, fracture half length, and perforation design. Fiber optics are playing a vital role in such optimization. LF-DAS is being deployed in wellbore offsets in hydraulic fracturing operations to diagnose the fracture treatments.

With advances in technology, the opportunities to deploy fiber optic sensing in oil and gas became increasingly more economic. Oil and gas companies, service providers, and

government agencies are collaborating to invest in these technologies to further develop their resource plays.

The ability of petroleum engineers and geoscientists to understand diagnostic data sets can enable lower-cost, more reliable, and cleaner energy. However, fundamental questions on the subsurface remain, such as what is the geometry of hydraulic fractures? How do fractures evolve under shear and normal stresses? Can LF-DAS be utilized to predict when a shear slippage will occur? LF-DAS data started shedding light on some of these questions to help generate answers and enhance completion design and reservoir development.

1.3. Problem Statement

The ability to unpack LF-DAS data can be very impactful to completions optimization and reservoir development. Numerous field cases and experimental investigations were conducted; however, the introduction of a shear stress to a propagating fracture has not yet been investigated. What we can observe about fracture geometry when there is a shear and normal stresses on the fracture plane is still a question.

In extreme cases, shear stresses in the subsurface during hydraulic fracturing can result in deformed casings of wellbores offset to active hydraulic fracturing well. Therefore, by studying the cross-well strain responses of shear and normal stresses during hydraulic fracturing in the lab, the goal is to determine a pattern in the strain data that acts as a precursor to casing deformation. This could be used as a real-time fracturing diagnostic to halt the hydraulic fracturing job and eliminate any further shear deformation. The following are the primary research objectives:

a. Observe the LF-DAS response normal to a propagating fracture with shear and normal stresses on plane that passes the fiber.

b. Compare these results to previous LF-DAS experimental work where purely normal stresses existed on a plane that passed through the fiber.

c. Understand how the zero-strain method (Leggett et al., 2022) applies to the studied case and what the strain data reveals about fracture geometry under more complex conditions.

2. EXPERIMENTAL METHODS

2.1. Zero-Strain Location Method Development

Laboratory-scale experiments performed by Texas A&M University validated the converging extension pattern surrounded by compression to indicate a fracture intersection. A method was developed to estimate fracture geometry from the location of zero-strain along a fiber optic sensor (Leggett et al., 2022).

Figure 2.1 depicts the experimental set up. The experiment consisted of injecting dyed water into an unconfined 8-inch cube of epoxy with a 1-inch radial initial flaw in the middle of sample to initiate a fracture. During injection, the fracture geometry, pressure, and strains were measured. The experiments used an array of fiber Bragg grating (FBG) to measure the strain around the fracture plane, creating quasi-distributed sensors in the sample acting as a distributed sensor for the purposes of the experiment.

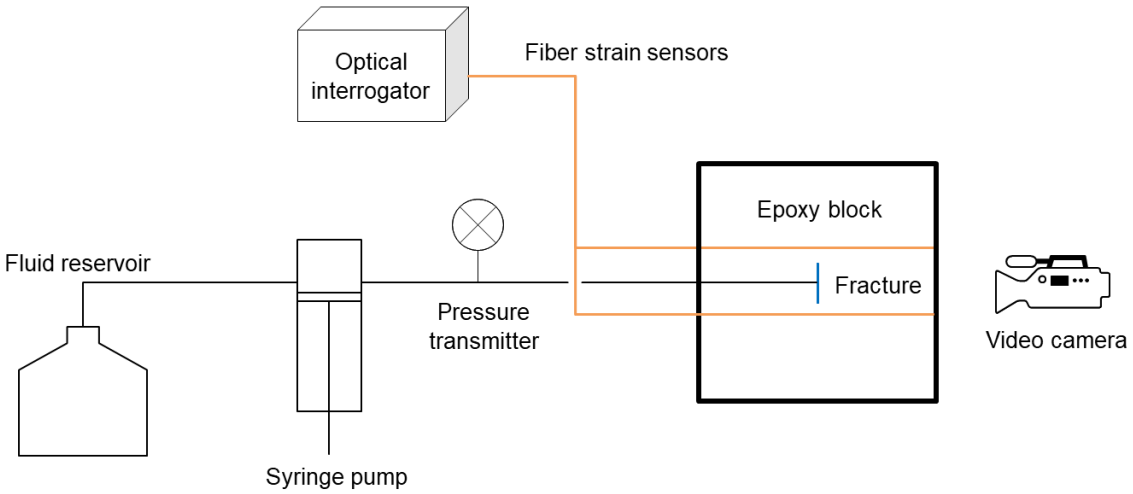

(Leggett et al., 2022)

Figure 2.1 Schematic of the experimental set up for the fracture injection test (Leggett et al, 2022).

The evolution of the fracture radius observed is shown in Figure 2.2. The white cross hairs represent the location of the embedded fiber optic cables. Using the measured radii with the strain data, the zero-strain location method was developed to dynamically estimate fracture propagation. The experiments determined that the location of zero-strain has a one-to-one correspondence with fracture radius (Leggett et al., 2022).

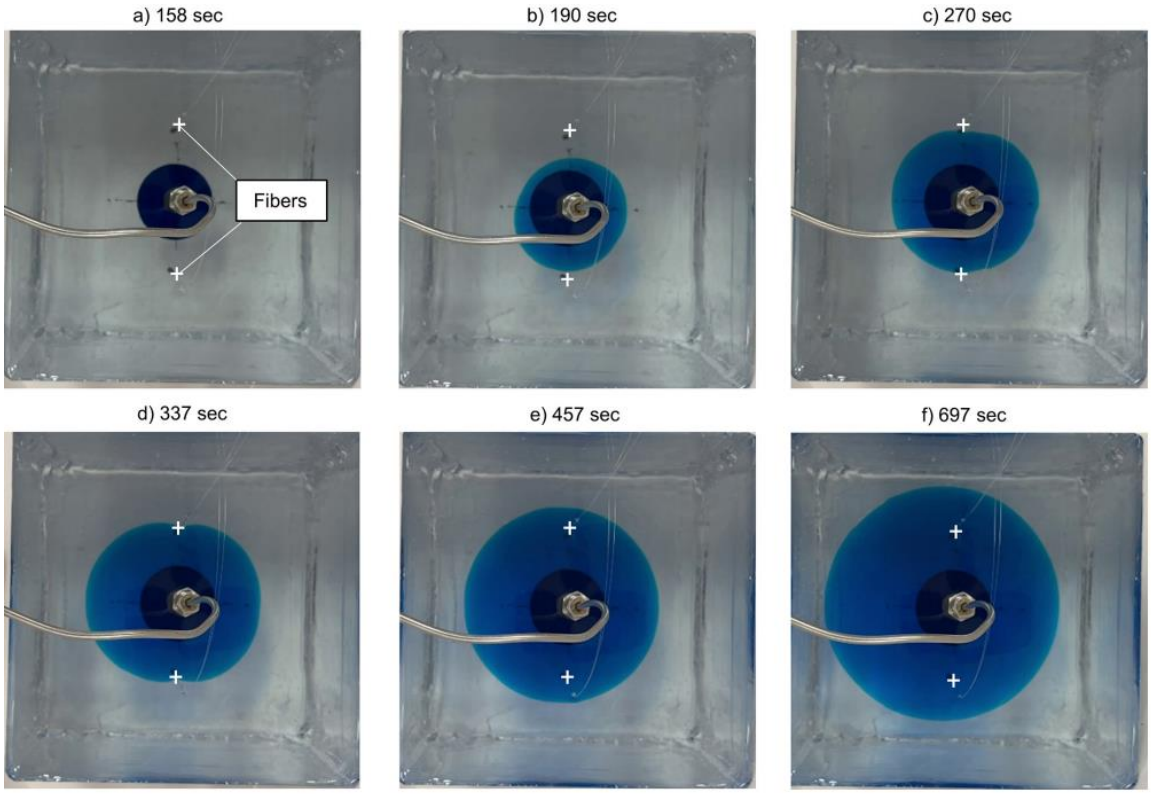

Figure 2.2 Fracture evolution during the experiment with purely normal stresses on the fracture plane (Leggett et al., 2022).

The zero-strain locations can be determined from strain waterfall plots (shown in Figure 2.3) as the locations along the length of the fiber that experience a flip in polarity of the strain response as a fracture is propagating. By defining the zero-strain locations, offset

horizontal and vertical distances of the monitor well from the treatment well, and Poison's ratio, the location of the nearest fracture to the monitor well can be estimated. The zero-strain location method was validated experimentally in the laboratory and with a field case (Leggett et al., 2022). Figure 2.3 shows a converging strain (top) and strain-rate (bottom) pattern of extension surrounded by compression prior to the fracture intersection near 150 seconds.

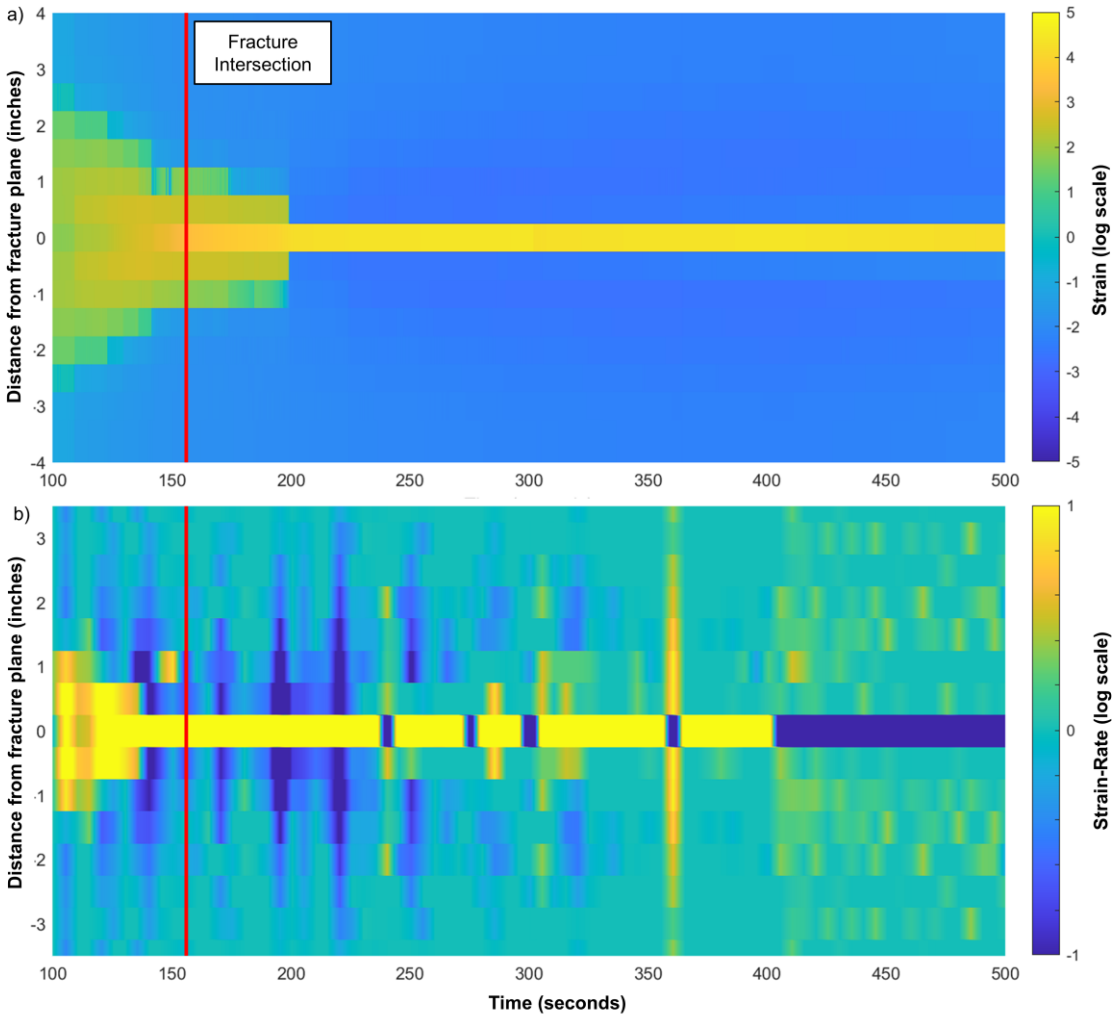

Figure 2.3 Strain and strain-rate waterfall plots from a fracture experiment. The vertical line near 150 seconds denoted the time the fracture intersected an embedded fiber (Leggett et al., 2022).

Interestingly, the experimental results aligned with Sneddon's solution for the strains in an infinite elastic medium to a penny-shaped crack (Sneddon, 1946) when accounting for boundary effects. Figure 2.4 illustrates the comparison of strains versus location on the fracture plane for the measured data (crosses with error bars) matched the modeled results for an 8-inch cube using a finite element model simulator. The measured data

matches the shape of Sneddon's solution, however overestimates Sneddon's strain prediction for strains in an infinite linear elastic medium in response to a propagating penny-shaped crack. However, when a larger cube simulation was run, it aligned perfectly with Sneddon's solution.

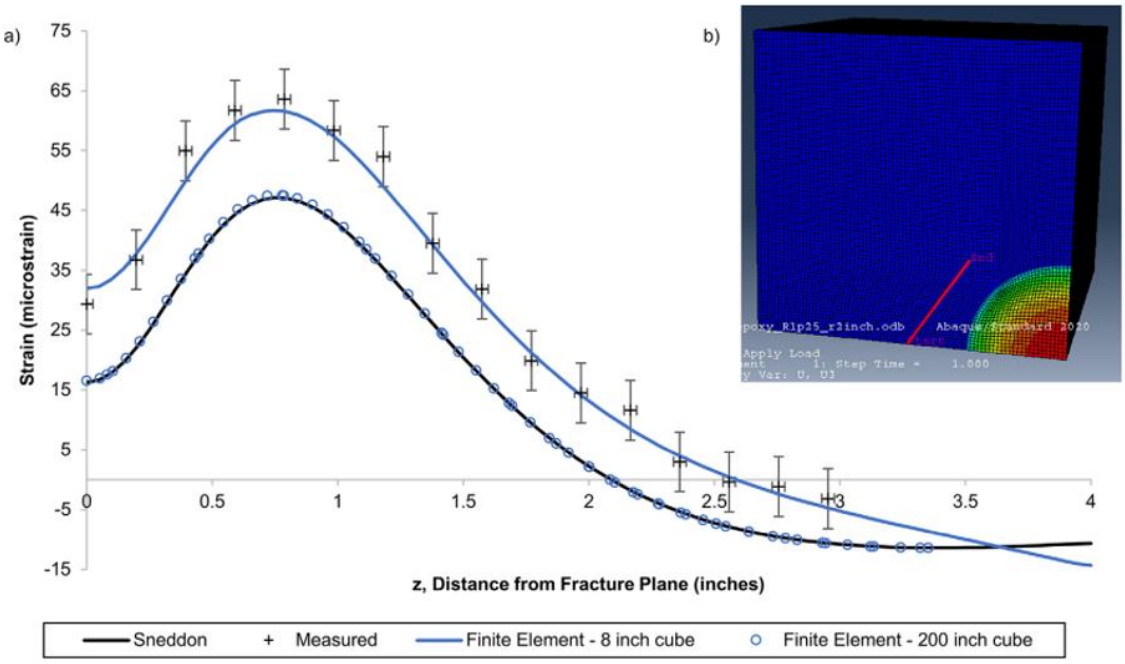

Figure 2.4 (a) Experimentally measured strains and modeled strains along the distance of the fiber from fracture plane. (b) Snapshot of the displacement in the z-plane from the finite element model simulator (Leggett et al, 2022).

The experimental design successfully simulated the LF-DAS response to a propagating fracture with a normal stress on the fracture plane. The model was verified through both the experimental work and a field case. The results for the experimental case are shown in Figure 2.5. The strain-rate (top) and strain (bottom) waterfall plots of the field case are shown in Figure 2.6. The cone-shape feature of the strain and strain rate pattern can be

observed in both plots. The location of the fiber where the fracture was intersected is labeled as D_{hit} based on the strain convergence on the waterfall plot. The extracted zero strain locations are presented in Figure 2.7a, and the modeled distance to the fracture front is presented in Figure 2.7b.

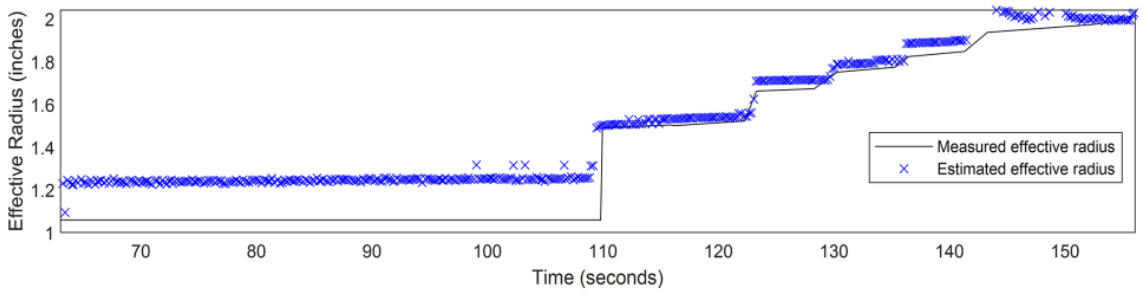

Figure 2.5 Experimentally measured and estimated fracture radius using the zero-strain location method (Leggett et al., 2022).

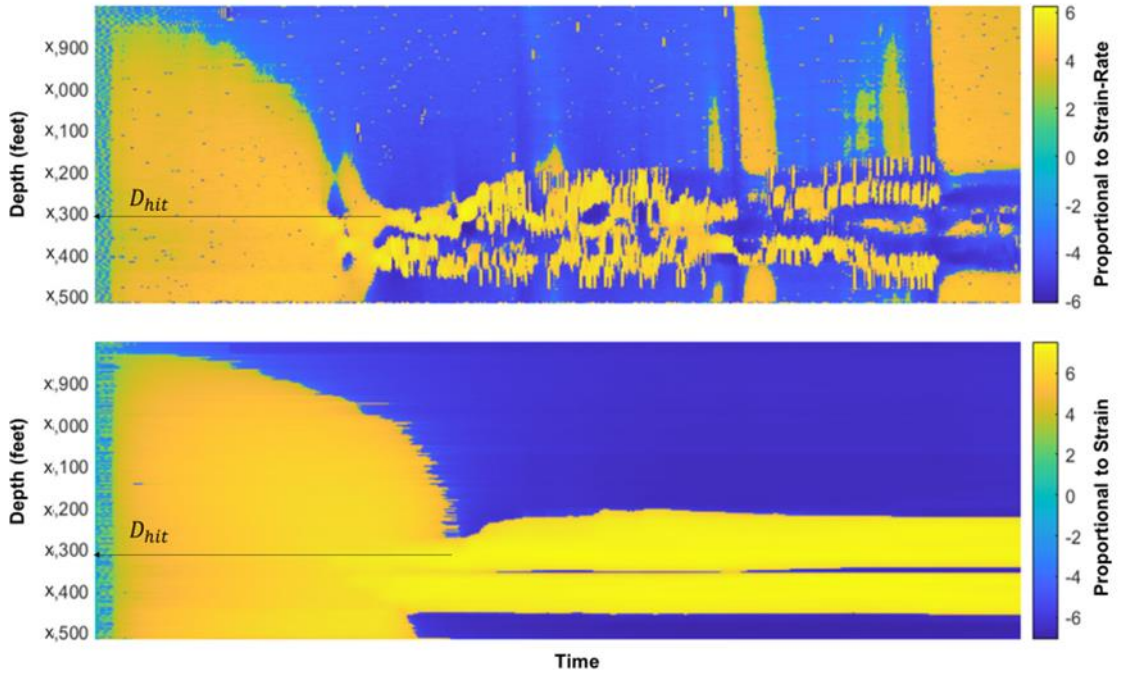

Figure 2.6 LF-DAS strain-rate (top) and strain (bottom) waterfall plots, with the fracture hit location D_{hit} marked (Leggett et al., 2022).

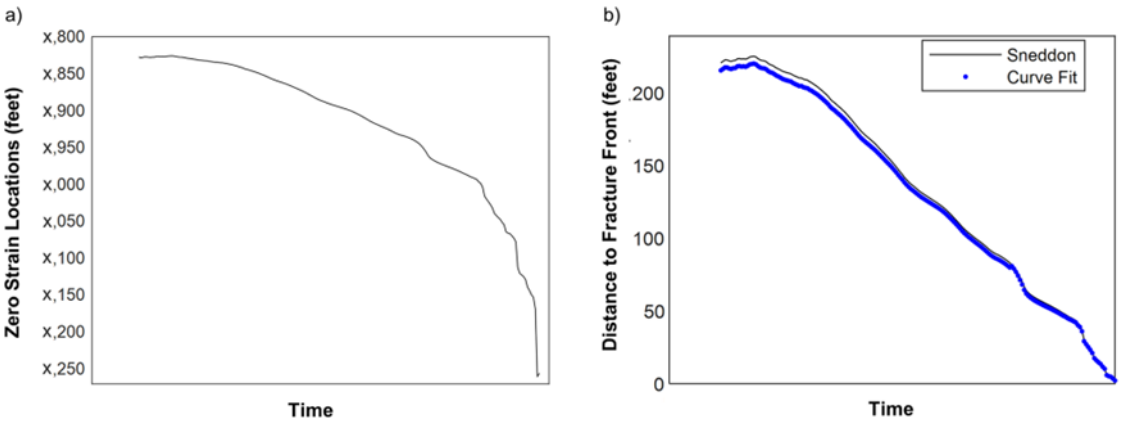

Figure 2.7 (a) Zero-strain locations D_0 extracted from the strain waterfall plot and (b) estimated distance to the fracture front (Leggett et al, 2022).

Multiple experiments of different spatial resolution revealed that higher resolution strain and strain-rate data converged closer to the actual time of fracture intersection depicted in Figure 2.8. The experiments were performed with 1, 2, and 5 FBG per inch.

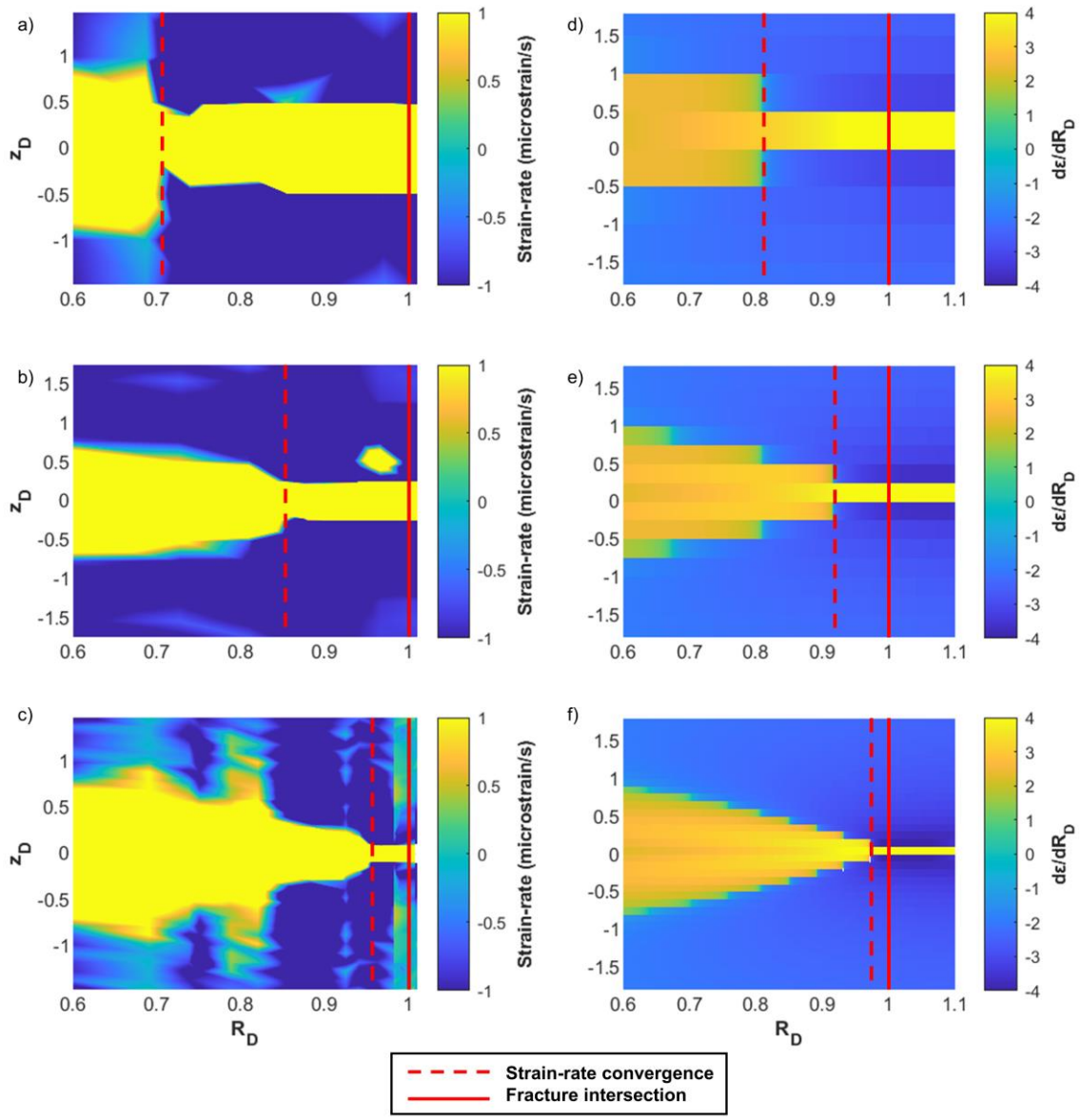

Figure 2.8 Strain-rate waterfall plots from experiments (left column) and model predictions (right column) with dimensionless spatial resolutions of 0.5 (a and d), 0.25 (b and e), and 0.1 (c and f) (Leggett et al., 2022).

By identifying a cone-shaped signature of the strain pattern of extension to compression, the distance from the fiber to the fracture tip can be computed. Since the laboratory investigation produced results that aligned with Sneddon's solution linear elastic solution for a penny-shaped crack, a model was developed to estimate the distance of the nearest fracture front from the monitoring well. Sneddon's model can be simplified as Equation 2.1 for a displacement, u_z, and Equation 2.2 for a strain, ε_z, at any location in an infinite medium for a radial crack in the direction normal to the plane of crack, z, as a function of fracture net pressure, P_{net}, fracture radius, R, Poisson's ratio, v, Young's Modulus, E, a Bessel function, J_0, a parameter from Henkel transform, η, dimensionless depth, ζ, and dimensionless radial coordinate, ρ.

$$u_z = \frac{-4P_{net}R(1-\nu^2)}{\pi E}\int_0^\infty \left(1+\frac{\zeta\eta}{2(1-\nu)}\right)\left(\frac{cos\eta}{\eta}-\frac{sin\eta}{\eta^2}\right)e^{-\zeta\eta}J_0(\rho\eta)d\eta \qquad 2.1$$

$$\varepsilon_z = \frac{d}{dz}\frac{-4P_{net}R(1-\nu^2)}{\pi E}\int_0^\infty \left(1+\frac{\zeta\eta}{2(1-\nu)}\right)\left(\frac{cos\eta}{\eta}-\frac{sin\eta}{\eta^2}\right)e^{-\zeta\eta}J_0(\rho\eta)d\eta \qquad 2.2$$

The detailed steps below outline how to perform the zero-strain location method to estimate the distance to the fracture front of the nearest fracture to the monitoring well. (Leggett, 2022).

1. Determine a series of zero-strain locations as a function of time based on the converging pattern of the strain waterfall plot.
2. Calculate the dimensionless zero-strain location, z_{0D} with Equation 2.3.

$$z_{0D} = \frac{|D_0(t) - D_{hit}|}{\sqrt{\Delta l^2 + \Delta h^2}} \qquad 2.3$$

Where $D_0\ (t)$ is the measured depth along the fiber where the integrated LF-DAS phase shift is zero (from step 1), D_{hit} is the measure depth where the fracture intersects the fiber (center of cone-shaped region), and Δl and Δh are horizontal and true vertical depth offsets between the treatment well and monitor well.

3. Calculate the dimensionless crack radius, R_D, at every dimensionless zero-strain location using Equation 2.4 using correlation coefficients from Table 2.1.

$$R_D = \frac{-b - \sqrt{b^2 - 4a(c - z_{0D})}}{2a} \qquad 2.4$$

Table 2.1. Zero-strain location method curve fit coefficients (Leggett et al. 2022).

	$Z_{0D} > 1$	$0.75 \leq Z_{0D} \leq 1$	$Z_{0D} < 0.75$
a	-0.141ν - 0.473	-1.24ν - 0.702	-4.06ν - 3.01
b	0.0707ν + 0.00106	1.72ν + 0.142	7.82ν + 3.73
c	0.331ν + 1.05	-0.246ν + 1.04	-3.39ν - 0.348

4. Calculate the distance to the nearest fracture front from the monitoring well, d_f, using Equation 2.5.

$$d_f = \sqrt{\Delta l^2 + \Delta h^2}(1 - R_D) \qquad 2.5$$

The model proposed by Leggett et al. (2022) was verified with a field case study to dynamically estimate the distance to the fracture front from LF-DAS data. In the developed model, the strain is only dependent on fracture radius, net pressure, Young's

Modulus and Poisson's ratio. The previous experimental work also concluded that for a radial fracture there is a one-to-one correspondence between the location of zero-strain and the fracture radius leading to the development of the zero-strain and zero-strain rate method. These experiments laid the groundwork for exemplifying how LF-DAS can be studied in the laboratory and scaled to field applications.

2.2. Overview of Experiments

This chapter details the experimental apparatus designs and procedures for the laboratory-scale hydraulic fracture experiment. The experiment conducted consists of injecting dyed water into 8-inch transparent epoxy cubes with an angled fracture under a uniaxial compressive load while measuring the strain, pressure, and fracture geometry. This simulated a LF-DAS response in the subsurface with shear and normal stresses on the rock to be fractured.

A schematic representation of the lab-scale hydraulic fracture experiment is provided in Figure 2.9. An 8-inch cube of epoxy is used in the experiment to represent formation rock. A flaw is embedded at the center of the block which has a 5.12-degree angle to the vertical in the center of the block. The flaw assisted the initiation of the angled fracture. A syringe pump injected dyed water into the center of the epoxy fracture specimen to propagate the fracture. The flow rate was controlled through the pump controller on the syringe pump. A confining load of 72kN (equivalent 250 psi) was applied in the vertical direction. The pressure during injection was recorded from a pressure transmitter and the fracture geometry was recorded with a video camera at 30 frames per second. Four high-definition strain sensors were used to measure the strain along offset locations, 2-inches

from the center of the 1-inch radial fracture, (as in a monitoring well) to the injection tubing (as in a treatment well).

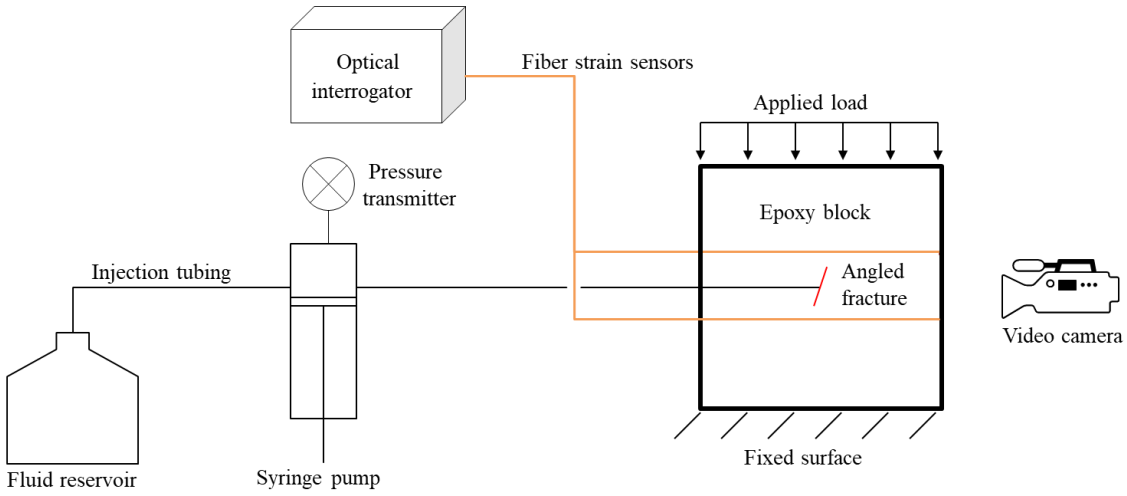

Figure 2.9 Schematic representation of the lab-scale hydraulic fracture experiment with load (modified from Leggett et al., 2022).

The fracture specimen was created within a plywood mold lined with polypropylene sheathing tape. The EcoPoxy Flowcast resin and hardener system was used to create the epoxy cubes representing the reservoir in a LF-DAS application. The mechanical properties of the epoxy at the time of the test are dependent on the curing time and temperature. The temperature of the laboratory during curing and experiment was maintained at 72ºF. The curing process of epoxy is an exothermic process, so it is recommended by the manufacturer that the epoxy is poured in 1-1.5 inch thick layers. The constructed sample consisted of a 6-layer epoxy cube where each layer was designed for a cured thickness of 1.333 inches. Each layer cured for 72 hours before

another layer was poured. The injection test was performed 7 days after the final layer was poured.

The third layer of the epoxy was cured at a 5.12º angle to create an angled flaw during the fracture injection test. The initial flaw consisted of a 1-inch circular piece of polypropylene sheathing tape and was centered in the middle of cube around the fibers. A ½-inch diameter hole was drilled 1.5-inches into the epoxy through the middle of the fracture after pouring layer four. A ¼- inch stainless steel was set in the hole with quick epoxy. An O-ring was set on the injection tubing 1 inch above the end of the injection tubing to preserve connectivity between the end of tubing and the initial flaw. Figure 2.10 is a schematic representation of the epoxy specimens illustrating the fiber optic sensor locations (blue and green lines) with rest of the sample.

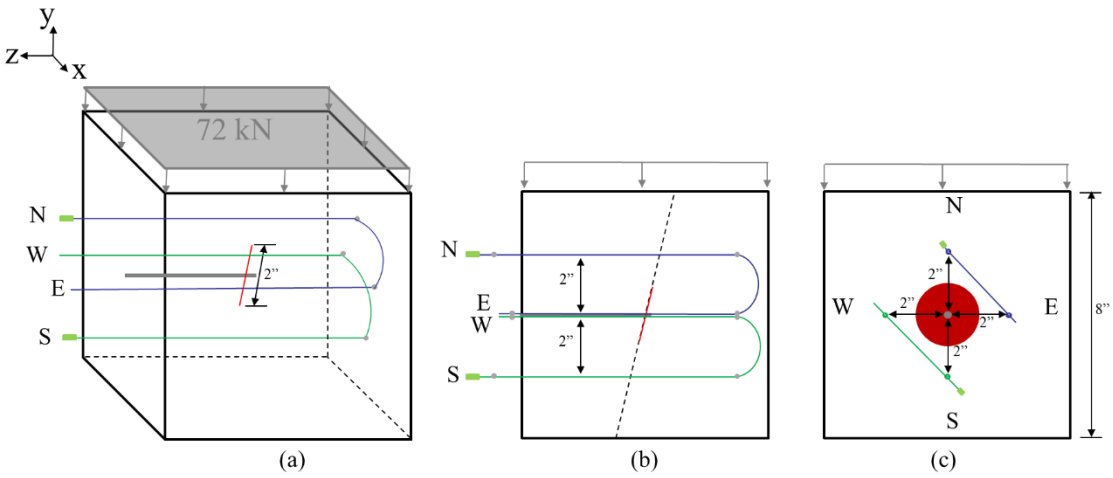

Figure 2.10 Schematic representation of the epoxy specimens: (a) isometric view, (b) a view normal to the fracture plane, (c) a view normal to the injection tubing and fiber optic cables (modified from Leggett et al. 2022).

2.3. Pressure Measurements

Pressure measurements were obtained from the pressure transducer within the Teledyne Isco D-Series syringe pump. The calibration of the transducer was validated against separate pressure transducers with known calibrations. The experiment was conducted at an injection rate of 0.25 mL/min. Assuming no barriers to flow exist between the open end of the injection tubing and the initial flaw, the pressure measurements represent the pressure in the fracture.

2.4. Fracture Geometry Measurements

A digital camera was utilized to record fracture propagation at a frame rate of 30 frame per second with a spatial resolution of approximately one hundred pixels/inch on the fracture plane. The digital camera and the face of the epoxy block were carefully aligned with each other to avoid angular distortions of the geometry measurements beyond the designed angle. The ratio of pixels to inches was calibrated for each experiment against the known dimensions of the initial flaw and the calibration markings applied on the surface of the fracture plane. The calibration markings serve as a reference point of known dimension for direct correlation to the geometry of the fracture recorded by the camera. The fracture radius and center were computed based on an equivalent area from photogrammetry measurements. The measurements are reliable at approximately the resolution of one pixel, or 1/100”. Since the geometry of the 5.12-degree angled fracture lies within the uncertainty of the pixel analysis, no further processing is required to capture the fracture geometry of the angled fracture. Figure 2.11 defines the measurement of the distance from the fiber to the fracture tip. The distance was

computed along a line from the fiber location point to the edge of the fracture nearest to the fiber.

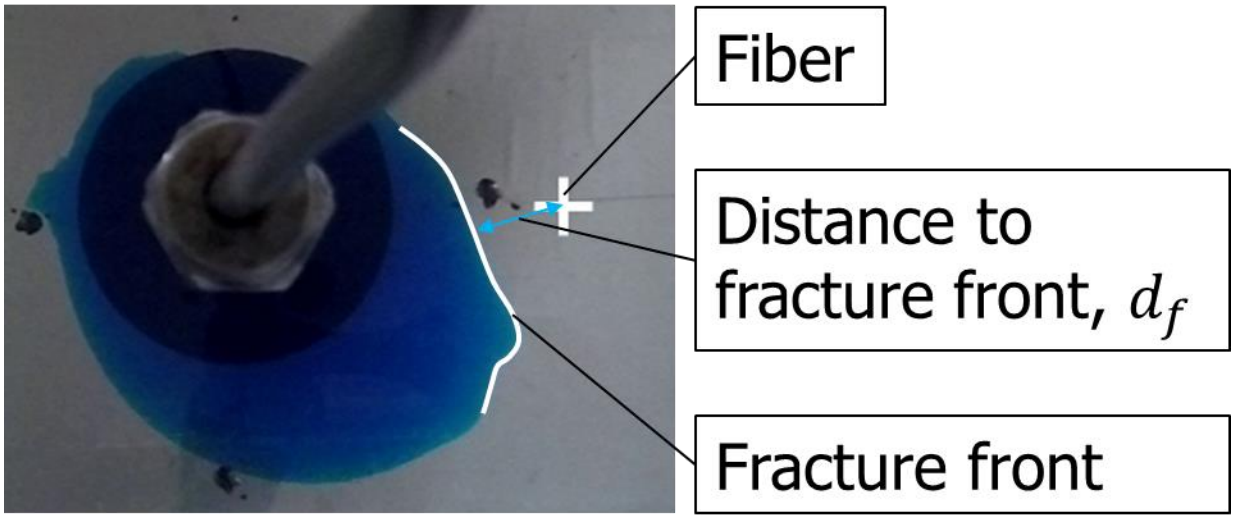

Figure 2.11 Example of an eccentric non-radial fracture observed in the experiment (modified from Leggett et al. 2022).

2.5. Specimen Preparation Procedure

The following list contains a detailed procedure for creating an epoxy fracture specimen with distributed strain sensors. The procedure follows what is documented in Smith Leggett's Dissertation (Leggett, 2022) with variation involved in pouring of the angled layer 3. Steps 1 through 9 addresses creating the mold and the fiber positioner. These steps are not necessary if an existing mold and fiber positioner are already available.

1. Prepare the wooden mold for the epoxy block. Use a table saw to cut pieces with the following dimensions from three-fourths-inch plywood. To attain uniform heights for the mold sides, it is recommended to make all the eight ½-inch cuts at

one time (do not adjust the table saw rip fence between cuts). The same reasoning applies for the nine ½-inch and 8-inch cuts.

   a. (2) - 9 ½-inch x 9 ½-inch pieces (for the base and fiber positioner)
   b. (2) - 8-inch x 8 ½-inch pieces (sides)
   c. (2) - 9 ½-inch x 8 ½-inch pieces (sides)

2. Measure and record the actual dimensions of the cut pieces accurately to within $1/100^{th}$ of an inch.
3. Select the smoothest surfaces of the plywood pieces to be used for the inside of the mold and cover with two layers of Tuck Tape Construction Sheathing Tape. Sand the surfaces if necessary. Ensure that the second layer of tape covers the seams of the first layer to prevent any seepage of epoxy between the tape edges into the plywood. Using only one layer of tape or not overlapping the seams resulted in epoxy seepage into the plywood mold in the past. Eliminate having the printing on tape overlap where markings are required in Step 4.
4. Using calipers, dimension and mark the center of the base with a fine-tipped pen. Also place cross-shaped marks two inches offset from the center towards each edge. These are used as location markers to verify that the fiber optic cables are in the correct position.
5. Using square clamps, carpenter squares, an electric drill, and #6 x 1 ½-inch screws, construct a rectangular box with 8-inch x 8-inch x 8 ½-inch inner dimensions as shown in Figure 2.12. The mold height is designed at 8 ½ inches, so the epoxy does not need to be poured to the very brim for an 8-inch block.

Pre-drill the screw holes with a countersink drill bit to prevent the plywood from cracking. Mark the top and bottom of each side, and label the sides as North, South, East, and West, to make it easier to reassemble the box. The labels also serve as a reference for placing the mold in the exact same position on the table to achieve level surfaces.

Figure 2.12 Epoxy block mold.

6. Caulk the inner seams of the box using silicone caulk to prevent epoxy from leaking out of the mold. Smooth the seams with a caulk finishing tool. After the caulk dries, fill the mold completely with water and check for leaks. Images of the necessary tools and caulked seams are shown in Figure 2.13.

Figure 2.13 Tools (left) used to caulk epoxy mold (right).

7. Using a table saw and electric drill, construct the fiber positioner out of the remaining 9 - ½-inch x 9 ½-inch plywood pieces as exhibited in Figure 2.14. The one-eighth-inch slots are used to guide the fibers to rest at exactly two inches away from the center of the block. Sand the edges of the one-eighth-inch slots to avoid any sharp edges that might cut, snag, or damage the fibers.

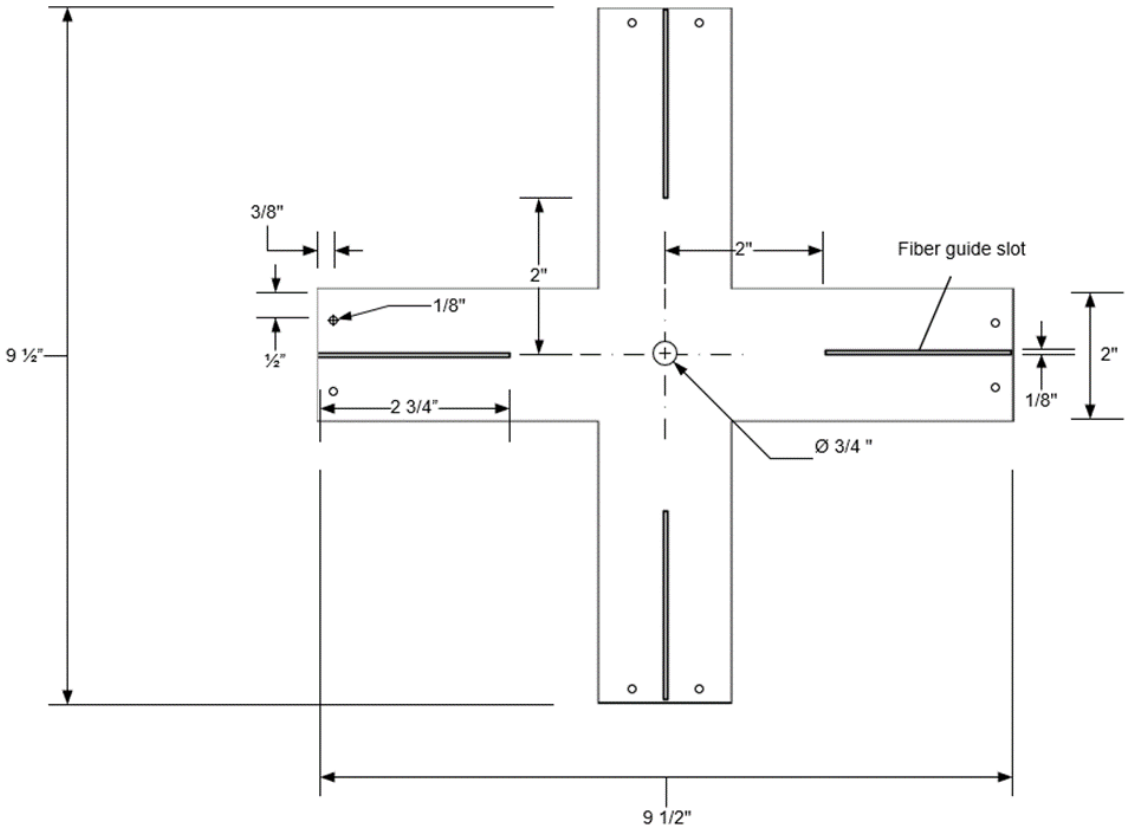

Figure 2.14. Dimensioned schematic of the fiber positioner (Leggett et al. 2022).

Figure 2.15 Fiber positioner used in experiments.

8. Measure the thickness of the fiber positioner. Nominally 3/4-inch plywood is measured to be closer to 0.73-inches thick.
9. Place the fiber positioner on top of the mold. Ensure it is centered by aligning its ends with the edges of the mold and screw the fiber positioner in place. Be sure to mark which side is facing up and which sides are North, South, East, and West so that it can be put back into the exact same position when removed.

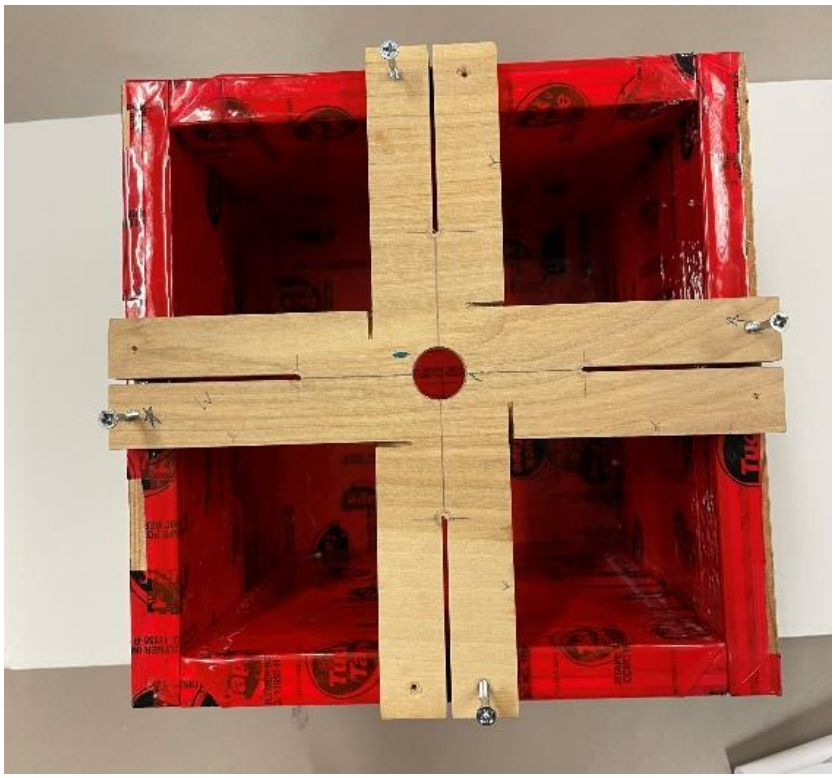

Figure 2.16 Fiber positioner centered and anchored to top of epoxy mold.

10. Obtain, measure, and record the dimensions of a piece of plywood large enough to support the epoxy mold and ring stand holding the fibers.
11. Obtain, measure, and record the thickness of propping materials (the wood shim) to create an angled surface.
12. Place the epoxy mold on the plywood and mark the location of the mold on the plywood.
13. Prepare to pour the epoxy in the mold. Ensure the box is in a well-ventilated, temperature-controlled environment. Maintain the room temperature at a constant 72 ºF +/- 1 ºF on days, nights, weekends, and holidays. The location should be

away from windows and not directly under an air vent. Major walkways in the room should be avoided so the box is not accidently bumped or jostled.

14. Use a bubble surface level to ensure that the table the mold is resting on is level. Place scrap wood, coins, or washers under the legs of the table to adjust the level as needed. Verify that the bottom of the mold and the top of the fiber positioner are level.
15. Design the placement of the distributed strain sensors. Figure 2.17 includes an example design for a distributed strain sensor. Key design considerations include:
    a. One inch bend radius should be always considered.
    b. Ensure at least three feet of fiber exists on each fiber beyond the sample. This is needed to reach the ODiSI unit during the testing procedure.
    c. Place a mark on the fiber that aligns with the top of the fiber positioner. This fiber depth marker, displayed as a red dot on the following figure, is used when hanging the fiber in place to ensure the fiber is in position.

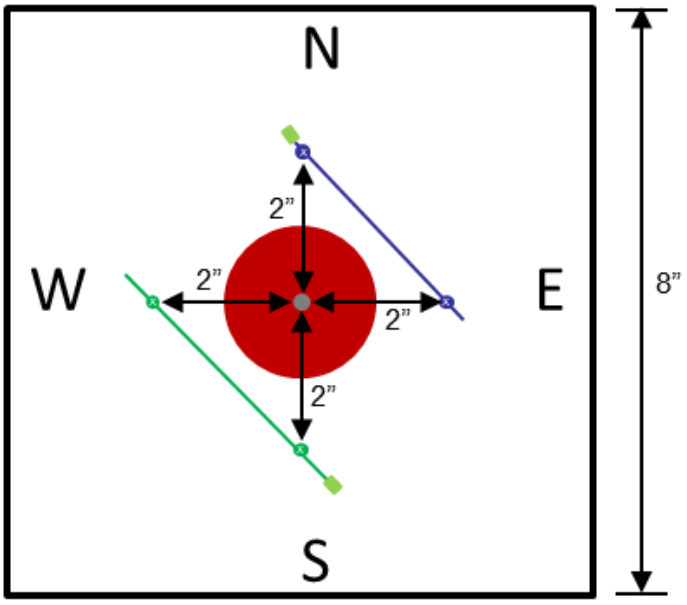

Figure 2.17 Example design of the distributed strain sensors. Each fiber is located two inches offset from the center of the initial flaw.

16. Trim excess fiber on the bare, non-connectorized end so that the end of the fiber hangs approximately 0.1 inches above the mold bottom. Best practices for trimming the end of the fiber include:
    a. Remove the protective cap from the fiber and connect to the standard remote module.
    b. Connect the fiber to the ODiSI unit based on the user manual for the ODiSI 6100 and identify the termination return loss and insertion loss data.
    c. Use pliers and cut a small portion of the fiber at a 45° angle to minimize reflection of the laser at the end of the fiber.

d. View the reading on the ODiSI for that fiber and ensure that the cut did not cause the termination return loss and insertion loss to exceed -60 dB and -10dB, respectively.

17. Prepare the fiber(s) to be embedded as follows.

a. Generate the sensor keys for each fiber (refer to Section 2.6.3) for how to do this). The sensor key is a unique ID for each fiber that needs to be loaded into the system.

b. Mark the fibers with a dry erase marker based on the design of depth placement for the distributed strain sensor. A template was created on paper to easily measure and mark the fiber. The key locations to mark are indicated in Figure 2.18: top split shot, top of fiber positioner, and bottom of split shot for both the long and short side of the fiber. The “long” side of the fiber is the end nearest to the spool and the “short” side of the fiber is on the termination end.

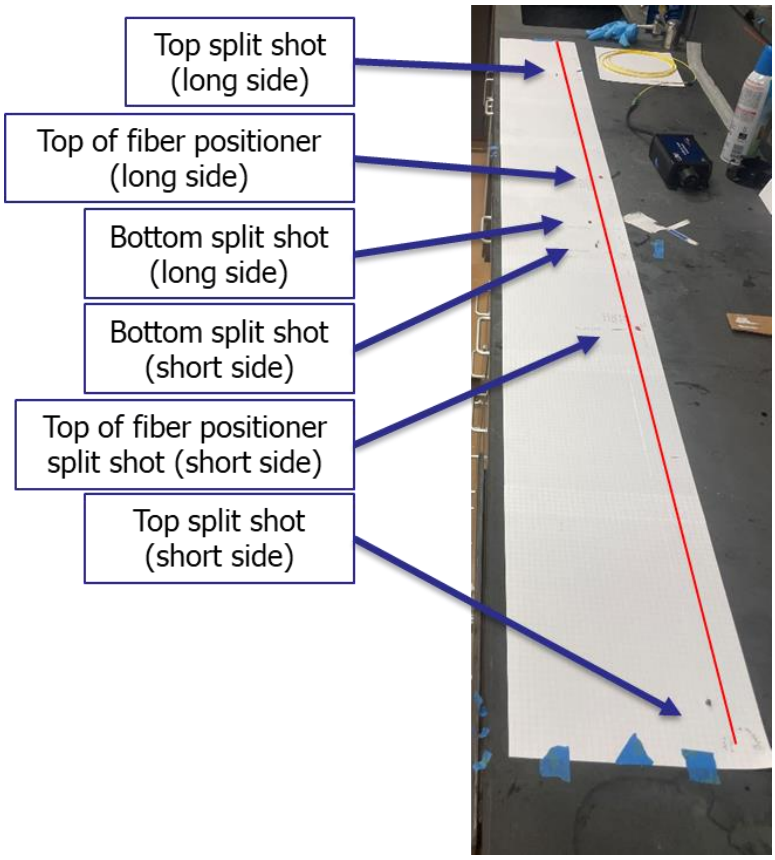

Figure 2.18 Measured and marked template for locating key points along fiber.

c. Create the segments to be used in the system by creating gauges with the "Touch to Locate" feature in the ODiSI software (Figure 2.19). The segments should be located between the top of fiber positioner and the bottom split shots.

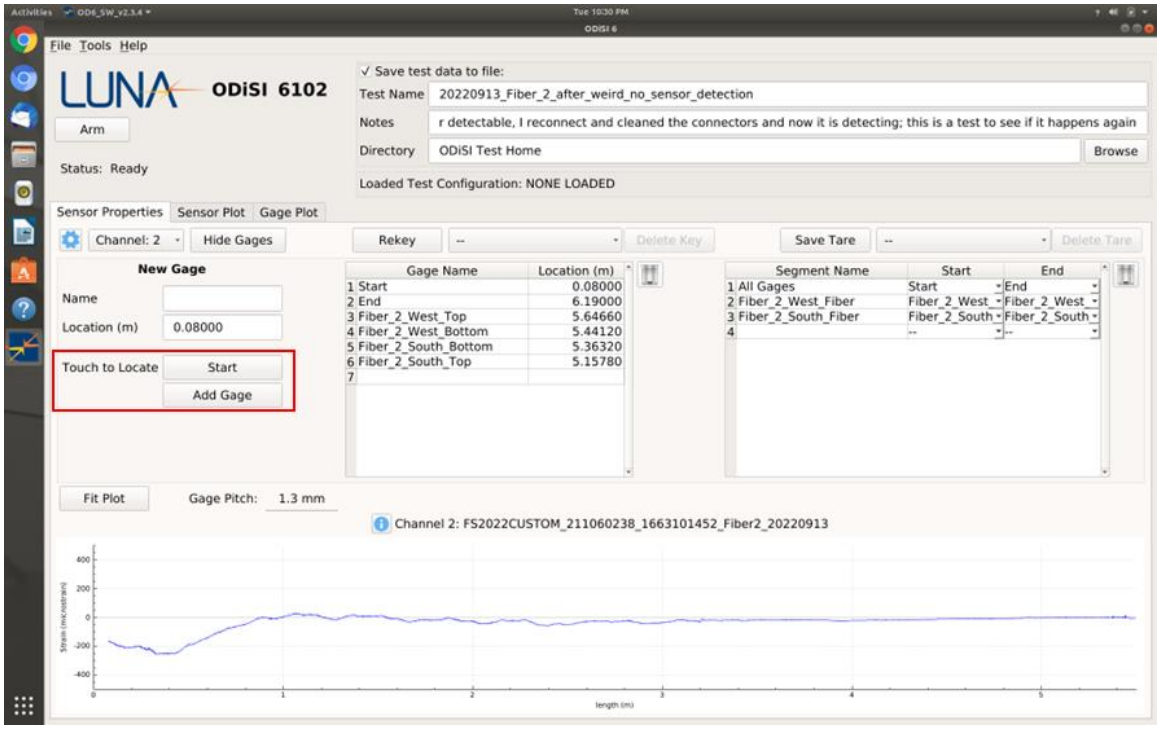

Figure 2.19 Touch to locate feature in the ODISI program.

d. Add four small fishing weights (also known as split shots) each 0.5-grams (size BB) to each fiber based on the markings from the measurement template by placing the fiber in the fishing weight slot and closing the gap with a pair of pliers. The fishing weights used in this experiment are in Figure 2.20. **Safety note:** Use caution not to add them with intense pressure. This can alter the fiber response downstream of the stressed area.

Figure 2.20 Small fishing weights (size BB) used in the experiment.

e. Hang the fibers using the ring stand and bag clips. Position them in the mold with the fiber positioner (Figure 2.21).

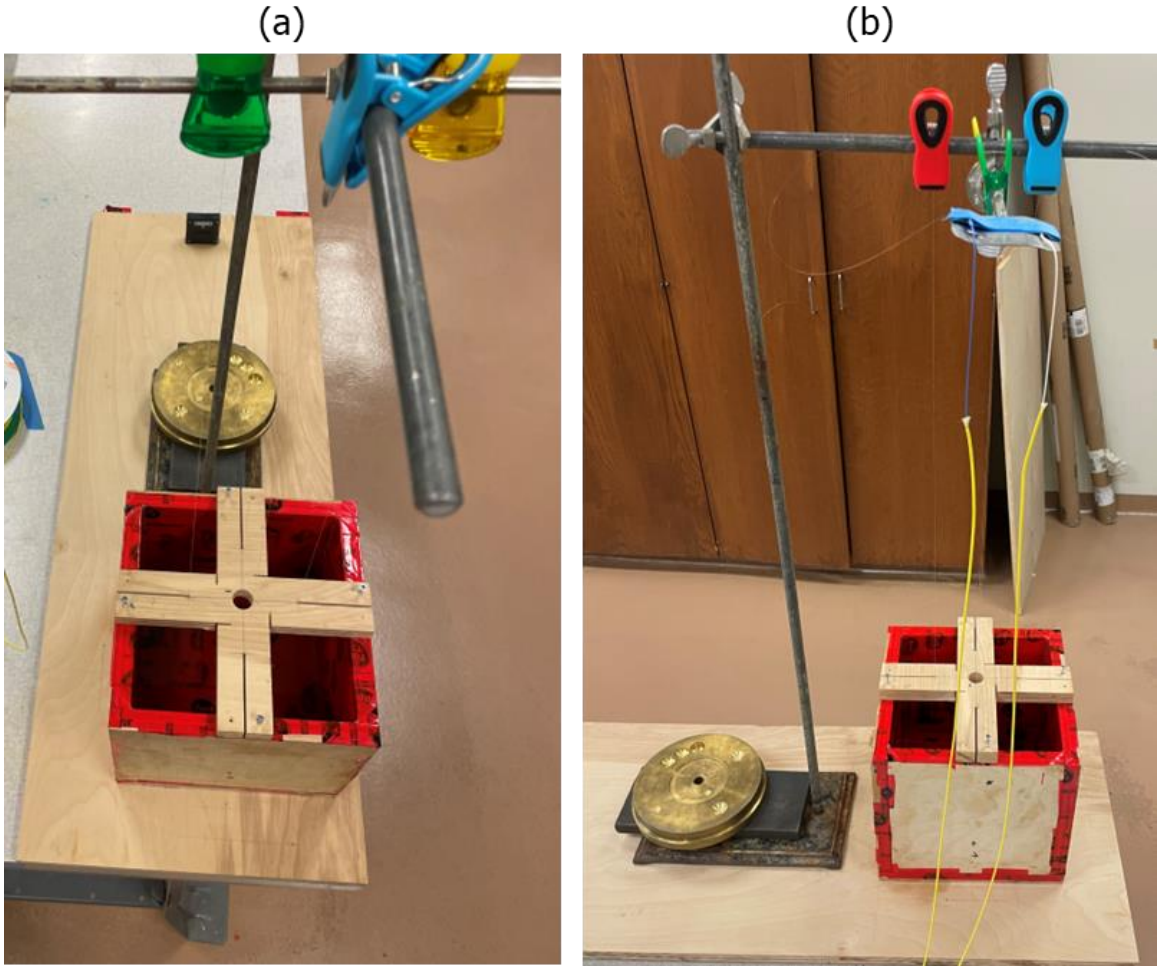

Figure 2.21 (a) Top view and (b) side view of the fibers hanging in the mold with the fiber positioner.

f. Confirm that the fibers do not contact the bottom of mold and measure the height of fishing weight from the bottom of mold.

g. Connect the interrogator unit and confirm the fiber response reading is recordable throughout the testing zone.

h. Record and save a baseline tare measurement of the strain response on the ODiSI. This monitors distortion of the reflected spectrum due to volumetric shrinkage of the epoxy.

i. Disconnect the fiber from the ODiSI unit and put the protective cap back on the end of the fiber.

j. Thread the fibers through appropriate slots in the fiber positioner.

    i. Take one fiber and thread it through the north and east sides. Take the other fiber and thread it through the west and south sides. This eliminates any sort of cross-over between the two fibers.

    ii. Ensure the one" bend radius and that the bottom of the fiber is not touching the mold.

    iii. The east and west fibers should be short ends, while the north and south fibers should be spooled with the remaining fiber, and appropriately spooled and anchored during specimen prep.

k. Clamp fishing weights of 0.5g to the end of the fiber leaving 0.2**"** on the end.

l. Place a marking on the that side twenty-two" away.

m. Then place another split shot 8.1" from the marking.

n. Then place another split shot three" from the last.

o. Mark 8.1" away from the last split shot.

p. Clamp another split shot 21.5**"** away.

q. Round split shot size BB weighing 0.50 grams works well

r. Using magnetic kitchen clips and a metal test tube stand, suspend the fiber in place. Ensure the fiber depth marker aligns with the top of the fiber positioner.

18. If the hanging fiber does not line up over the cross marks at the bottom of the box, the surface on which the mold is resting may not be level, or the box may be slightly non-square. Level the table surface as needed. Figure 2.22 show how the fibers should suspend over the epoxy block held in position by the fiber positioner.

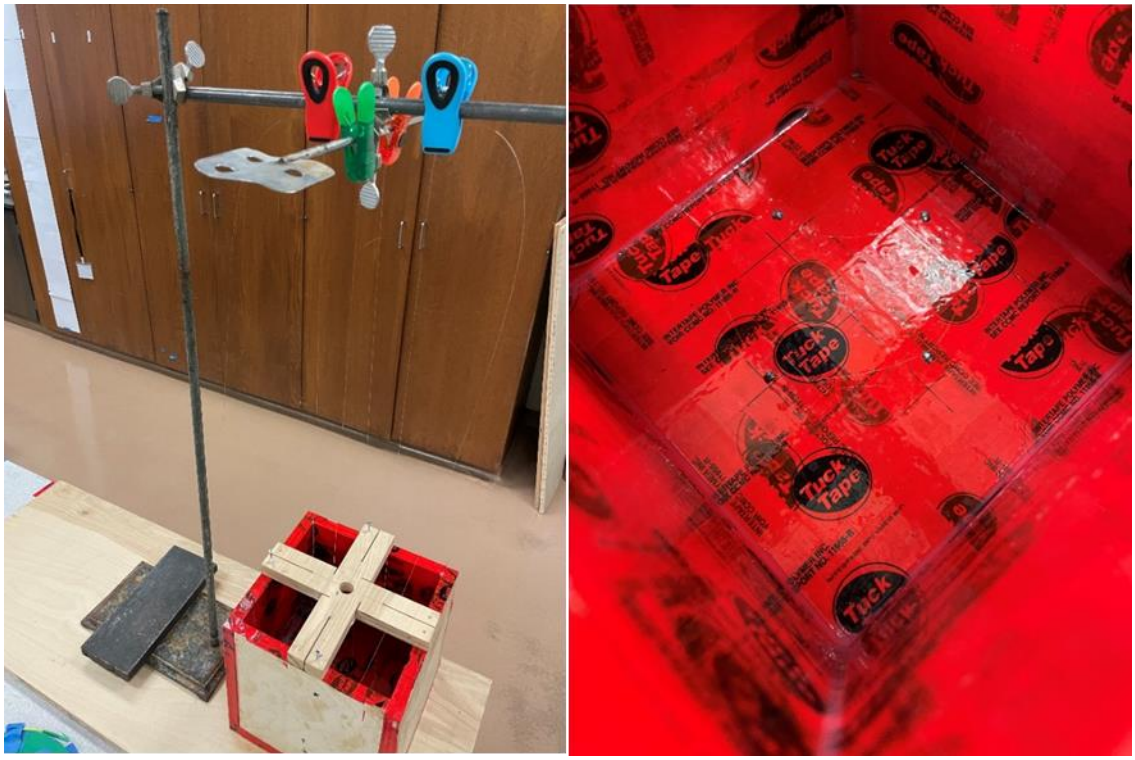

Figure 2.22 Distributed strain senor suspended over the epoxy mold through the fiber positioner (left). Fishing weights hang slightly above the bottom of the epoxy mold two inches offset from the center (right).

Figure 2.23. Close up view of fiber placements in the slots of the fiber positioner.

19. Vacuum the inside of the box to remove any particles that could contaminate the epoxy.
20. Ensure that a one” bend radius is attained.
21. Measure and record the distance from top fishing weights to the bottom of box.
22. Measure and record the angles near the base of the box with a digital angle detector. Ensure that the device is properly calibrated before use.
23. Measure and record the distance from the bottom of the mold to the top of the fiber positioner, one in each quadrant of the box. The measurements are used to determine the actual thickness of each epoxy pour.
24. Mix 987.9 mL (1096.6 grams) of EcoPoxy Flowcast Resin with 494.0 mL (484.09 grams) of EcoPoxy Flowcast Hardener in a plastic beaker. Immediately

stir with an electric mixer and stirring paddle for 3 minutes. Pour the first layer of the epoxy. The volumes provided here should result in an 8-inch x 8-inch x 1.333-inch-thick layer. If modified, the volumetric ratio of resin to hardener should remain at 2:1.

25. Wait 5 to 10 minutes after pouring and look for bubbles. Eliminate them by using a paper clip to disturb them, or by applying brief blasts from a heat gun. Remove any floating particles of debris that the vacuum did not remove. Clean the beaker and stirring paddle with isopropyl alcohol.
26. Repeat steps 22 through 25 to pour layer two, waiting 72 hours between pouring each layer. If the measured thicknesses are not precisely 1.333 inches, consider adjusting the volumes of resin and hardener as needed, always maintaining a 1:2 ratio of hardener to resin by volume.
27. 72 hours after pouring layer two, prop one side of the base plywood to create an angle. Use a wood shim that creates a 5-degree angle as in Figure 2.24. Ensure that the fibers are not contacted when placing the wood shim under the plywood. Properly anchor the wood shim and the plywood down to eliminate any movement. Mark on the table where the material should be placed. Properly account for the distance under the plywood that the propping material is placed. Calculate the expected angle of the new surface in the following ways:
    a. Triangle method: use the distance from edge of table to the location of propping material and the height of the wood shims, to calculate the angle by using trigonometry.

b. Tangent method: measure the height from bottom of plywood to the table at two separate locations and the distance between the two locations to create a trapezoid and determine the angle present.
c. Digital angle indicator: calibrate the digital angle indicator a designated location on the table (not on the plywood that to be tilted). Mark 4 locations on the plywood to be used. A north, west, south, and east location should be selected and should be oriented in the same direction at each location.
d. Magnetic indicator: at the same locations of the digital indicator, use the magnetic indicator to quantify the angle
e. Protractor: determine the angle from the bottom of plywood to the top of table from the pivot side of plywood.

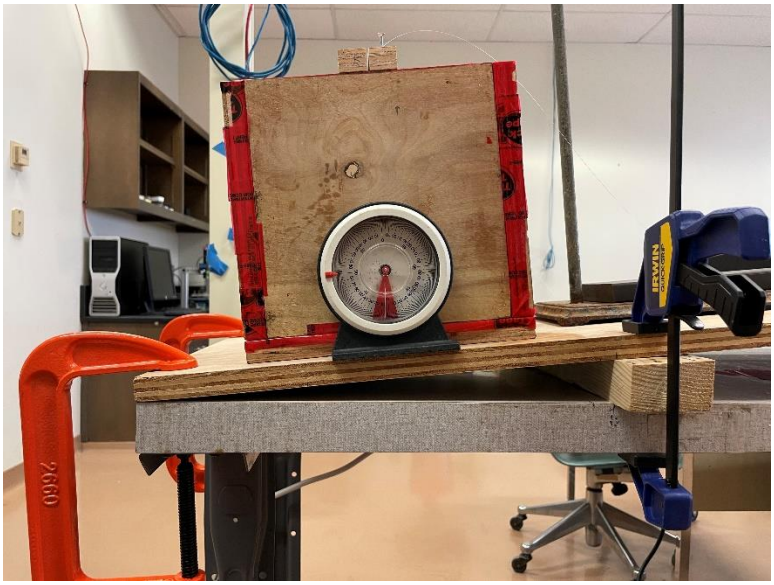

Figure 2.24 Angled and anchored surface to pour third layer of epoxy.

28. Repeat steps 22 through 25 to pour layer three. Since the setup is angled, ensure no sag is present in the fibers.
29. After 72 hours, remove the propping materials from plywood and bring back to original position. Use caution to not hit the fibers.
30. Place the digital angle indicator on top of layer three in the middle. Record this value.
31. Create the initial flaw. Obtain sticker paper from a local print store. Using the punch tool, cut out a 2-inch diameter hole and remove the sticker part. Use the 2-inch diameter non-stick plastic as a guide to cut a 2-inch initial flaw from a piece of sheathing tape. Measure the actual diameter and mark the center of the sheathing tape. Figure 2.25 reflects the required tools and result including a 1-inch radius circular punch, sticker paper, scissors, a template with 1-inch circles.

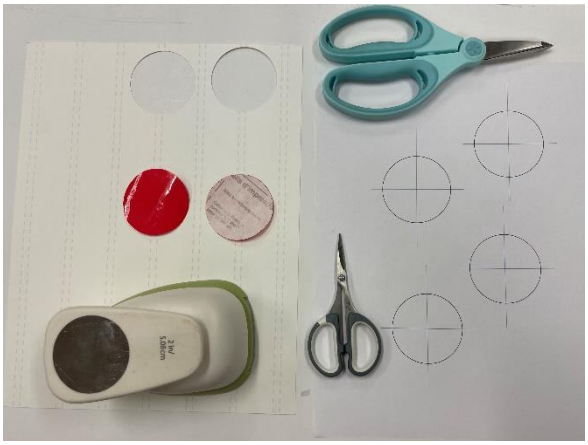

Figure 2.25 Tools used to create the initial flaw.

32. Remove the fiber positioner from the mold. Mark the center location between the two fibers and measure the relative distance between this mark and each fiber, as

well as to the edges of the mold. These measurements are important for accurately knowing the distance from the tip of the initial flaw to the fibers.

33. Mark distances from the centers of cube toward the fibers at 0.25-inch increments. These dots help calibrate the distances on the plane of fracture from the camera angle (Figure 2.26).

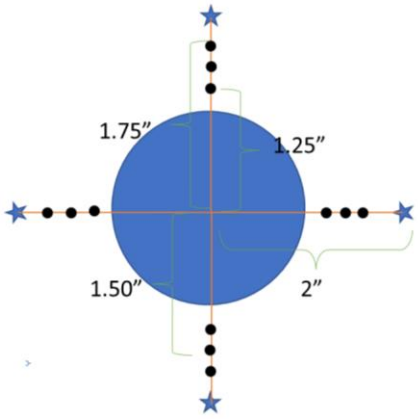

Figure 2.26 Calibration dot configuration around the initial flaw on fracture plane.

34. Carefully place the center of the tape to be used as the initial flaw on the marked center of the block. Measure the shortest distance from the tip of the tape to each fiber. The new center of the cube is not at the original four inches from the edge of block due to the angled plane. The distance is $4/\cos(\theta)$ from the edge of angled plane edges.
35. Repeat steps 22 through 25 to pour the fourth epoxy layer.
36. Measure layer four thickness as in step 23. Reproduced here for simplicity: measure and record the distance from the bottom of the mold to the top of the

fiber positioner, one in each quadrant of the box. The measurements are used to determine the actual thickness of each epoxy pour.

37. Remove the fiber positioner and carefully tape the loose ends of the fibers to the edges of the outside of the block. Mark the center of the block.
38. Use a mill press to drill a ½-inch diameter hole in the middle of the epoxy sample for the injection tubing. Check the mill press alignment with a carpenter square to ensure the drill bit is perpendicular to the drill table. Clamp the model to the mill press table as shown in Figure 2.27. Failure to do this can result in a hazardous scenario where the drill bit catches on the epoxy and spins the entire block.
39. Drill a ½-inch diameter by 1.5- to 1.6-inch-deep hole in the center of the cube that penetrates the center of the flaw tape. The end of a drill bit is tapered; ensure the full ½-inch diameter portion of the bit fully penetrates the initial flaw. Secure the mold with clamps so that the block cannot rotate or rock out of position.

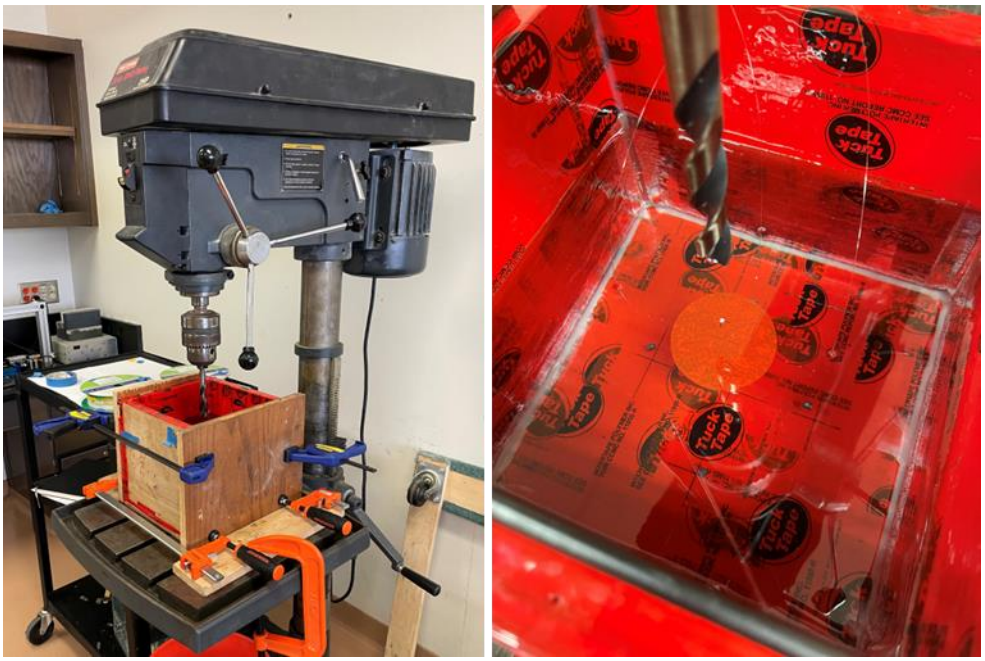

Figure 2.27. Mill press set up used to drill the hole for the injection tubing.

40. Epoxy the injection tubing in place as follows:

    a. Prepare a 5-inch long by ¼-inch diameter by 0.049-inch wall thickness 316 stainless steel tubing open ended on one end with a compression fitting and ¼-inch by one-eighth-inch reducer fitting on the other end. Connect a short piece of 1/8-inch SS tubing and a 6,000-psi rated ball valve to the end with the compression fitting.

    b. Rough up the surface of the tubing with 120 grit sandpaper to improve adhesion with the epoxy.

    c. Slide a Buna N black 70 Shore A (NBR 70) AS568 (#-202) 1/8”x1/4” O-ring over the bare end of the tubing. Measure the O-ring thickness; it should be slightly less than 0.15 inches.

d. Connect the injection tubing to the syringe pump. Fill the tubing with distilled water mixed with two drops of food coloring per milliliter of water. Ensure the system is purged of air. Slide the tubing through the fiber positioner.

e. Insert the tubing into the hole in the epoxy block. Use a stand and clamps to support the tubing and to hold it in the center of the hole. Position the O-ring such that it is approximately 0.1 inches above the initial flaw. This can be verified by measuring the distance from the top of epoxy layer four to the top of the O-ring, which should be 1 to 1.1 inches for a 1.333-inch-thick epoxy layer.

f. Set the syringe pump at 0.25 mL/min, and slowly fill the anulus beneath the O-ring with dyed water. The goal is to purge air from the system. Look for air pockets trapped beneath the O-ring. If water rises above the O-ring, remove it with a fine tipped syringe.

g. Fill the tubing-hole annulus with 5-minute instant mix Loctite epoxy. Work out any air bubbles with a paper clip. Wipe away excess epoxy that spills over. Wait approximately 1 hour for the epoxy to harden before proceeding.

Figure 2.28. Injection tubing before (left) and after (right) layer four is poured.

41. Secure the injection tubing with no stored energy and eliminate it from accidently springing free and damaging the fibers or epoxy. Screw the fiber positioner back on and re-align the fibers.
42. Repeat steps 22 through 25 to pour layers five and six. Wait one week after layer six is poured. Measure layer six height and calculate the actual thickness of the block.
43. Remove the block from the mold by gently prying the mold sides and bottom off with a flathead screwdriver. Enlist help from a second person to avoid damaging the fibers.
44. Smooth the north and south faces as needed since these are the planes that withstand the load. Proceed to test the block according to the fracture test procedure.

2.6. Strain Measurements

Strains were measured at four offset locations from the injection tubing, each 2-inches from the center of the angled fracture (Figure 2.10). The strains were obtained with an ODiSI 6100, and high-definition strain sensors were used. This section details the equipment specifications and the methods used to obtain strain measurements. Figure 2.29 depicts the strain sensing equipment. The dedicated instrument controller is the user interface with the equipment and is connected to the interrogator unit that emits the laser pulses and measures the backscattered intensity. The standoff cables and remote modules serve as an extension and connection of the fibers to the interrogator unit.

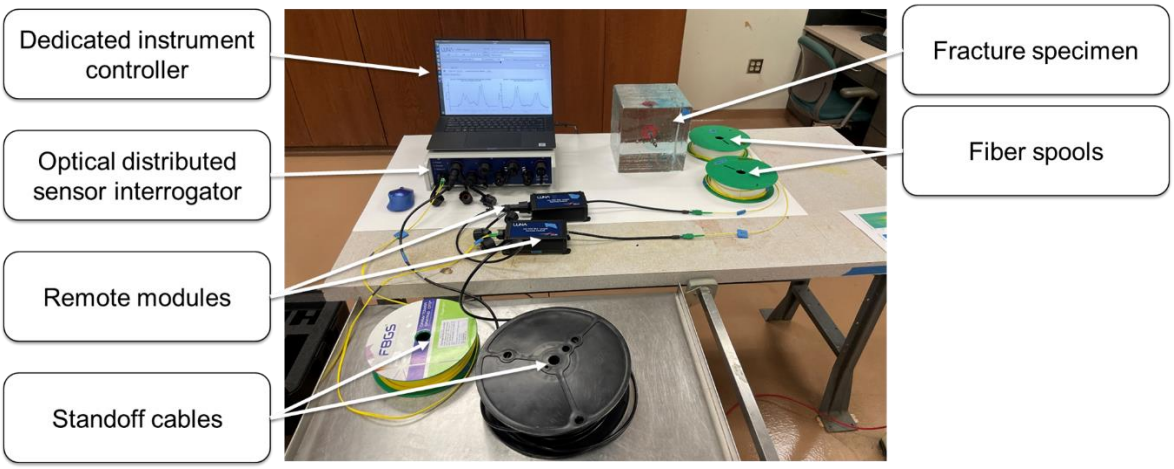

Figure 2.29 Operational set up for fiber optic sensing equipment.

2.6.1. High-Definition Fiber Optic Strain Sensor Design

The following details the specification of the fibers and interrogator unit used for the experiment. The properties high-definition strain sensors are indicated in Table 2.2. The fiber design must have adequate length to reach the interrogation unit equipment during the fracture injection test. A fiber length of at least one meter is recommended between

the edge of the sample and the end of the fiber in order to reach the interrogator unit with the given experimental apparatus.

Table 2.2 High-definition strain sensor properties.

Design Variable	Suggested Specification
Fiber type	Flexible, polyimide low bend loss
Cladding Diameter	127 µm
Coating Diameter	203 µm
Coating	Ormocer-T

2.6.2. Fiber Optic Interrogator Unit Specifications

The interrogator unit used for the experiment was the ODiSI 6100 with two available channels. This unit can obtain strain data using optical fibers with spatial resolution as low as 0.65 nm. The high-definition fiber optic sensing technique is driven by Rayleigh backscatter measurements in the fiber optic sensors. The sensors are provided with a unique sensor key with pre-calibrated coefficients to provide seamless integration for utilization. Table 2.2 identifies the interrogator unit configuration during the experiment while recording strain data and Table 2.3 represents the performance specifications with the ODiSI 6100 at the operations parameters identified in Table 2.4.

Table 2.3 Operational parameters for the fracture injection experiment.

Design Variable	Suggested Specification	Notes
Gage Pitch	0.65 mm	Used to capture the high changes in strain along fiber
Measurement Rate Per Channel	6.25 Hz	Depends on sensor length, measurement mode, gage pitch, performance mode, and number of channels
Performance Mode	Full optimization	Used to obtain high quality strain measurements at half of maximum rate

Table 2.4 Performance specifications at operational parameters for the fracture injection experiment (Luna 2021).

Parameter	Specification*
Strain measurement range	±15,000 με
Resolution	0.1 με
Instrument Accuracy	±1 με
System Accuracy	±25 με
Measurement Uncertainty at zero strain	±5 με

**με represents the microstrains measured by the interrogator unit.*

2.6.3. Procedure to Obtain Strain Data from ODiSI Program

Safety section: It is important to follow recommended safe practices when working with fiber optic cables. Safe practices include never looking at the end of a fiber optic cable that is plugged in to the laser interrogator or looking into a port on the interrogator. Doing so could cause serious eye damage. Gloves should also be utilized to avoid glass fiber particles from penetrating the skin while cutting fibers. Hands should be washed thoroughly to avoid accidental ingestion of fiber particles. Ingesting fiber particles can lead to damage of internal organs. This is not an exhaustive list of safe fiber handling practices.

The following procedure describes how to use the ODiSI V2.3.4 program for strain data acquisition.

1. Open OD6_SW_v2.3.4 program (LUNA, 2022) from desktop shortcut. Allow the system to initialize and show a “ready” status before proceeding.

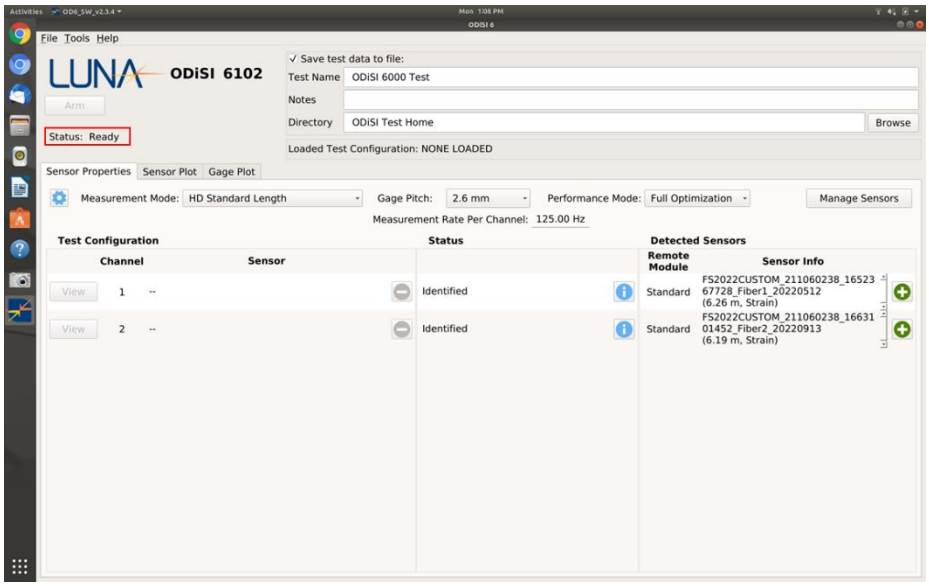

Figure 2.30 Main ODiSI 6 software window after successful initialization.

2. Import the sensors (only needs to be completed the first time the sensors are connected).

    a. Click the “Manage Sensors” button.

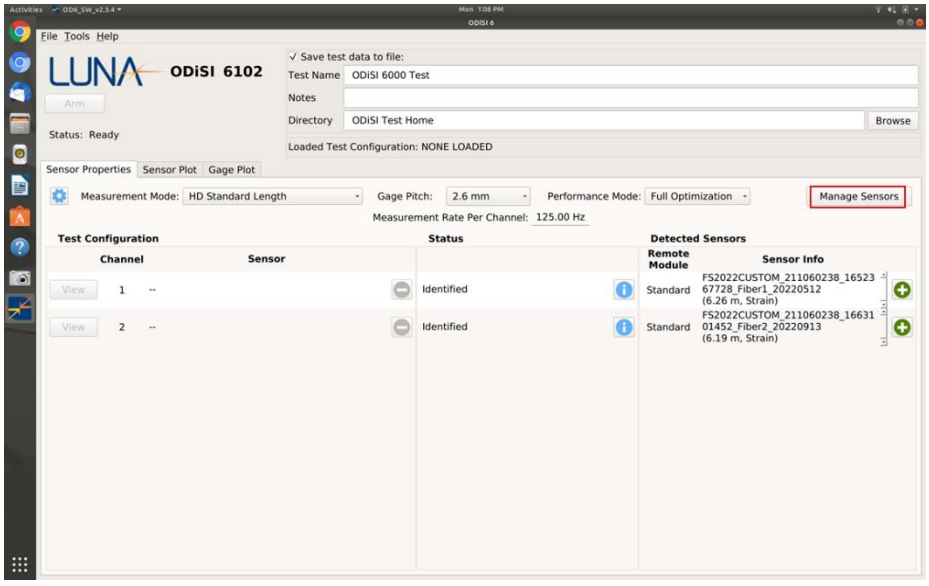

Figure 2.31 Interface window to manage sensors.

b. Click the “Import Sensors” button and select the “USB Drive” button.

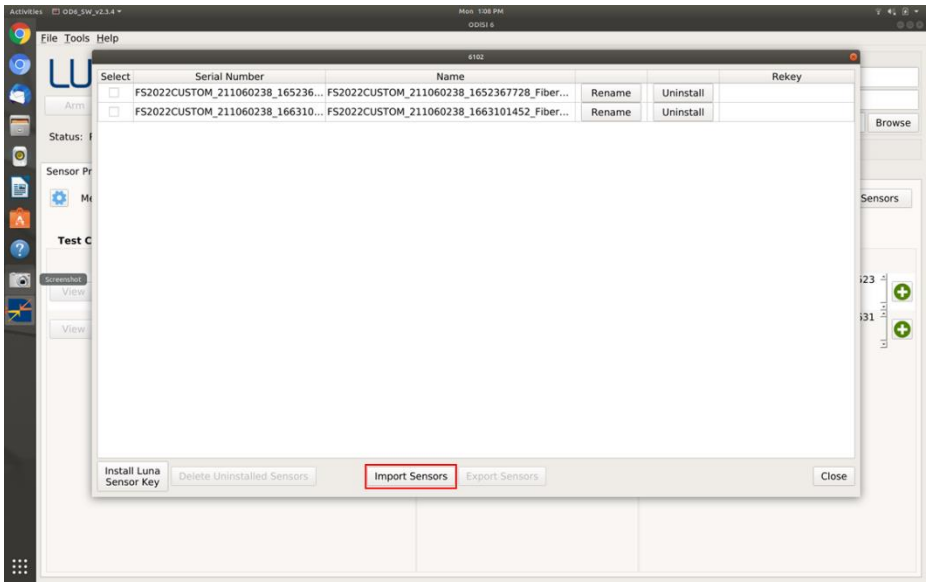

Figure 2.32 Sensor management window.

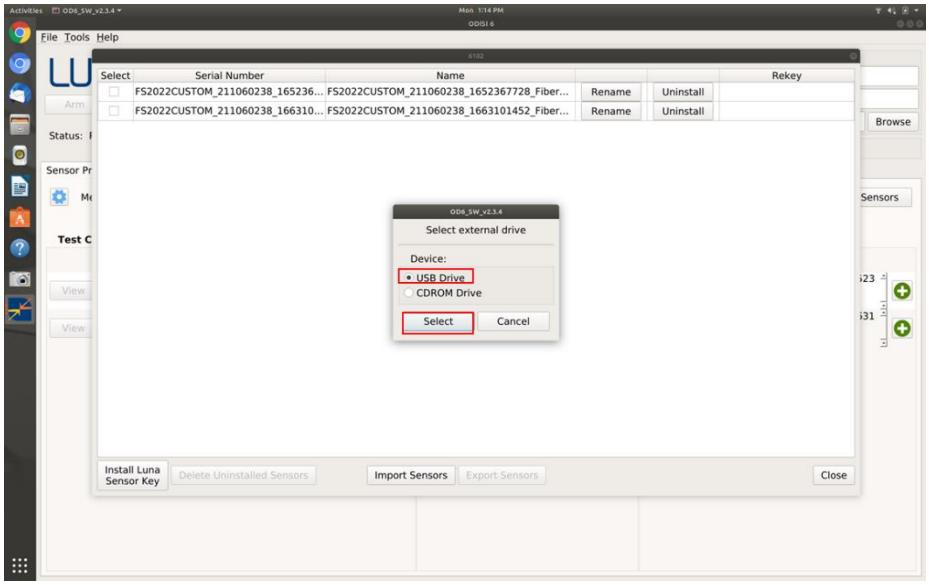

Figure 2.33 Select drive to import sensors.

c. Select the appropriate sensor keys that came with the associated sensors via the USB drive.

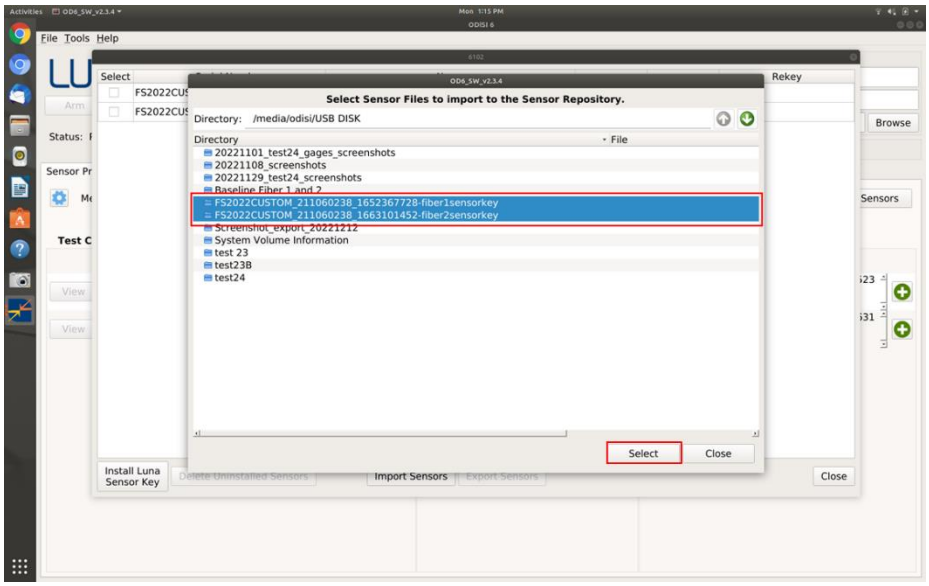

Figure 2.34 Select the sensor keys to import into program.

d. Click the “Close” button to return to main interface.

3. Add the identified sensors to the channel configuration by clicking the green plus signs.

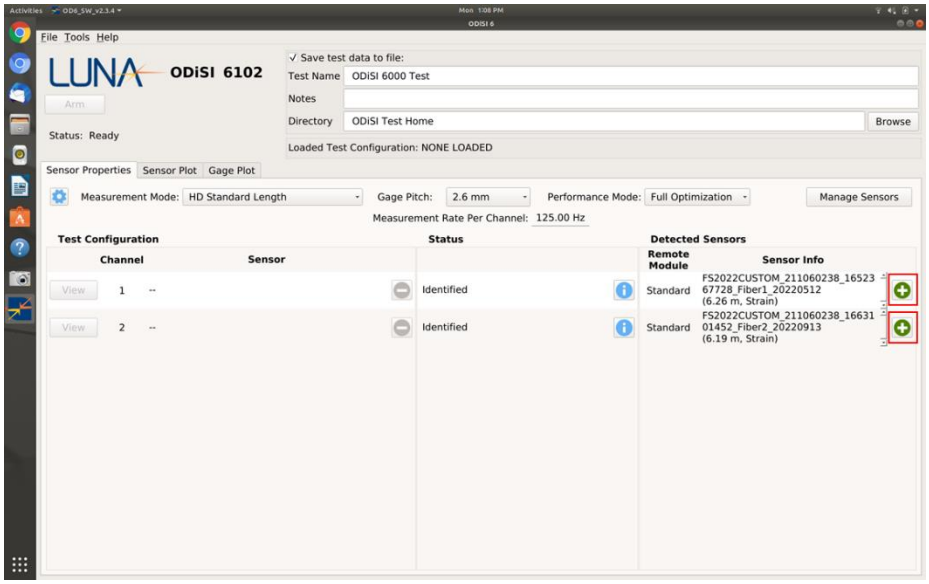

Figure 2.35 Add sensors to configuration.

a. If identification errors with the fibers occur, view the details of the sensors by clicking the blue information dots.

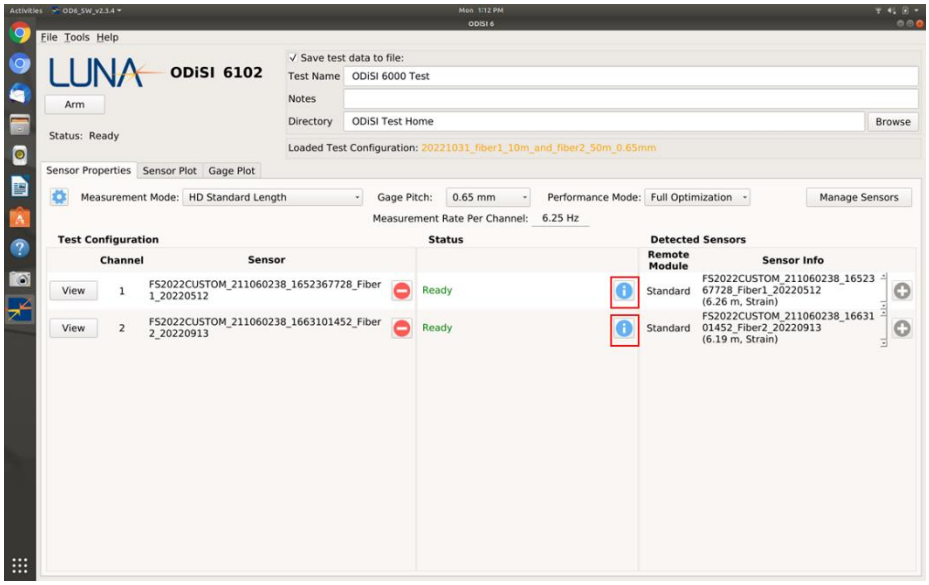

Figure 2.36 Review the sensor details.

b. Click the “Advanced” button.

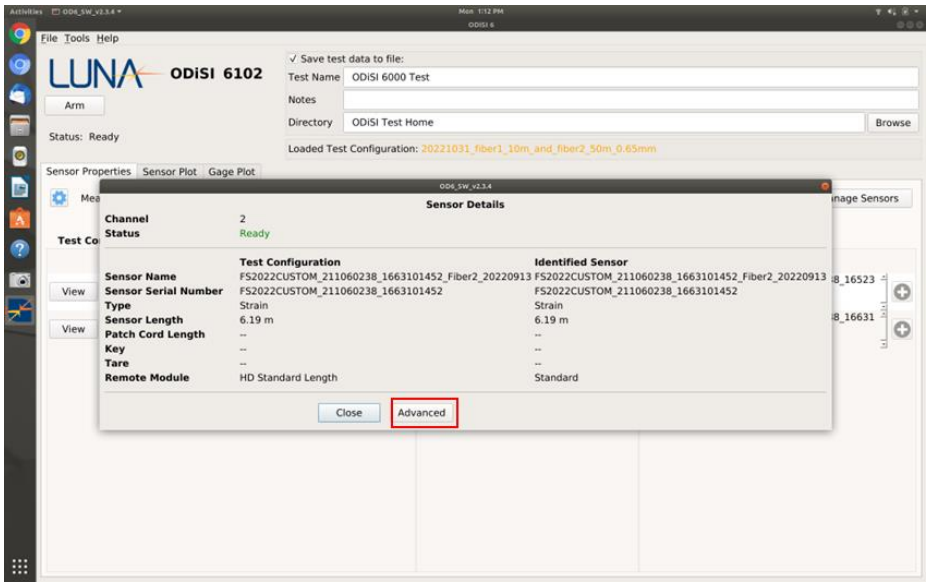

Figure 2.37 Review the advanced settings.

c. View the return loss and insertion loss measurements for the connector and termination ends of the fiber. Ensure that the return and insertion loss are within the constraints indicated in Table 2.5.

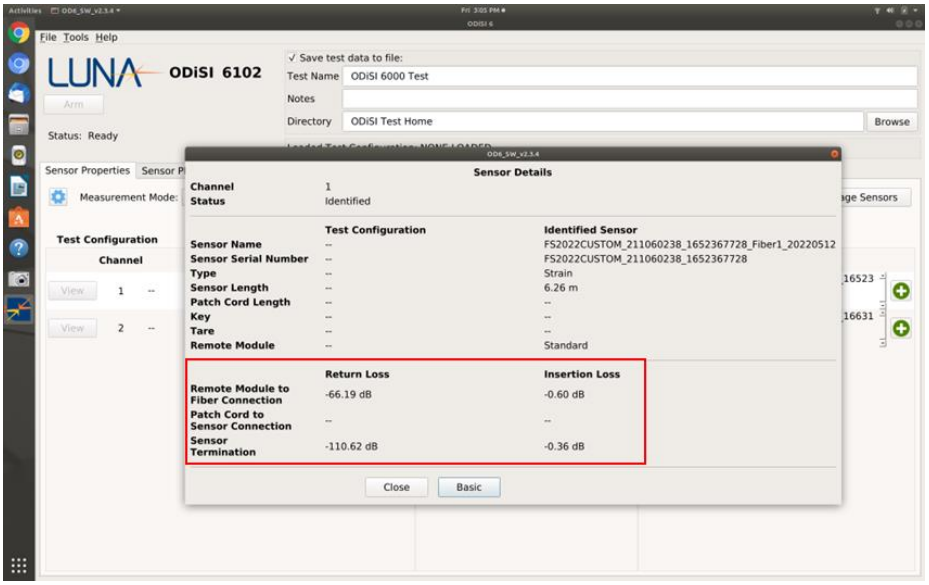

Figure 2.38 Ensure the return loss and termination loss are stabilized and identified.

Table 2.5 Connector and termination constraints for return loss and insertion loss (adapted from Luna 2021).

	Return loss (dB)	**Insertion loss (dB)**
Connector	-87.5 < RL < -60	IL > -0.5
Termination	RL < -60	IL < -10

4. Prepare test configuration (only required the first time, skip to step 5 if test configuration has already been created and saved).

   a. Click the settings icon.

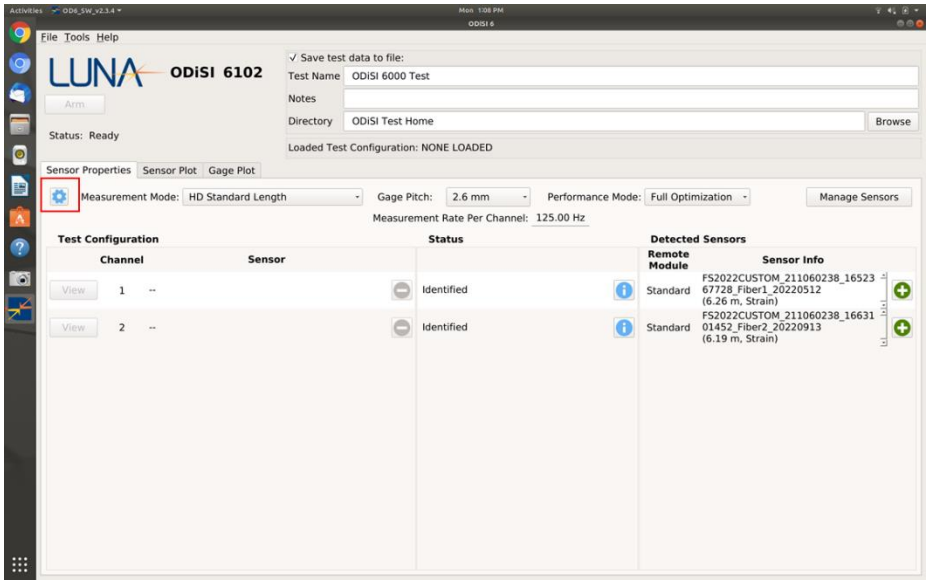

Figure 2.39 Open channel settings.

b. Under the “Channel Settings” tab, select the appropriate standoff cable lengths in use. Click the “Apply” button, then click the “Ok” button to confirm the standoff cable lengths.

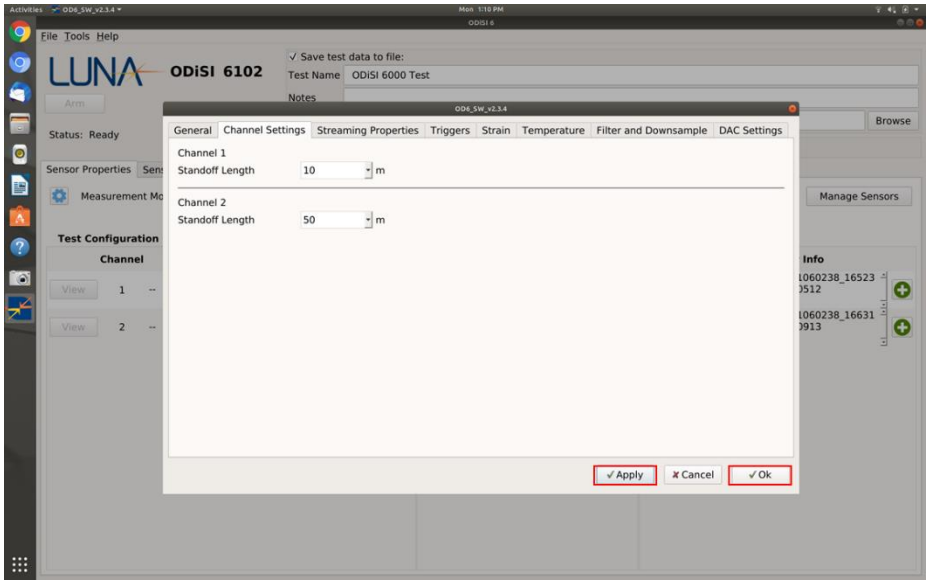

Figure 2.40 Adjust channel settings based on standoff cable lengths.

c. From the drop-down menus, set the “Gage Pitch” to and the “Performance Mode.”

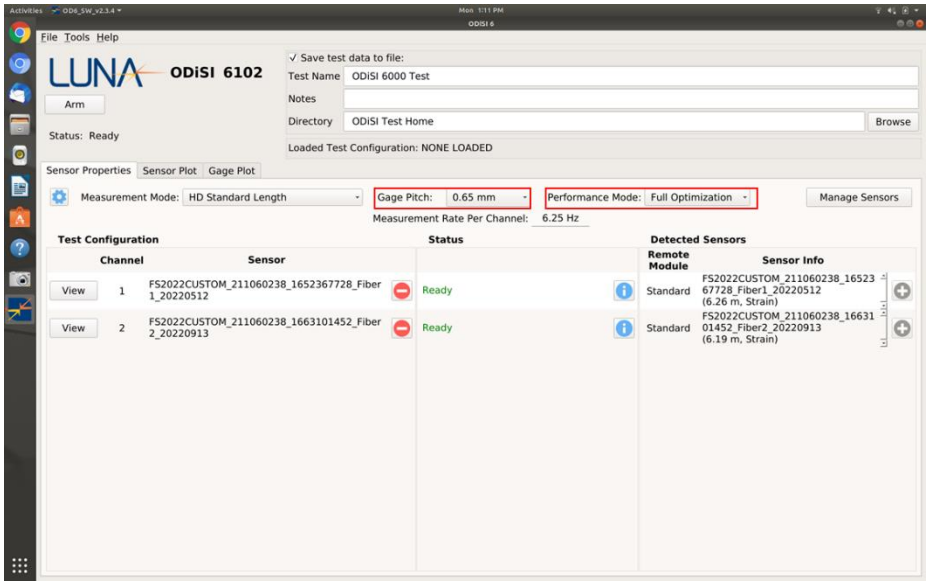

Figure 2.41 Configure the operational parameters (gage pitch and performance mode).

d. Under the “File” directory, select “Save Configuration…”

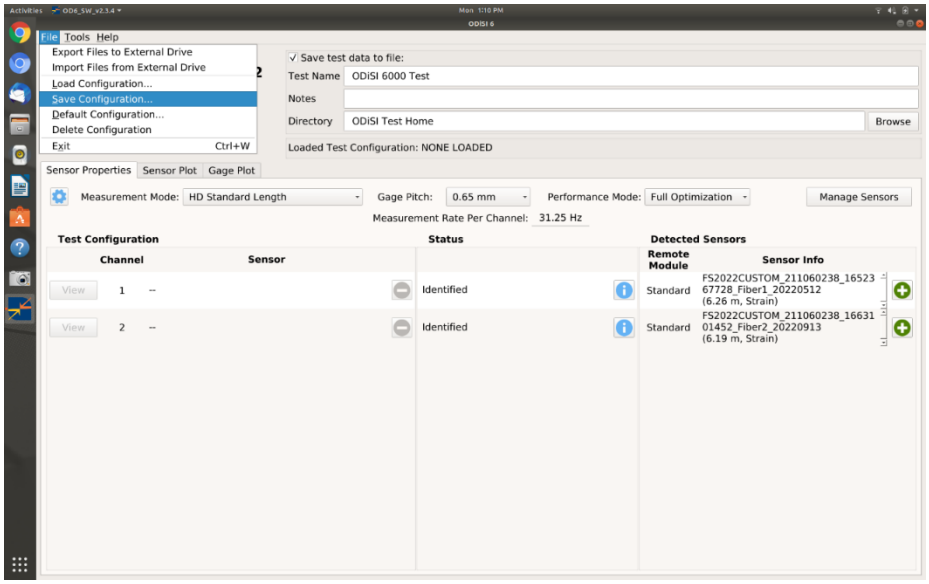

Figure 2.42 Save the configuration.

5. Load the proper test configuration.

    a. Under the “File” directory, select “Load Configuration….”

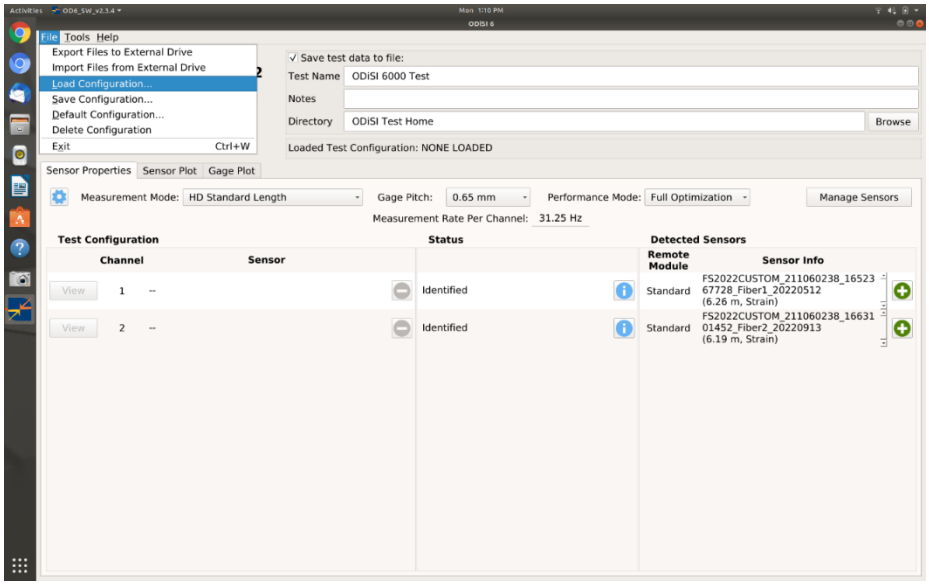

Figure 2.43 Load the desired configuration.

b. Ensure the desired configuration has been set. Incorrect settings can lead to incomplete datasets.

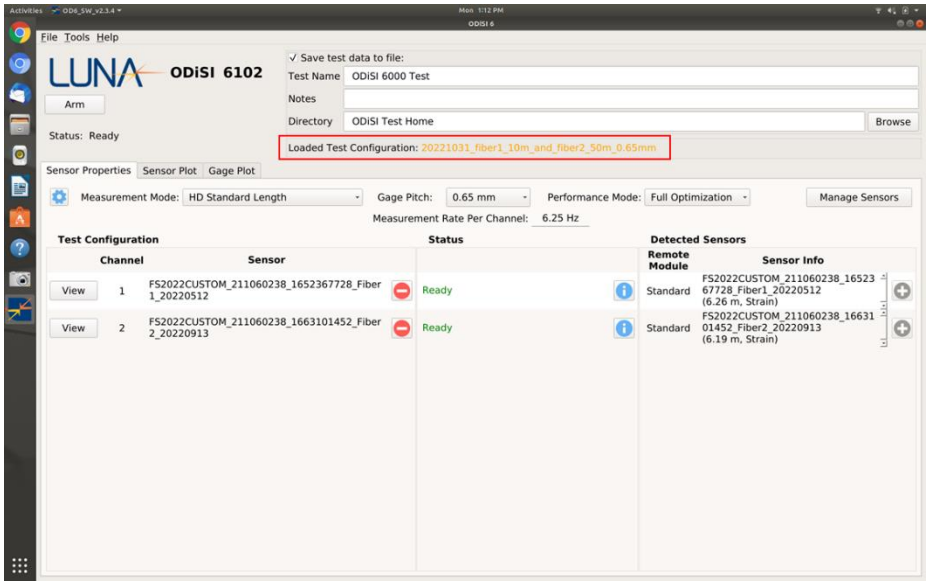

Figure 2.44 Ensure the desired configuration has been loaded.

6. Manage sensor settings by clicking “View” next to a sensor.
    a. Click the “Fit Plot” button to auto-adjust the axes to observe the strain data along the sensor.
    b. Click the “Save Tare” button and name the tare. This zeroes out the strains along the length of the sensor.
    c. Select the tare that to be used during the test from the drop-down menu of the saved tares.
    d. (Optional) Define key points of interest along the sensor as segments by creating gages.
7. Run a test from the main interface.

a. Set the data file settings by checking the “Save test data to file” and naming the test with details in the notes area. Select directory to store the data in.

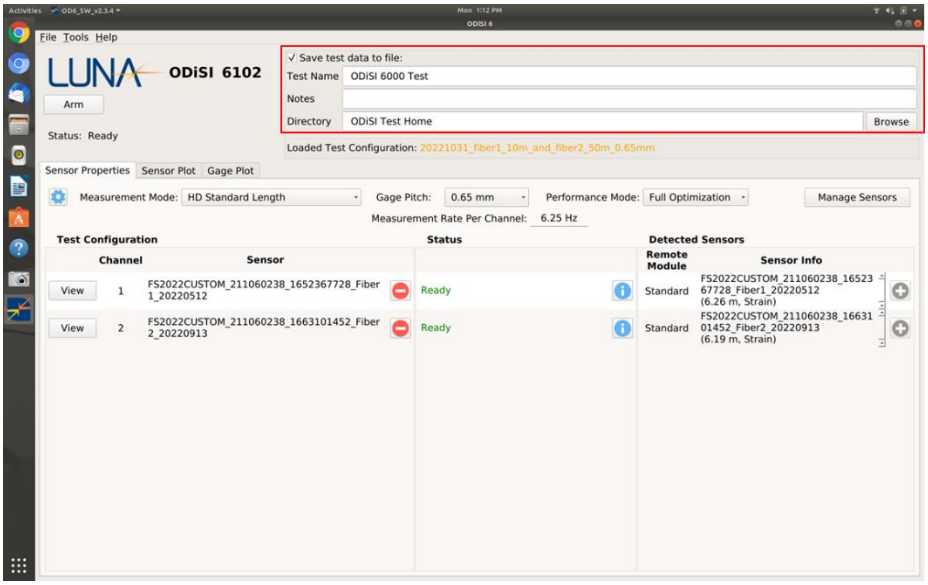

Figure 2.45 Name and set directory to save test data.

b. Click the “Arm” button to prepare the ODiSI unit to collect data.

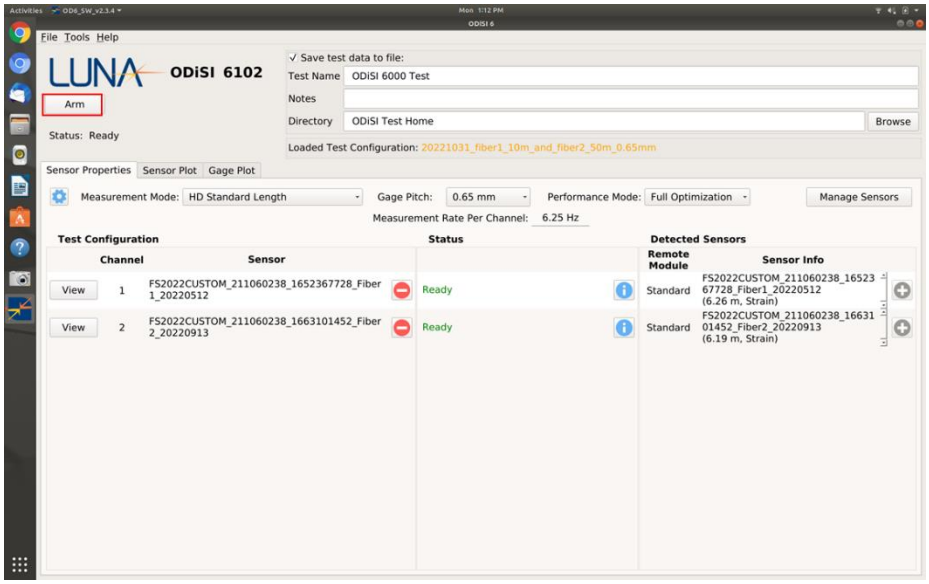

Figure 2.46 Arm the system once system is prepared to acquire data.

c. Start the test by clicking the “Start” button.” This automatically brings the strain data for each fiber to the screen.

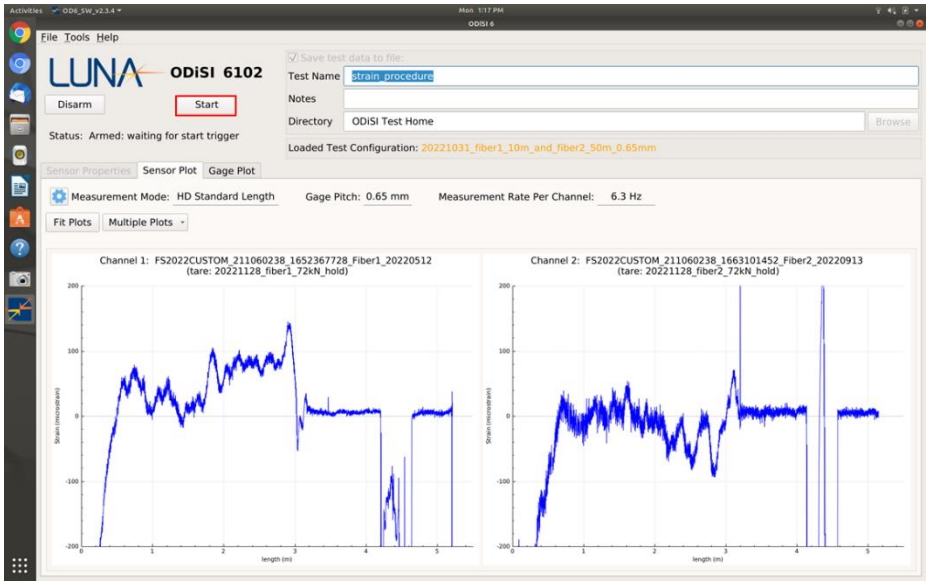

Figure 2.47 Start the data acquisition.

d. Once the data acquisition is complete, select the “Disarm” button followed by the “Stop” button.

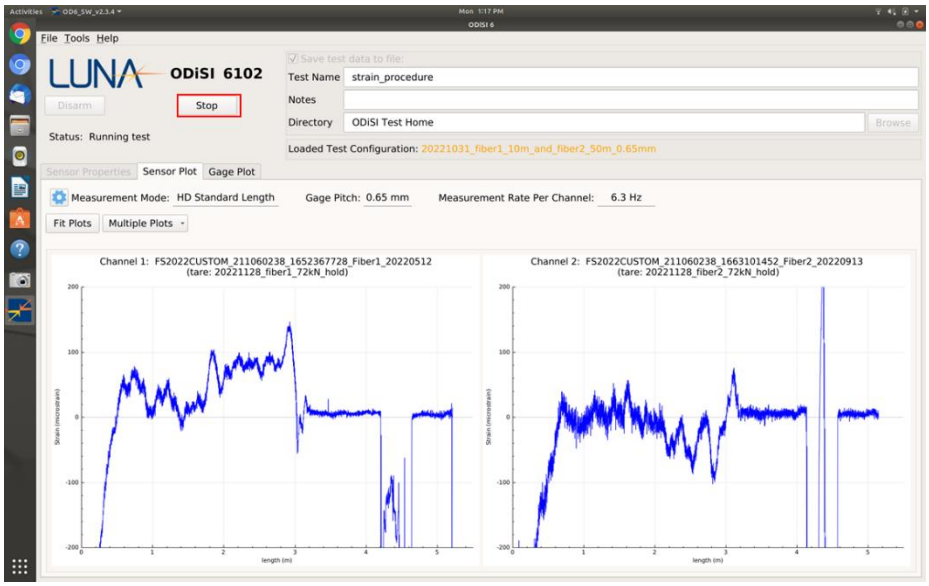

Figure 2.48 Stop data acquisition after test.

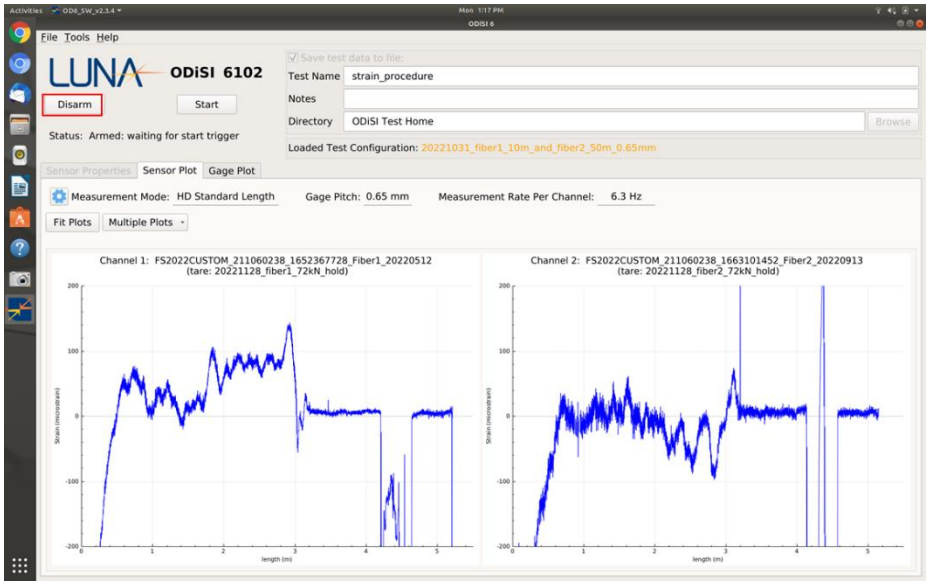

Figure 2.49 Disarm the system from acquiring data.

8. Export the raw data to ascii format for use in external platforms.

    a. Under the “Tools” directory, select “Generate Test Data TSV Files.”

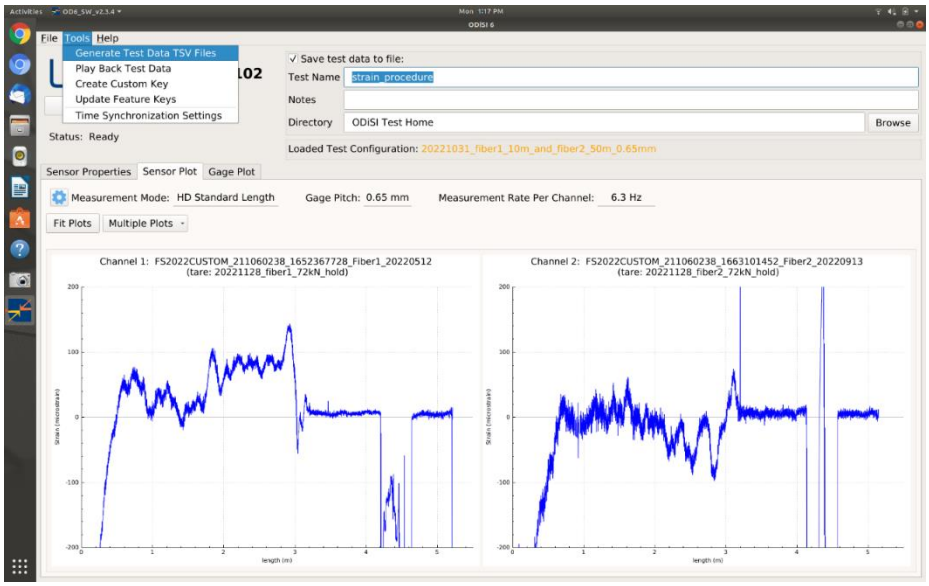

Figure 2.50 Export the test data files.

    b. Select the data to be extracted, click the “Add” button then click “Save.”

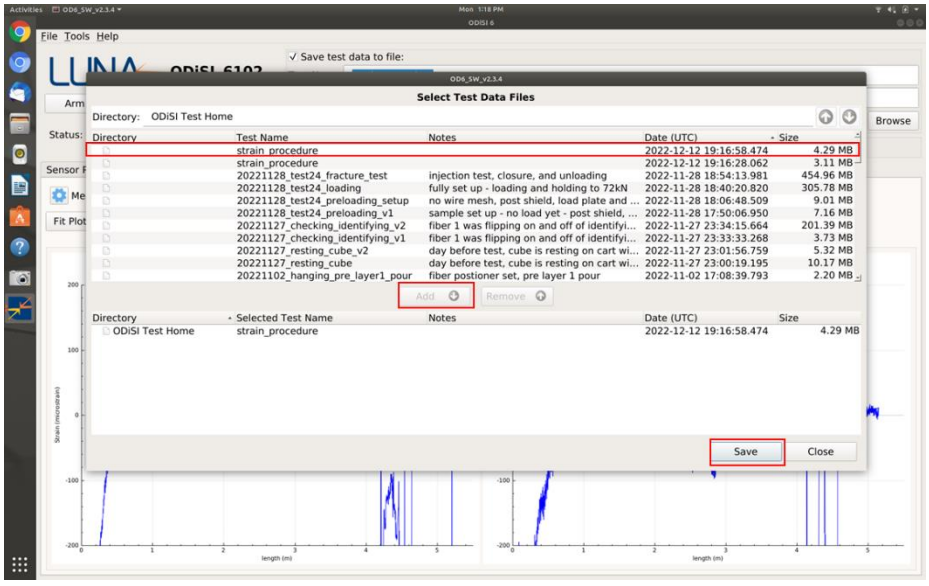

Figure 2.51 Select the data file to be exported.

c. Select the file directory and the amount of data to be extracted.

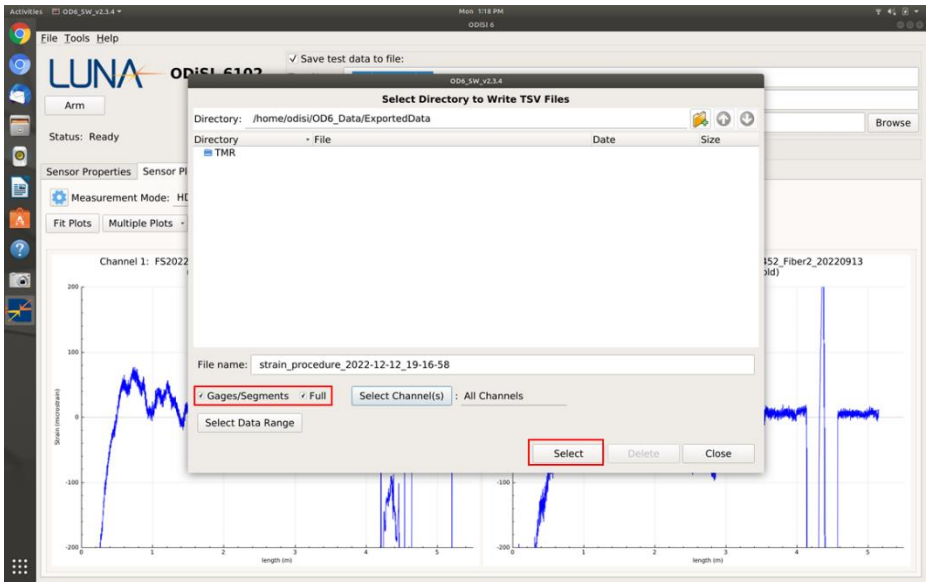

Figure 2.52 Select the quantity of data from test file to be exported.

2.7. Fracture Test Procedure

This section details the procedure for performing the fracture test with embedded optical fibers.

Safety section: Wear proper eye protection, lab coats, and gloves. Be familiar with the location of emergency shut down buttons. Ensure at least two people are present to handle a block with fibers in it to avoid damaging the fibers when moving the block. Utilize proper shielding materials during loading and injection phases.

1. Ensure all valves are closed on the syringe pump.
2. Set up the sample in load frame as in Figure 2.53:
    a. Place the shield under the load frame.

b. Place the epoxy specimen in the load cell with the North side facing up to the load frame.
c. Place the steel plate on top of the north side.
d. Place the spacer above the steel plate.
e. Orient the injection tubing upwards over the shield.
f. Organize the fibers to be arranged to go above the shield. Ensure the fibers are not blocking the camera view of fracture geometry.
g. Close shield and arrange the wire mesh in three layers around the load frame – make sure the tubing and fibers are still accessible. Wire mesh needs to be securely fastened with no chance of falling. If wire mesh were to fall, fibers could break.

Figure 2.53 Sample in load cell oriented for injection test (shield is not pictured for clarity of set up).

3. Set up the syringe pump as follows:
    a. Fill the syringe pump with dyed water to an initial volume of approximately 6.5 milliliters.
    b. Set the desired flow rate (0.25 mL/min suggested) and run it to make sure it is correct.
    c. Set the desired refill flow rate (0.1 mL/min suggested) to simulate flowback/fracture closure.
    d. Ensure all the valves are open to the correct positions to inject water into the epoxy cube. If valves are replaced, ensure they have a pressure rating of at least 2,000 psi.

e. Record the initial volume of the syringe pump.

f. Ensure the maximum syringe pump output pressure is set at 2,000 psi.

4. Open the LabVIEW file: "Hydraulic_Fracture_test_data_collection_producer_consumer.vi" and perform a test to make sure the pressure data is saving properly.

    a. Press "Run"

    b. Check the "write to file settings" and test the program to make sure it is saving pressure data in an accessible location.

    c. Record and save a pressure data file to ensure data acquisition and file directory.

5. Set up two GoPro cameras to capture footage of the experiment. Position one camera to view the initial flaw and fracture propagation. This camera should be aligned precisely parallel to the plane containing the initial flaw. Position another camera to visualize any water leaking along the pipe. Consider the following:

    a. Place a neutral background behind the cube in the line of the camera. A white piece of posterboard, for instance.

    b. Ensure the cameras have enough memory to capture the anticipated duration of the experiment.

6. Connect the fibers to the ODiSI unit and open the OD6 data acquisition program.

7. Create and save two tares of the fibers while load plate and spacer are resting on cube.

8. Ensure all measurement devices have sufficient memory for the acquisitions. Typical data acquisition sizes for the experiment are listed in Table 2.6.

Table 2.6 Data acquisition memory requirements.

Data Acquisition	Capacity (GB)
Video	10
Pressure	1
Load cell	1
Strain	2

9. Ensure the computer clocks for the computers recording pressure, strain data, and load frame are synchronized to within 0.1 seconds. Check this by simultaneously entering with the “time” command on command prompt of both computers. Record any time differences.
    a. Prepare the load frame computer and software. The program should apply a constant load of 72 kN.
10. Record and save a test fiber acquisition on the following settings: 0.65 mm, 6.25 Hz and full optimization.
11. Open the valves on the outlet side of the syringe pump.
12. Check that the pressure is reading 0 psi.
13. Start the video recording on both cameras. Make sure the cameras are stable and not oscillating.
14. Countdown “3, 2, 1, 0” for the video audio to pick up. Simultaneously on “0”:
    a. Start the pressure acquisition.
    b. Start the fiber data acquisition.
15. Then begin loading the sample.

a. Start the load frame – load in 5 kN increments up to 65 kN allow stabilization after each increase.
b. Continue to load in increments of 1 kN up to 72 kN.

16. After the load is stabilized, stop the fiber data acquisition, and save and record a new tare for each fiber.
17. Stop the video and pressure data. Ensure to save the data. Reset the file save directory for the pressure data.
18. Start the video recording on both cameras. Make sure the cameras are stable and not oscillating.
19. Countdown "3, 2, 1, 0" for the video audio to pick up. Simultaneously on "0":
    a. Start the pressure acquisition.
    b. Start the fiber data acquisition.
20. Ensure that the cameras are recording, and the pressure and fiber data are actively recording.
21. Soon after, press the start button on the syringe pump.
22. Monitor the pressure and frac growth. When the fracture is ½ inches away from the edge of the block, stop the pump.
23. Immediately record the volume of the syringe pump, and then run the pump in reverse to simulate fracture closure. Do this by pressing "Refill" on the pump controller. A rate equal to or less than the injection rate is recommended.
24. Record the final volume of syringe pump.
25. Monitor the pressure. Stop the syringe pump when the pressure reaches 0 psi.

26. Reduce load to zero kN in increments of 5kN to 60kN and then by increments of ten kN increments to zero kN.
27. Stop the pressure acquisition. Stop the OD6 data recording. Collect the saved files (pressure, volumes, load, axial displacement, videos, etc.).
28. Disconnect the syringe pump from epoxy tubing and disconnect the fibers with care.
29. Remove the wire mesh.
30. Carefully open the shield, remove load cell plate, and epoxy specimen
31. Remove shield and clean surfaces of load cell.

3. EXPERIMENTAL RESULTS AND DISCUSSION

This chapter presents results from the hydraulic fracture lab experiment with embedded fiber optic cables. The results include fracture geometry and pressure measurements. The measured strains in the experiment are presented in numerous ways: digital format, waterfall plots, strains at singular time steps, strains at singular locations on the fiber, and cumulative strains across the fiber or during injection period. The application of the zero-strain location method for this experiment is discussed. Lastly, the finite element analysis modeling is compared with the experimental observations.

3.1. Fracture Radius and Pressure

The fracture geometry captured during the experiment is depicted in Figure 3.1 and Figure 3.2. The four embedded fibers are represented by the white cross markings offset in the north, south, east, and west directions 2-inches from the center of the fracture. Figure 3.1a shows the status before the experiment started. As the water is injected, it breaks past the initial flaw at 505 seconds as shown in Figure 3.1b. The fracture continues to grow in Figure 3.1c. At 616 seconds, the east fiber is intersected by the fracture depicted in Figure 3.1d and Figure 3.2a. The fracture propagates passing the east fiber as it approaches the north and south fibers (Figure 3.2b and Figure 3.2c). The experiment ends at 737 seconds because the fracture grew past the boundary of the cube, as shown near 712 seconds in Figure 3.2d.

The unexpected fracture propagation behavior toward the west fiber may be a result of undesirable impurities on the surface of the fracture plane (e.g., small dust particles that were not removed prior to pouring layer 4 or a scratch on the top of layer

3). Between 0 and 505 seconds the initial flaw is filled with water. The fracture takes an eccentric radial form after the fracture hits the east fiber. As the fracture propagates closer to the east edge of the cube, boundary effects are observed to make an impact, given the non-radial shape that the fracture assumes Figure 3.2d.

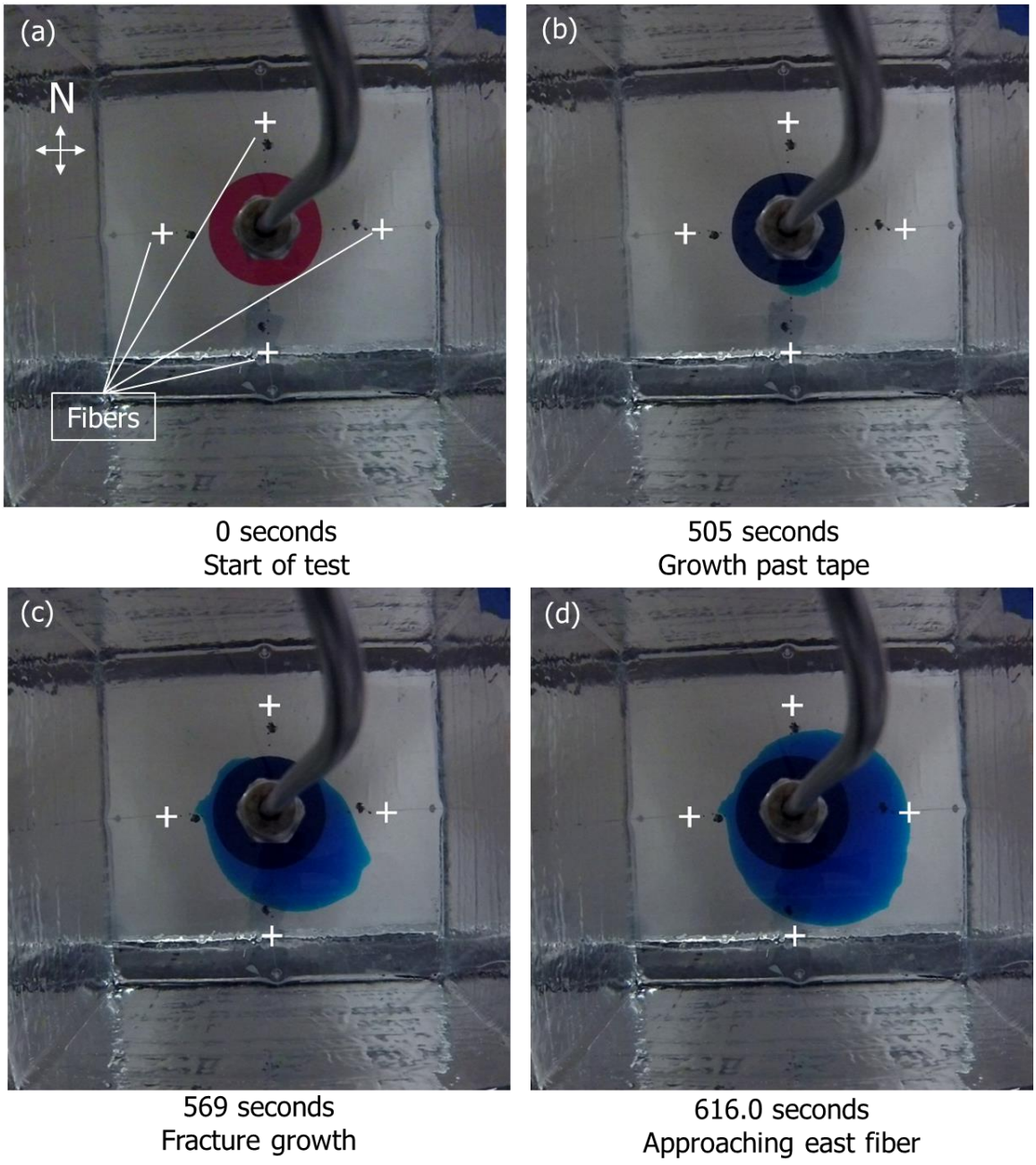

Figure 3.1 Fracture geometry evolution approaching the fiber during injection test.

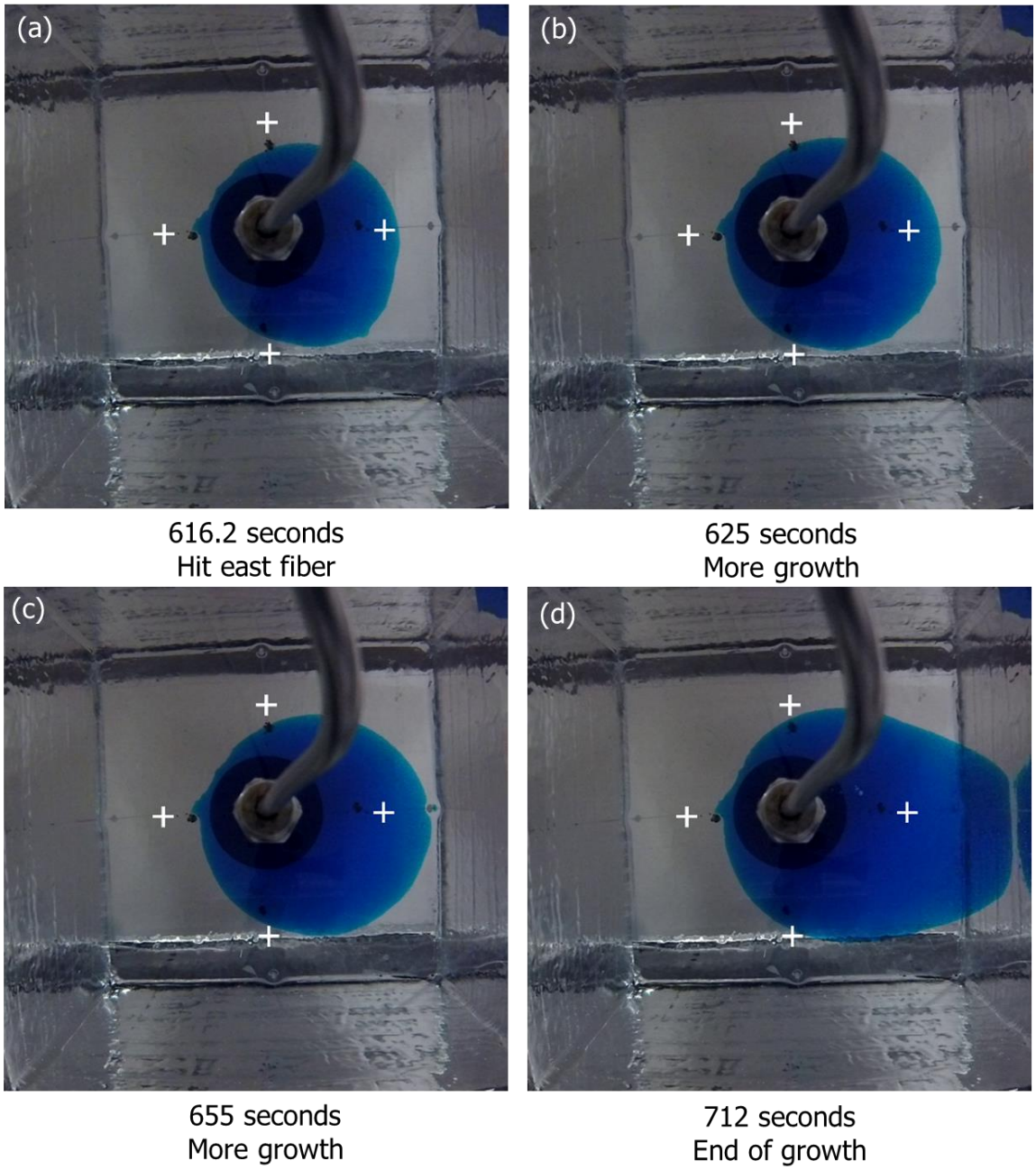

Figure 3.2 Fracture geometry evolution after fiber interception during injection.

The measured pressure and fracture radius are plotted with injection rate in Figure 3.3. The valves from the syringe pump to the epoxy were opened at 27 seconds. The

injection began at 67 seconds. The initial flaw did not receive water until 472 seconds based on the fracture video. At 472 seconds, the water went into the area of the initial flaw. At 505 seconds, the fracture started propagating into the epoxy, passing the initial flaw. The radius increased in incremental steps up until 737 seconds. Each drop in pressure from 505 to 737 seconds corresponds to a step increment in fracture radius. Figure 3.4 is an enlarged picture of pressure and fracture radius during the time of 450 seconds to the end of the test. The red lines show the correspondence of pressure drops to spurts of fracture growth. The results throughout this section will focus on the measurements during fracture growth which occurred from 450 to 750 seconds.

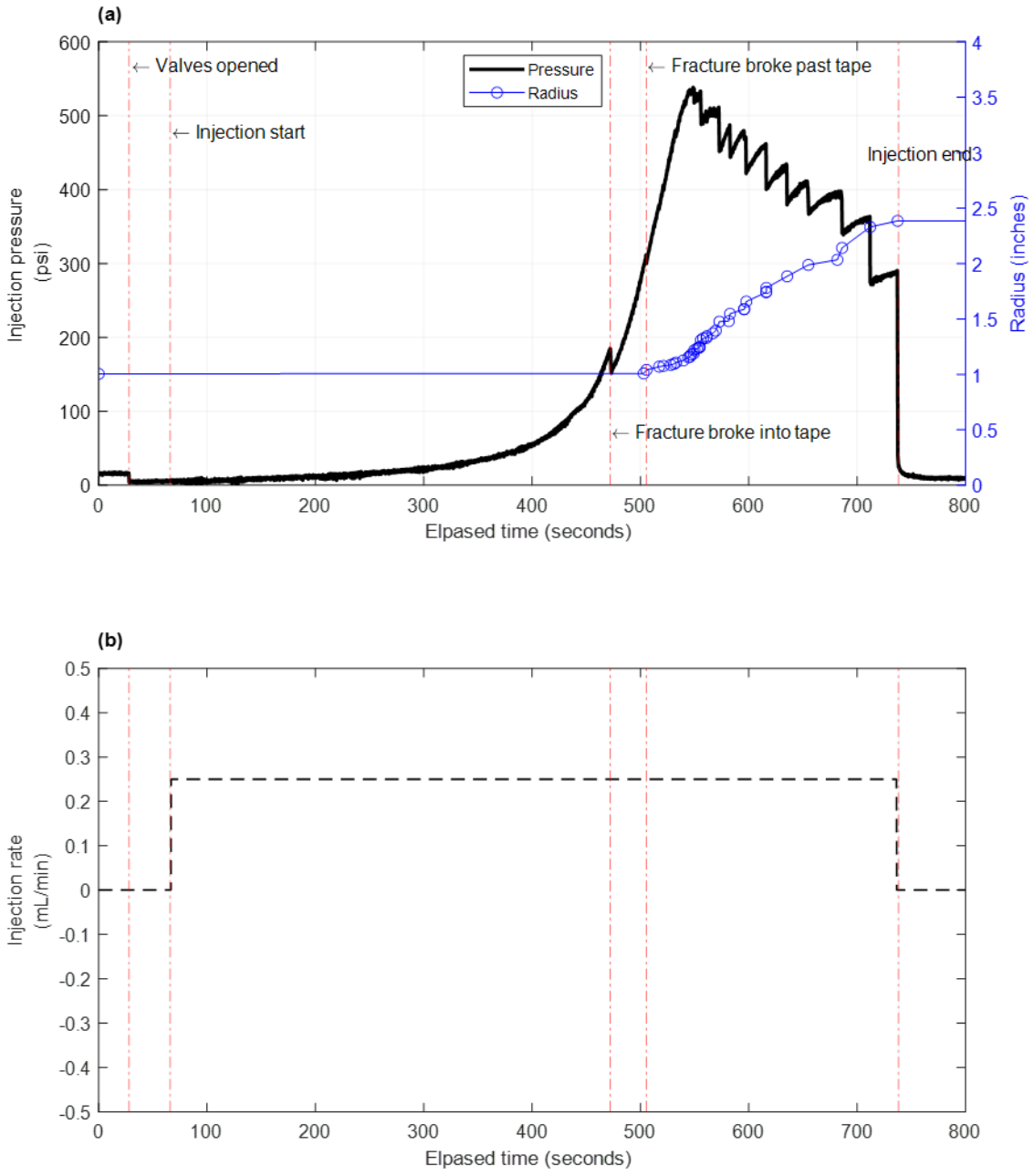

Figure 3.3 (a) Measured pressure (black) and fracture radius (blue) with (b) injection rate (dashed) for duration of experiment.

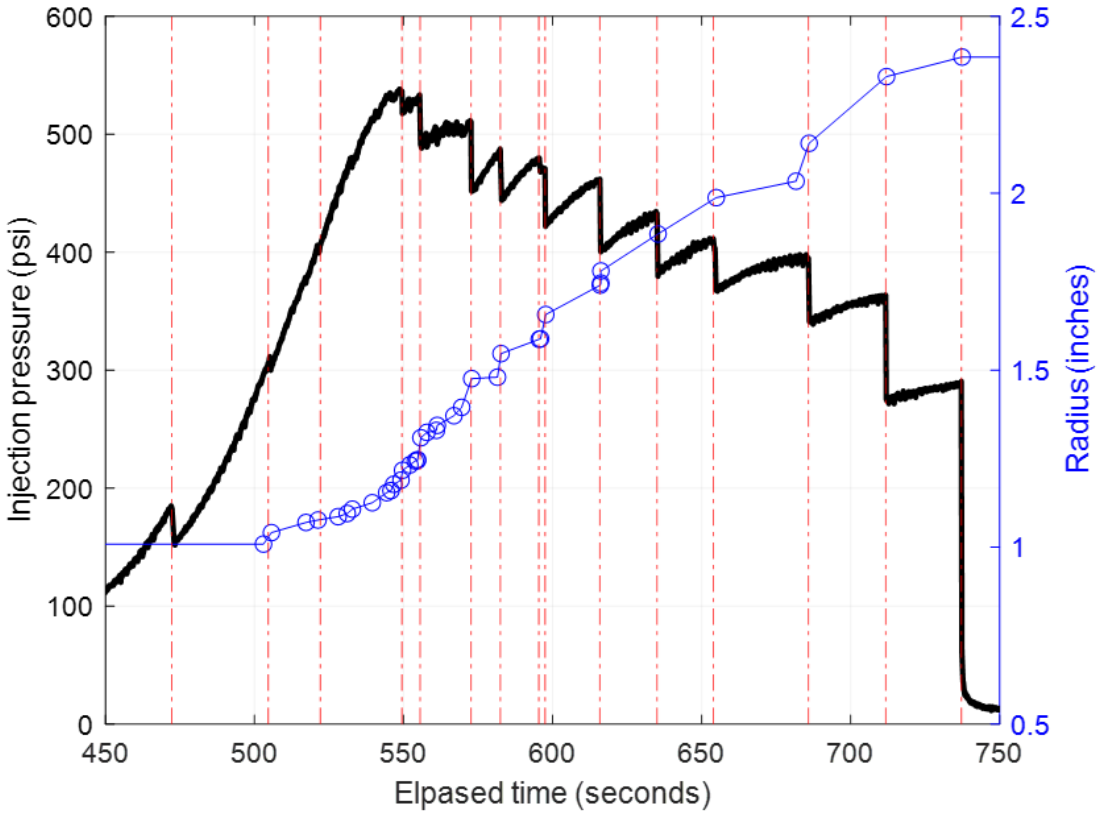

Figure 3.4 Focused area of measured pressure (black) and fracture radius (blue) during primary fracture growth period.

3.2. Waterfall Plots

LF-DAS data is typically visualized in 2D contour plots called waterfall plots that illustrate the intensity of strain or strain rate (color scale) at each time (along x-axis) and measured depth (along y-axis). Figure 3.5a and Figure 3.5b represent examples of waterfall plots from a field study and from a lab experiment, respectively.

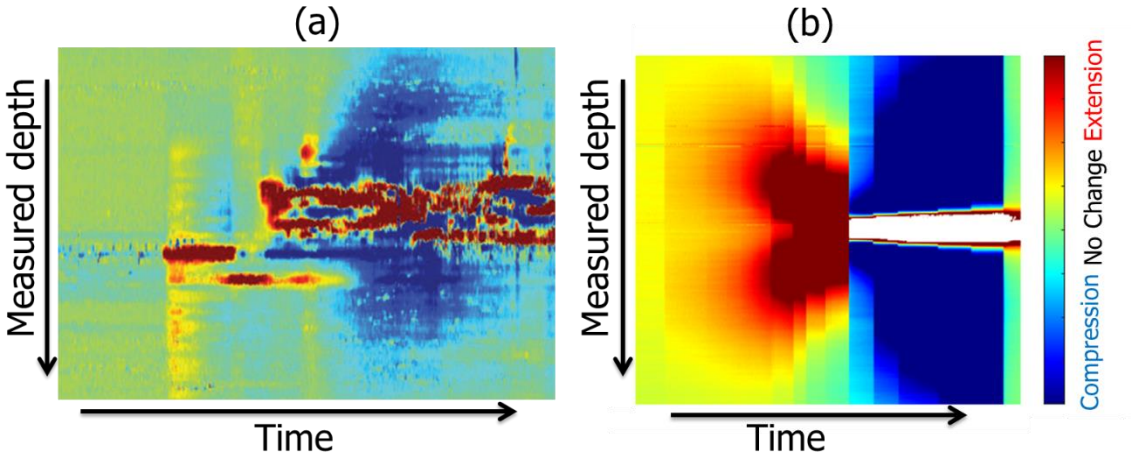

Figure 3.5 Examples of strain waterfall plots from (a) field case (Jin and Roy, 2017) and (b) a laboratory experiment.

Waterfall plots comparative to field results are presented at the experiment level of strain and strain rate waterfall plots as a function of time and distance from the fracture plane. The digital format of the strain data provided from the interrogator unit is a ".txt" format. A snapshot of this data is provided in Figure 3.6 as an example. The strains are provided in a matrix format, where the columns are locations along the fiber and the rows are at each time a measurement was recorded. Processing of the data consisted of converting the real time to elapsed time from experiment start and converting the location along the fiber to the distance from the fracture plane. For each fiber there were over 300 measurement locations along the fiber at 6,600 time steps resulting in over 2-millon strain measurements per fiber. MATLAB was utilized to generate waterfall plots from the digital files; they focus on the time of fracture growth (450-750 seconds) and ±2.5 inches around the fracture plane.

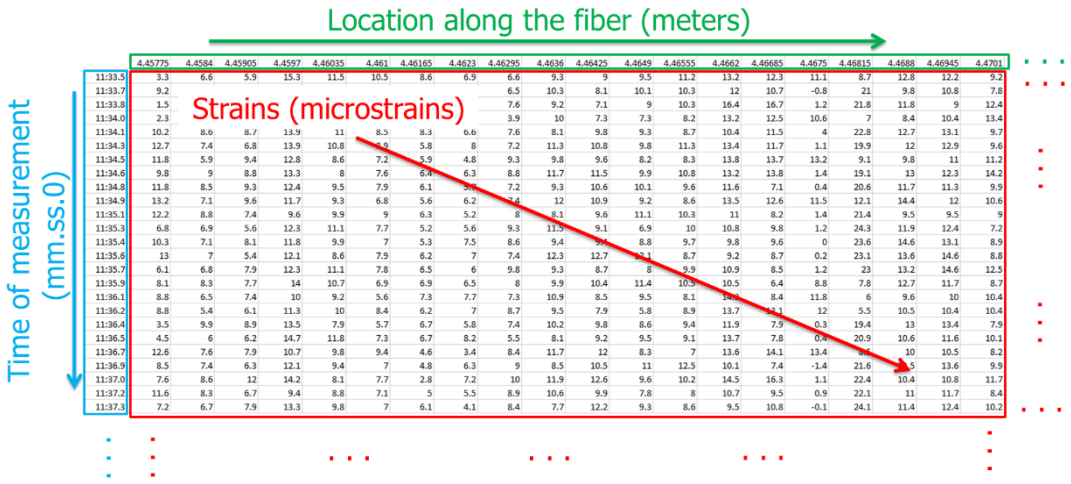

Figure 3.6 Example of a part of digital file of strain measurements produced by the interrogator unit for over a portion of the fiber at the start of the experiment.

The experimental data is plotted in strain waterfall plots where positive strain (or extension) is represented in red, and blue represents negative strain (or compression). The strain rate is also plotted. Due to the 6.25 Hz sampling rate of the equipment, the strain rate measurements were very noisy after the data processing. To overcome this, the strain-rate was down-sampled by averaging the strain change over 1-second intervals to reduce the noise in the data. Figure 3.7 to Figure 3.10 are synchronized plots of (a) strain in microstrains, (b) strain rate in microstrains/s and (c) pressure in psi, fracture radius in inches, rate in mL/min, and distance to the front in inches, over synchronized times. Figure 3.7 is an example of such plots that represent the results for the east fiber, which was intersected by the propagating fracture at 616 seconds. The convergence of the strain data (Figure 3.7a) matches the actual time that the fiber was intersected, based on the video of fracture propagation over time. The high spatial resolution of 0.65mm for the embedded fiber can capture exactly when the fracture intersects the fiber. A heart

shaped pattern of extension is observed in the strain waterfall plot and the heart shaped signature is centered around the fracture plane. The waterfall plots appear symmetrical above and below the fracture plane from the waterfall plot, but the strains are shown to be asymmetrical in Section 3.3.2. After the time of the fracture hit, there is a section of data nearest the fracture plane that is unable to be measured due to the limitations of the measurement device. After the time of the fracture intersection, there is an increasing shape of compression around the fracture plane, as shown with the expanding blue cone-shape. At 737 seconds, the data reverts to nearly zero strain around the fracture plane due to the relaxation measured in the fiber when the fracture propagated beyond the boundary of the cube. A comparable convergence pattern is observed in the strain rate waterfall plot (Figure 3.7b) leading up to the time of the fracture hit (dashed, vertical red line). The polarity of the strain and strain rate waterfall plots flip at the time of the fracture intersection as indicated the fracture transition from opening to closing. The strain rate plot reflects an increasing magnitude of extension pulses centered around the fracture plane as the fracture continues to propagate past the east fiber. In Figure 3.8c, the fracture radius growth (solid blue line) increases as the experiment progresses and nears 2-inches leading up to the time of the fracture hit. As a result of the fracture growth the distance to the fracture front (dotted blue lines) approaches zero. The fracture only intersected the east fiber, however the fracture was nearing north and south fibers before the experiment ended. The strain results for the north and south fibers are shown in Figure 3.9 and Figure 3.10, respectively. It is challenging to identify the converging

pattern; however, the concave signature is more easily observed in each strain-rate waterfall plot.

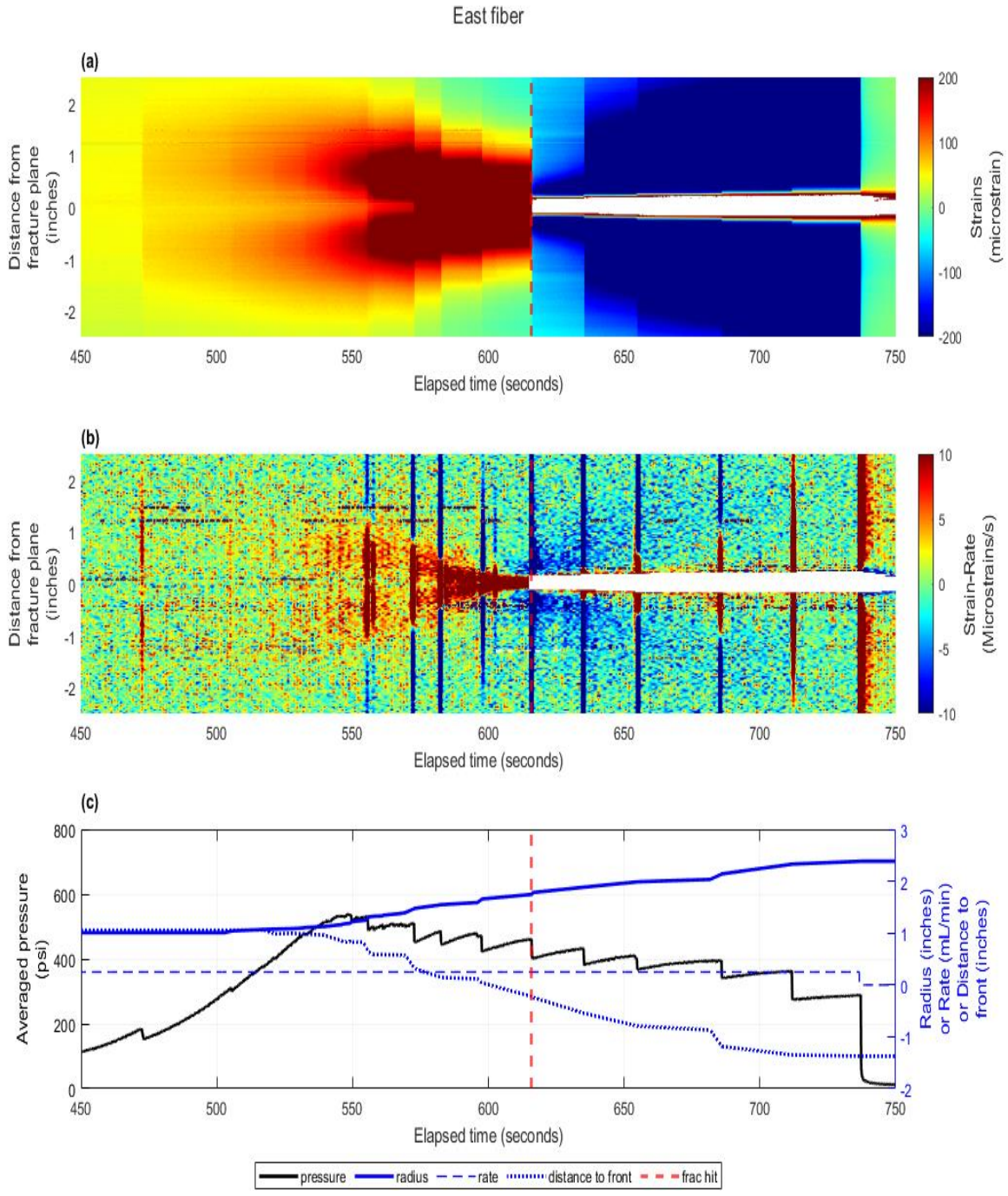

Figure 3.7 (a) Strain and (b) strain-rate waterfall plots for a propagating fracture intersecting an embedded fiber at 616 seconds. (c) The pressure and radius profiles are plotted below for reference.

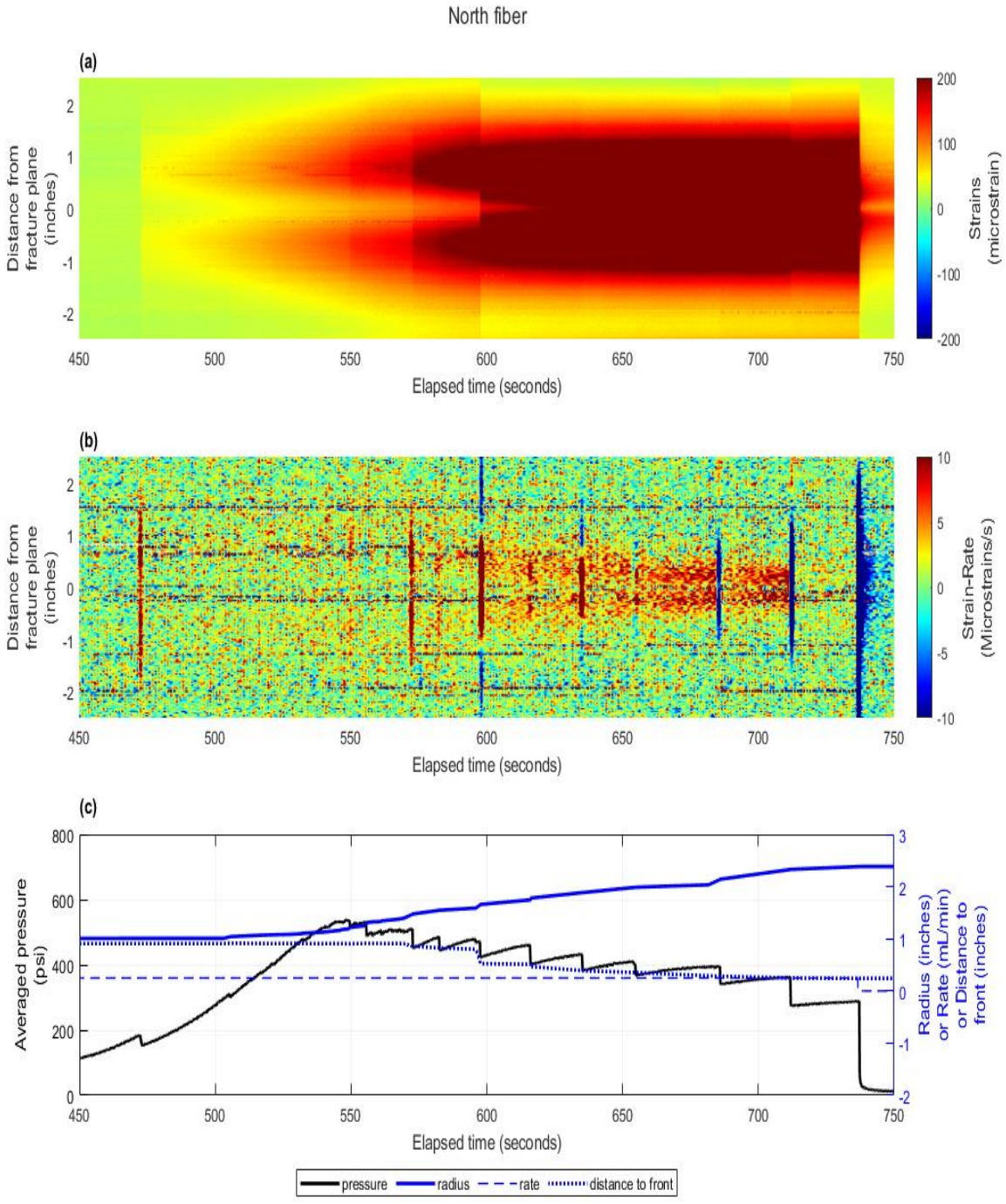

Figure 3.8 Strain (a) and strain-rate (b) waterfall plots of the north fiber which was not intersected by the propagating fracture. The pressure and radius profile are plotted below for reference (c).

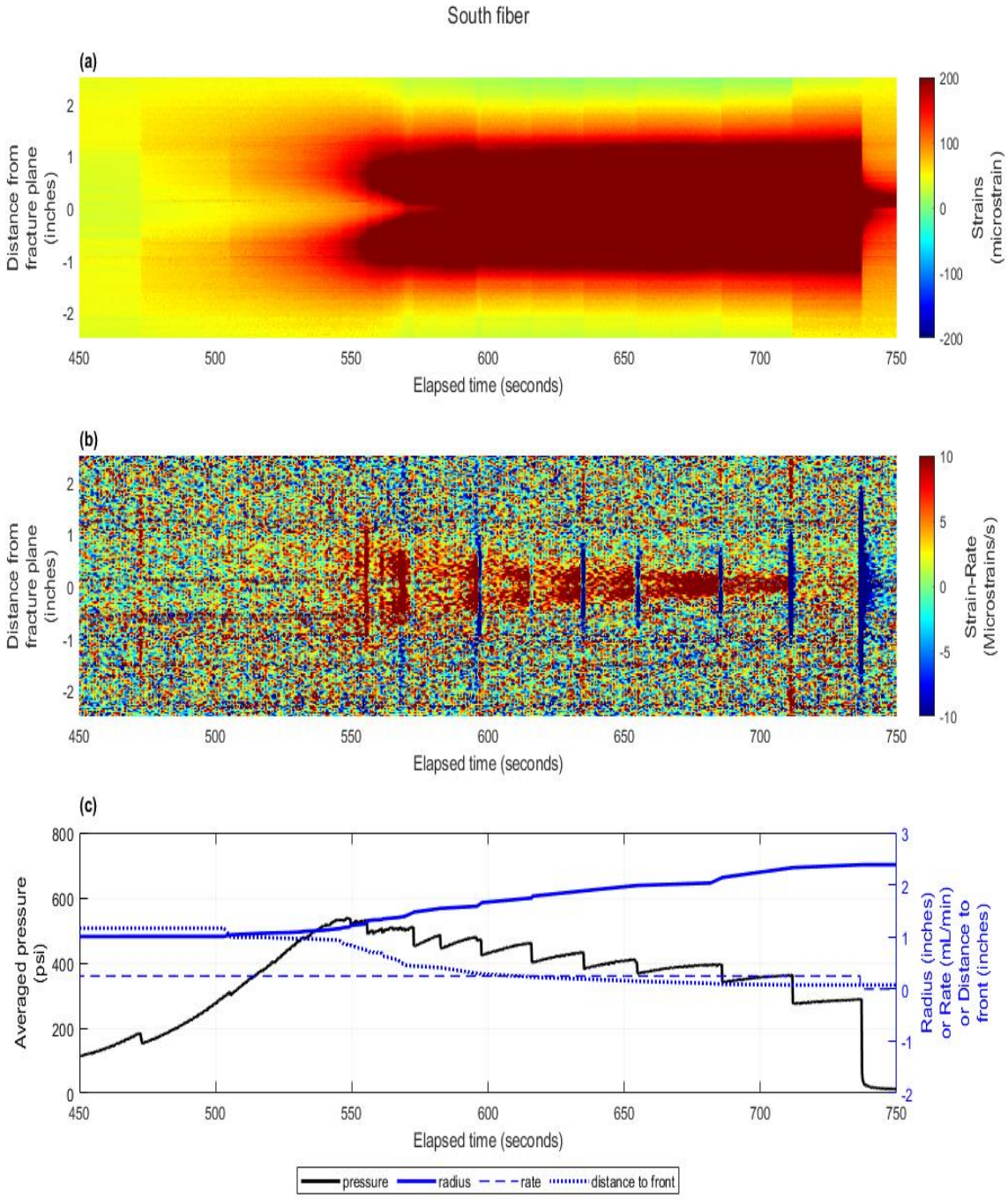

Figure 3.9 Strain (a) and strain-rate (b) waterfall plots of the south fiber which was not intersected by the propagating fracture. The pressure and radius profile are plotted below for reference (c).

The west fiber does not see as much extension across the studied length of fiber. This is due to the fracture not propagating in that direction. The waterfall plots for the west fiber are in Figure 3.10. Notice, that the distance to the fracture front (dotted blue line) maintains relatively constant after 550 seconds (Figure 3.10c).

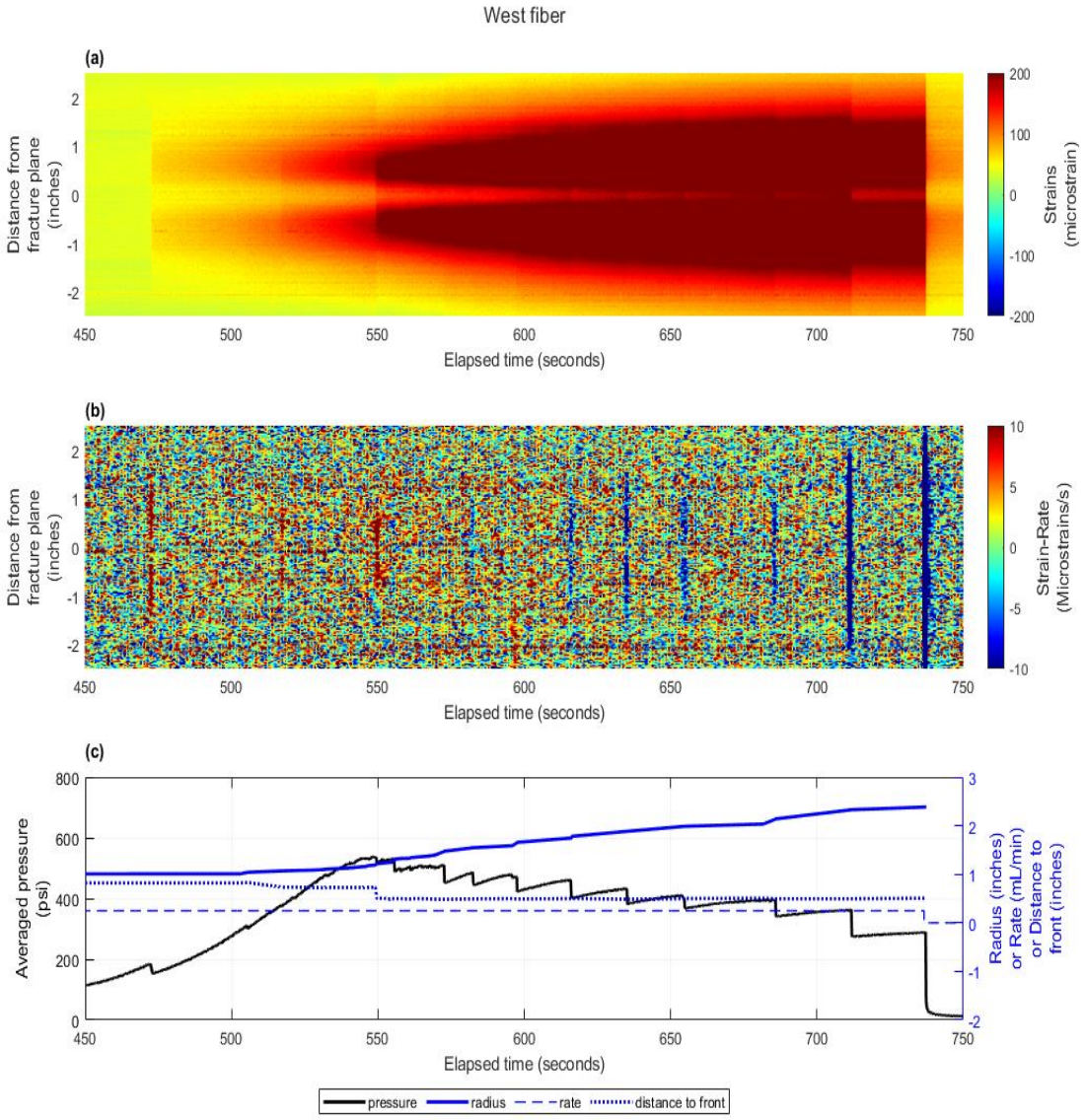

Figure 3.10 Strain (a) and strain-rate (b) waterfall plots of the west fiber which was not intersected by the propagating fracture. The pressure and radius profiles are plotted below for reference (c).

These measured strains from the waterfall plots can also be visualized at instantaneous times. Figure 3.11 and Figure 3.13 show the strain profile evolution for the south and east fiber, respectively. Figure 3.12 and Figure 3.14 show the strain profiles zoomed-in depicting the asymmetrical strain response over the fracture plane.

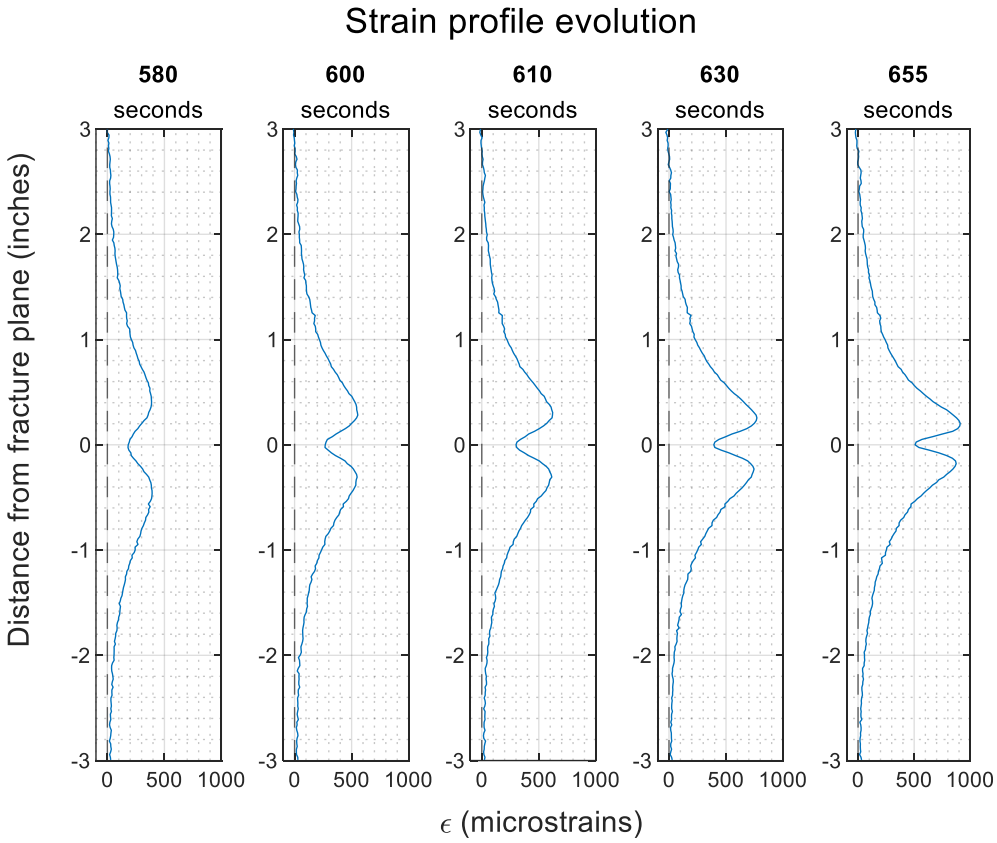

Figure 3.11 Strain profile evolution of the south fiber.

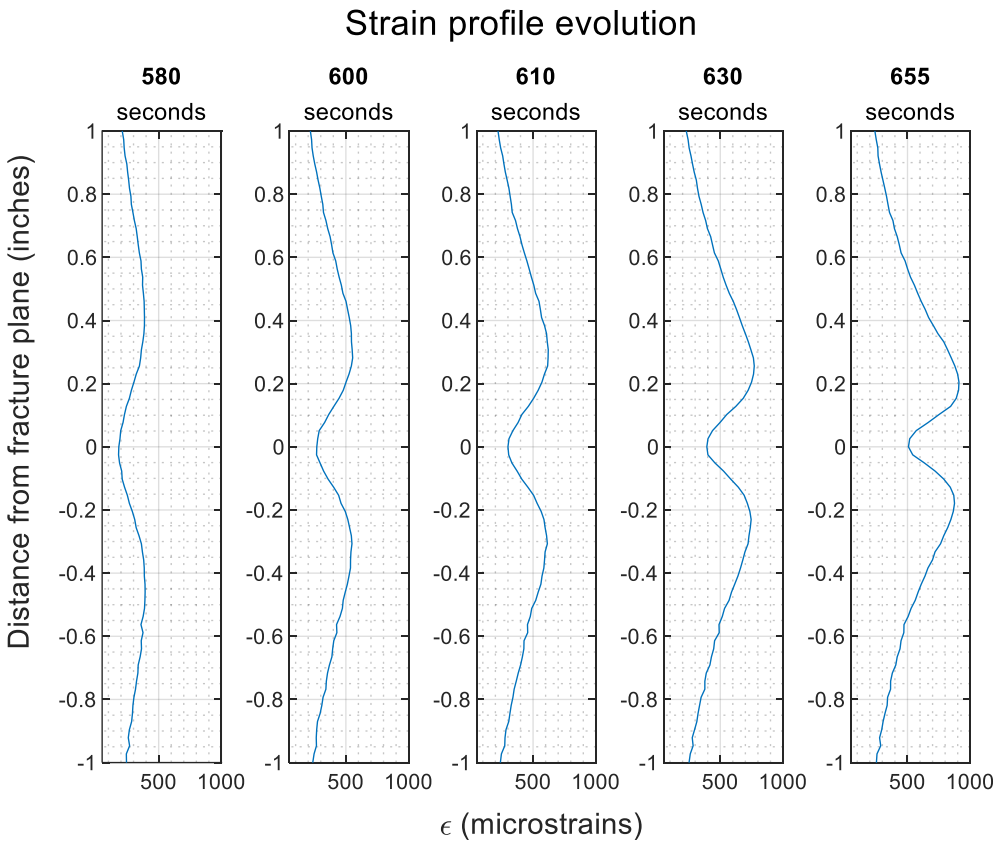

Figure 3.12 Zoomed-in strain profile evolution of the south fiber.

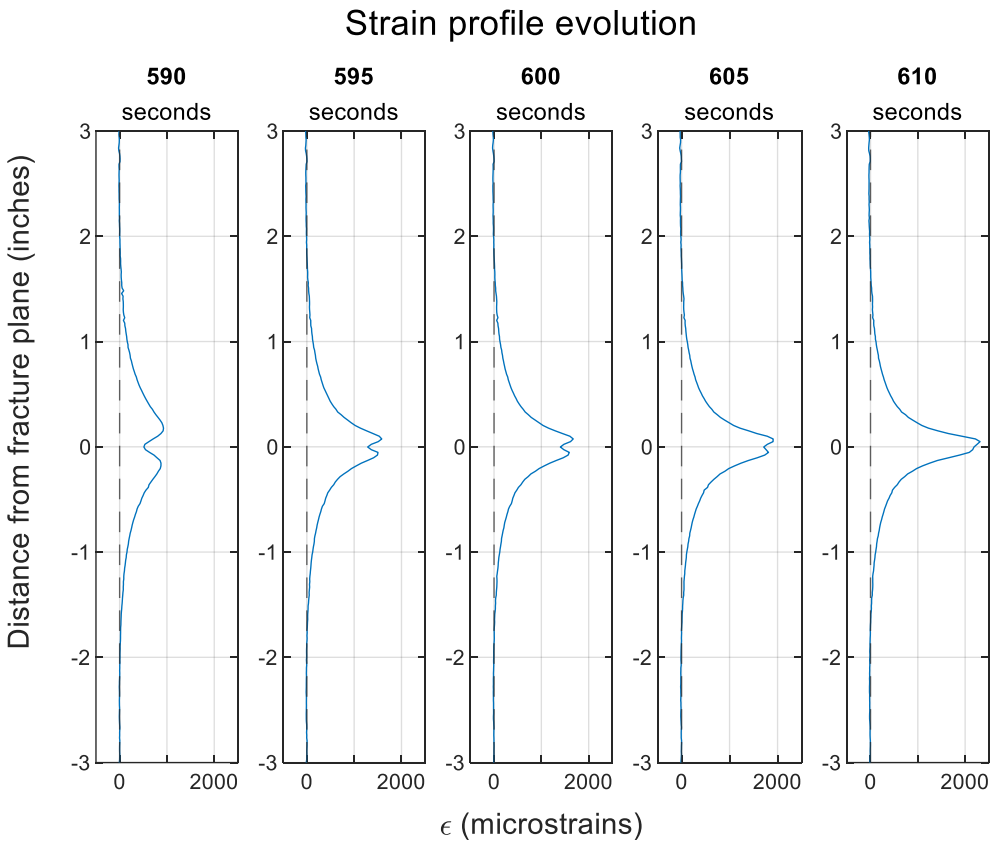

Figure 3.13 Strain profile evolution of the east fiber.

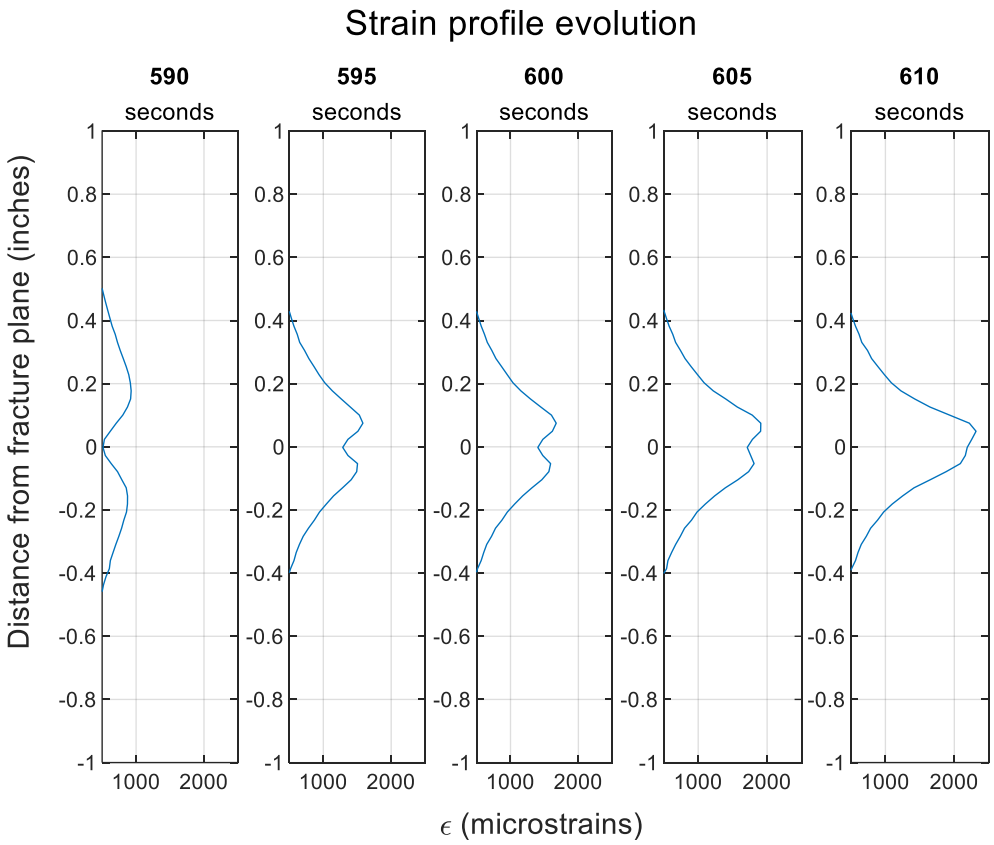

Figure 3.14 Zoomed-in strain profile evolution of the east fiber.

3.3. Measured Strains at Offset Fiber Optic Cables

The strains were measured by the ODiSI 6100 with the embedded distributed fiber sensors. It is important to recall that the east fiber was intersected by the fracture at 616 seconds, while the other three fibers were not intersected by the fracture. The injection stopped at 737 seconds when the fracture grew in the east direction beyond the boundary of the cube.

3.3.1. Measured Strains vs Time

The strains were recorded in 0.65 mm intervals along the fiber during the length of experiment. Figure 3.15 reveals the measured strain responses along the east fiber during the experiment at distinct locations on the fiber offset to the fracture plane. The offsets are plotted in 1/2” increments above and below the fracture plane. The distinct color lines represent different offsets from the fracture plane, while the purple line is the strain response at the fracture plane. The dotted red vertical line represents the time at which the fracture intersected the east fiber. As the fracture approached the fiber, an increasing amount of strain is observed at each point along the fiber with the largest strain response coming from the fiber location at the fracture plane. In fact, the strain at the fracture plane at the time of and after the fracture hit exceeded the measurement range of the interrogator unit. Since the measured strain response does not measure much strain variation between 0 to 450 seconds, Figure 3.16 shows a zoomed-in view from 450 to 750 seconds (the primary fracture growth time) and from -600 to +600 strains. This figure highlights how the intervals nearest the fracture plane exhibit the higher strain responses than those farther away from the plane of the fracture. Furthermore, the flip from extension (positive strain) to compression (negative strain) is observed at the time of the fracture hit at 616 seconds.

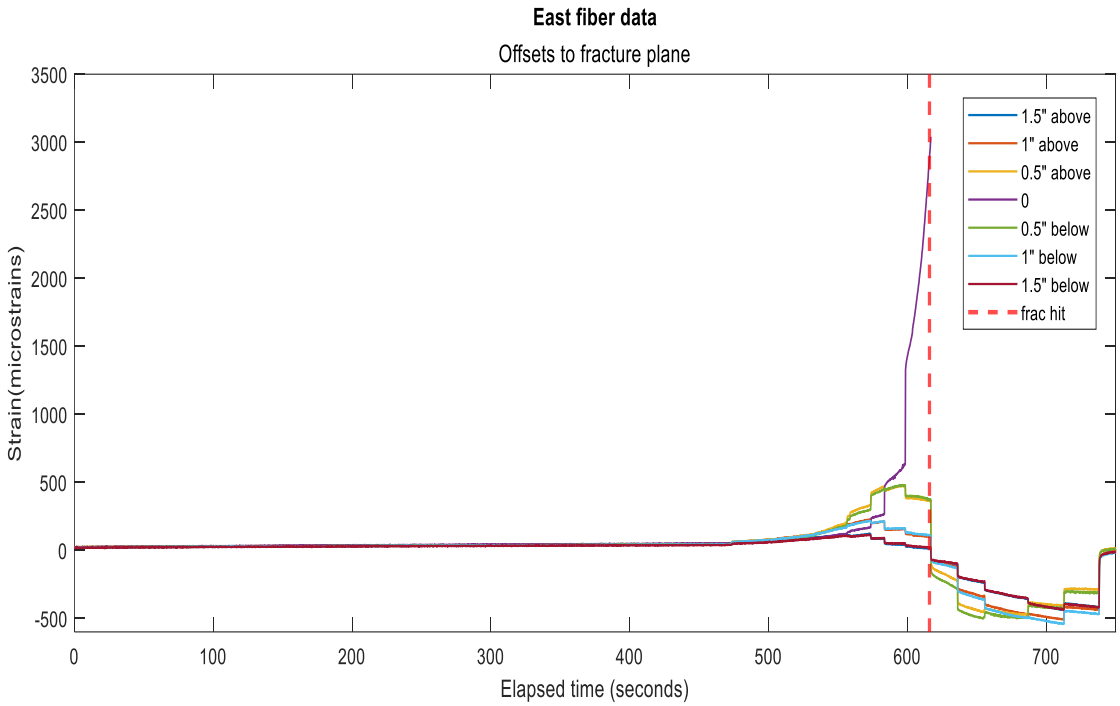

Figure 3.15 Measured strain response for the east fiber intersected by a propagating fracture.

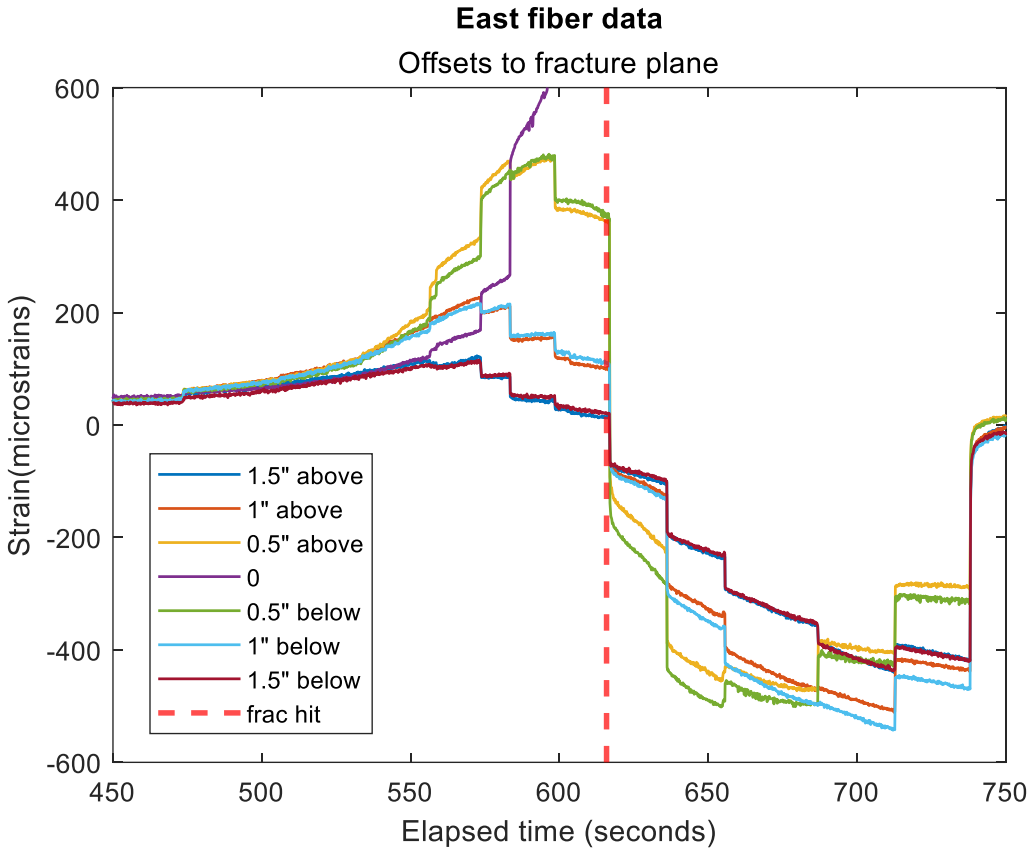

Figure 3.16 Zoomed in measured strain responses to propagating fracture.

Similar plots are shown in Figure 3.17 (north fiber), Figure 3.18 (south fiber), and Figure 3.19 (west fiber), where the fracture did not intersect the fiber. The fracture was nearing the north and south fibers by the end of the injection period, while the west fiber was not as approached. As a result, the magnitude of the strain responses felt by the west fiber are much less than the north and south. In the north fiber (Figure 3.17), the offset strains locations above the fracture plane experience more extension than the offset strain locations below the fracture plane. This difference is attributed to the combination of the

shear and normal stresses on the fracture plane. The rapid increases or decreases of the strain response align with times of fracture growth nearest the north fiber.

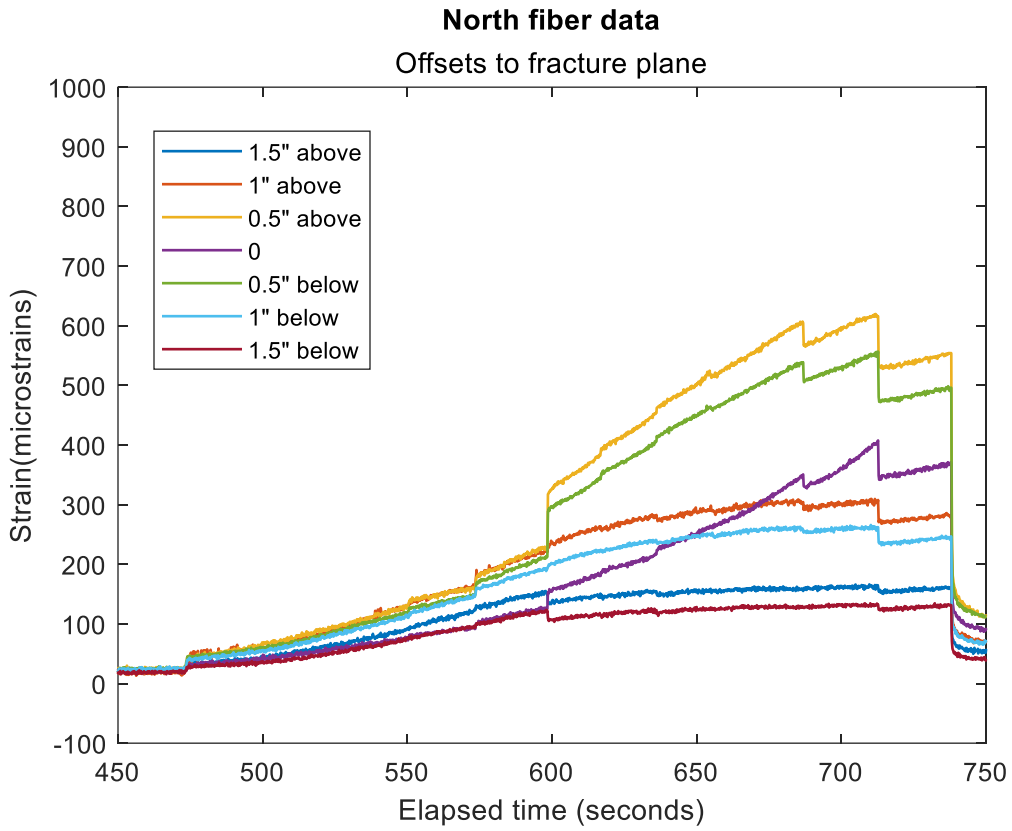

Figure 3.17 Measured strains at offset locations from the fracture plane during fracture growth for the north fiber not intersected by the fracture.

In the south fiber (Figure 3.18), the measured offset strains show different trends. At the 1-inch offsets (light blue for below fracture plane and orange for above fracture plane), the measured strains are higher for below the fracture plane. However, starting near 600 seconds the offset for the strain data at 0.5" away from the fracture plane is higher above the fracture plane than below the fracture plane. Additionally, the steep increase in the

strain at the fracture plane (purple line) is attributed to the fracture nearly reaching the south fiber before the experiment ended.

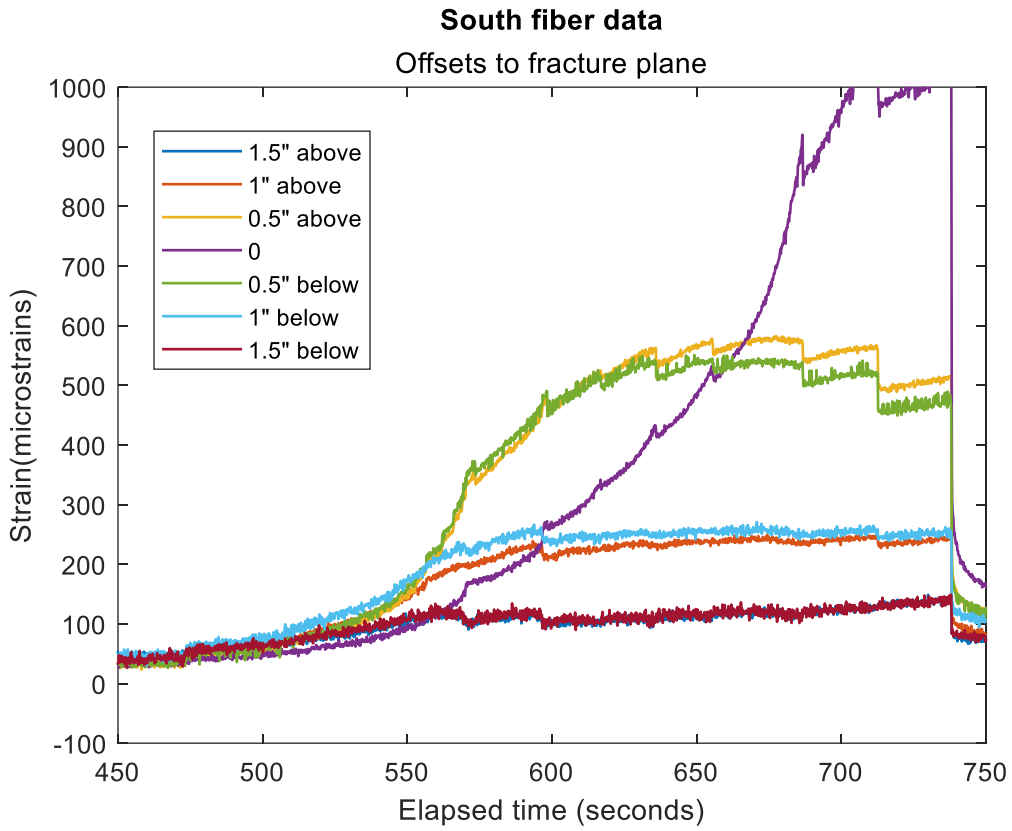

Figure 3.18 Measured strains at offset locations from the fracture plane during fracture growth for the south fiber not intersected by the fracture.

In the west fiber (Figure 3.19), the measured strains at offset locations on the fiber are all of less magnitude than the respective locations on the other fibers. This is caused by the lack of fracture propagation toward the west fiber. The offset strains nearest the fiber record higher strain responses than the offsets at farther locations from the fracture plane.

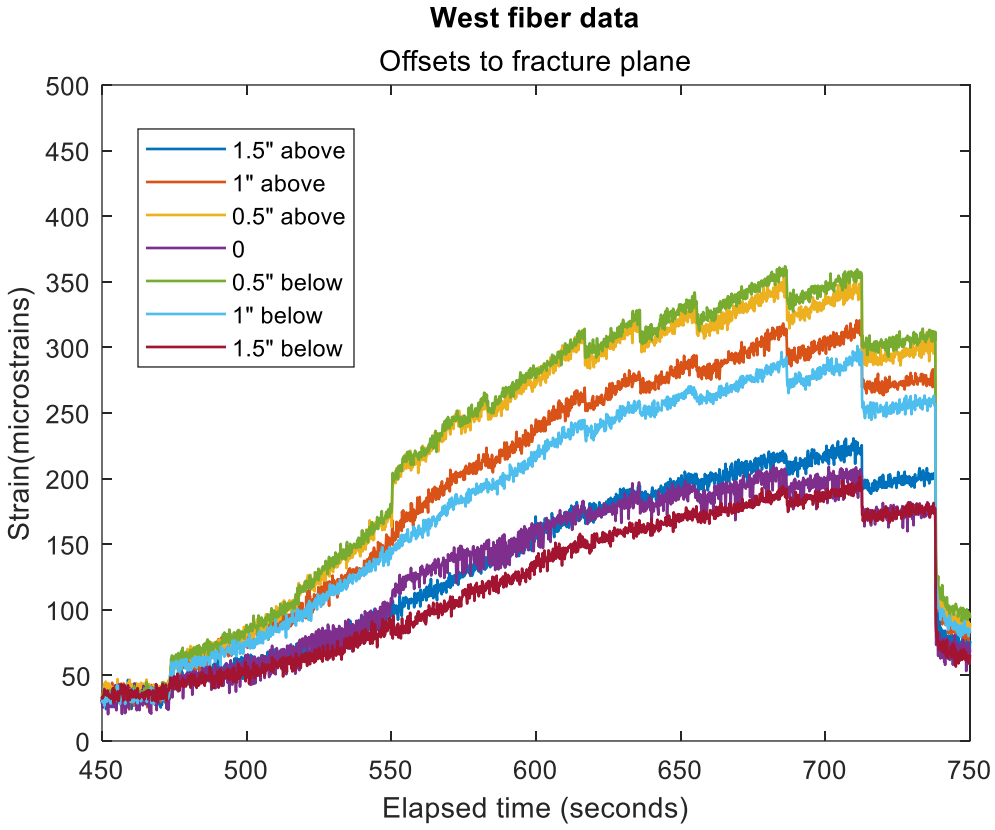

Figure 3.19 Measured strains at offset locations from the fracture plane during fracture growth for the west fiber not intersected by the fracture.

3.3.2. Cumulative Measured Strains vs Distance Normal to the Fracture Plane

Cumulative strains over the injection period at each gage is another way to analyze LF-DAS data. For each fiber, the strains from 0-737 seconds were summed at each depth to represent the total strains felt by each gage on the fiber over the entire injection period. The cumulative strains are shown in Figure 3.20, Figure 3.21, Figure 3.22, and Figure 3.23 for the north, south, east, and west fibers, respectively. The three fibers that were not hit by the fracture (north, south, and west) appear to have higher cumulative peak strains above the fracture plane compared to below the fracture plane. However, for the

east fiber (the one intercepted by the fracture), this is not the case. In order to diagnose the reason, the cumulative strains for the east fiber were further broken down into two time intervals: before the fracture hit (Figure 3.24) and after the fracture hit (Figure 3.25). It is observed that before the fracture hit the cumulative strains were higher above the fracture plane than below. This data suggests that as a fracture with shear and normal stresses is approaching a fiber optic cable, the strain responses on either side of the fracture will not be equivalent due to the introduction of the shear stress on the fracture plane.

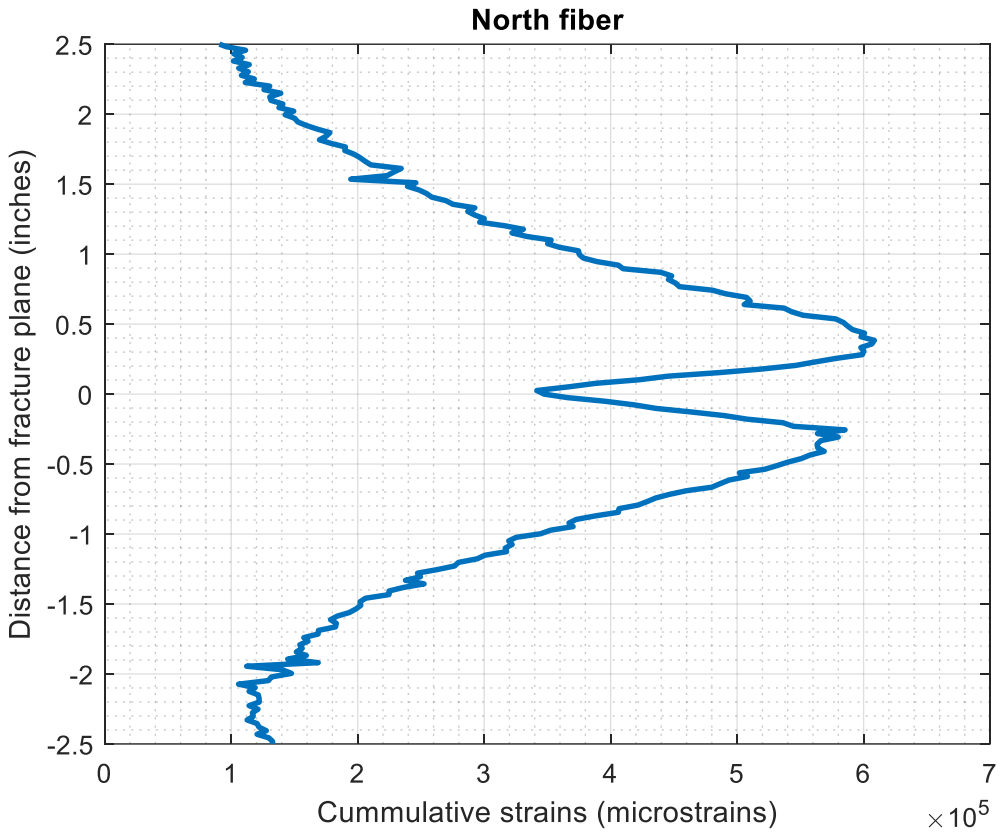

Figure 3.20 Cumulative strains of the north fiber from start to end of injection (0 to 737 seconds).

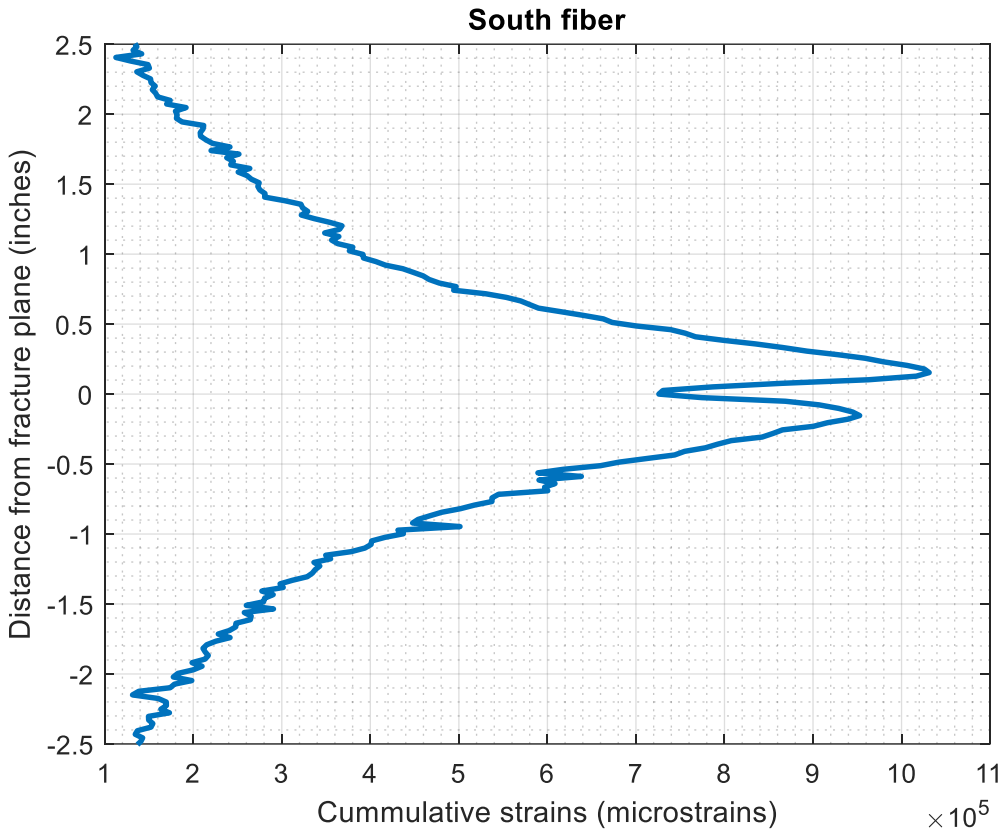

Figure 3.21 Cumulative strains of the south fiber from start to end of injection (0 to 737 seconds).

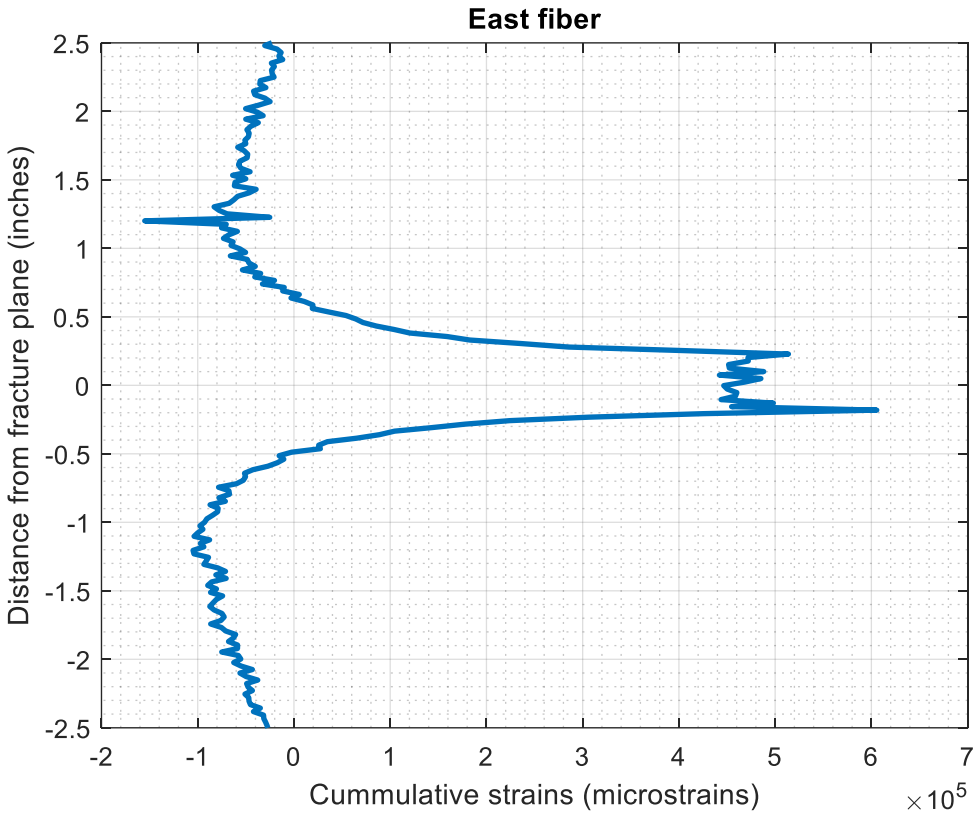

Figure 3.22 Cumulative strains of the east fiber from start to end of injection (0 to 737 seconds).

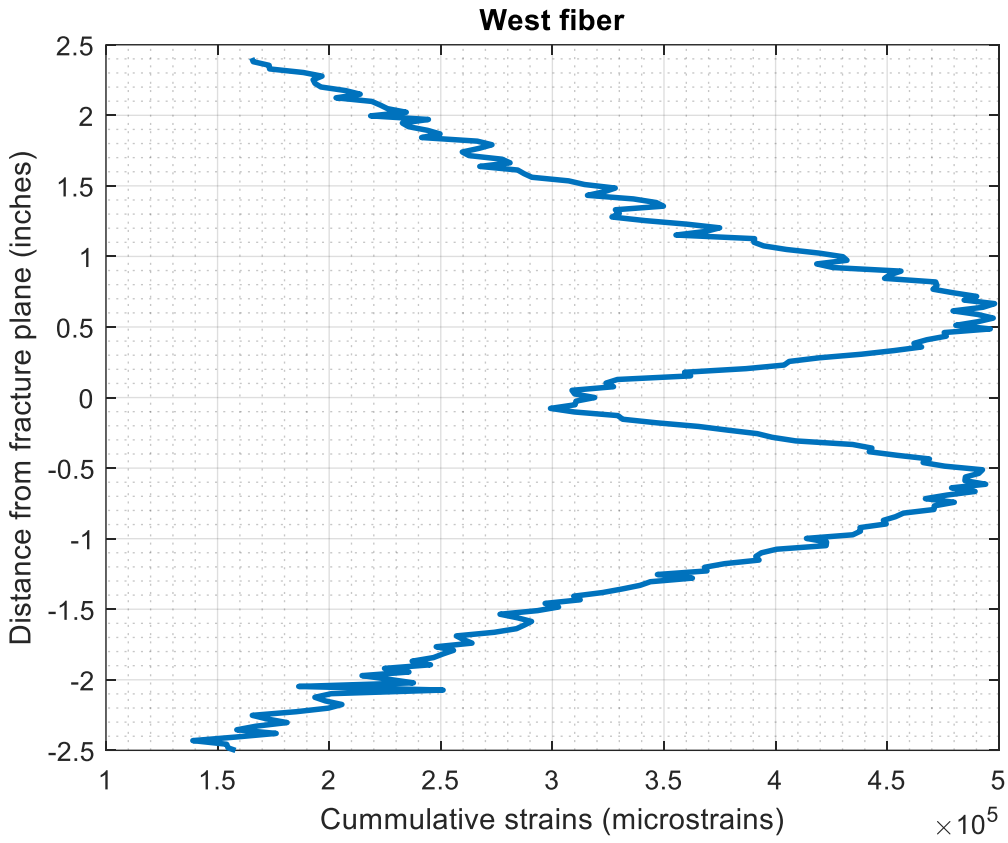

Figure 3.23 Cumulative strains of the west fiber from start to end of injection (0 to 737 seconds).

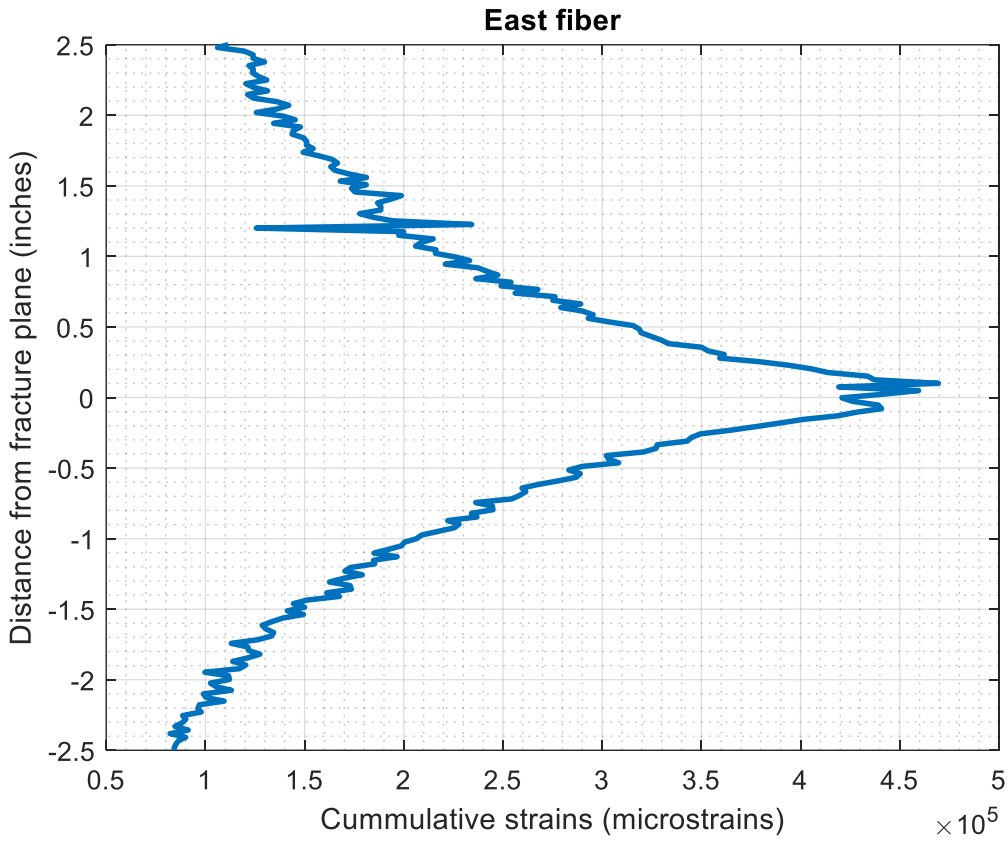

Figure 3.24 Cumulative strains of the east fiber up to fracture hit time (0 to 616 seconds).

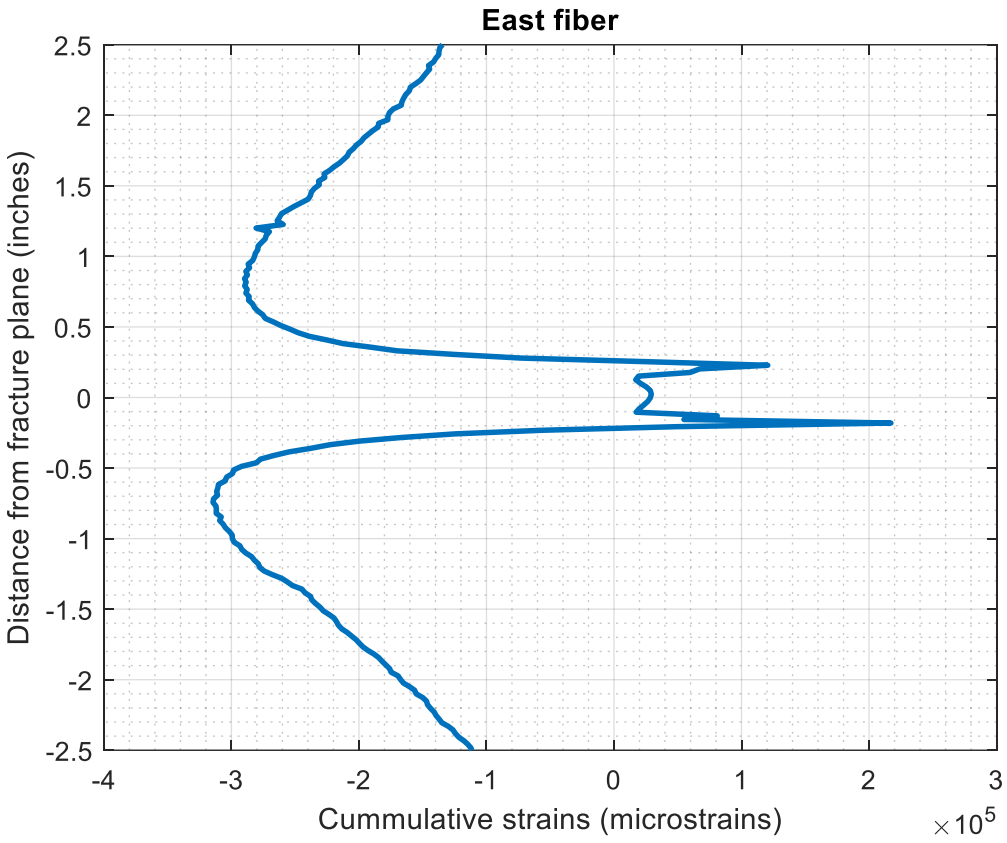

Figure 3.25 Cumulative strains of the east fiber from after fracture hit time to end of injection (616 to 737 seconds).

For direct comparison of the cumulative strains above and below the fracture plane, bar charts were created. The cumulative strains during the experiment over ¼" intervals along the fracture plane are summed around the fracture plane. Figure 3.26, Figure 3.27, Figure 3.28, and Figure 3.29 represent the comparisons between below the fracture plane (blue) and above the fracture plane (orange) for the north, south, east, and west fibers, respectively. The bar charts suggest that above the fracture plane experiences more extension than below the fracture plane at the same offset. This reflects the impact of the shear stress in addition to the normal stress that exists along the fracture plane, since

previous work alluded to a symmetrical response over the fracture plane when a purely normal stress was present on the fracture plane (Leggett, 2022).

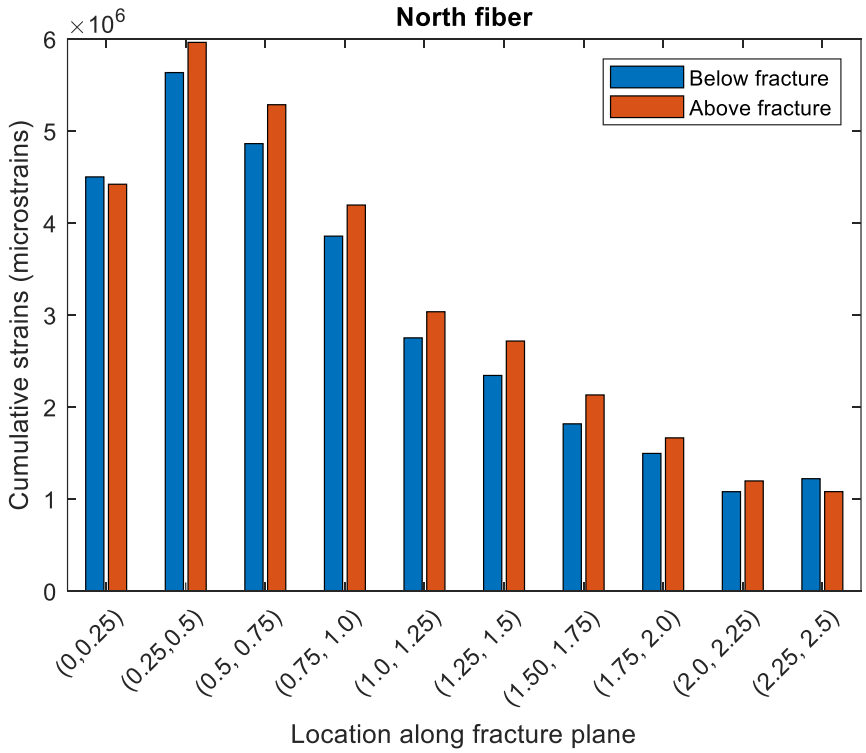

Figure 3.26 Above and below strains for the north fiber in one-fourth-inch increments around the fracture plane from 0 to 737 seconds.

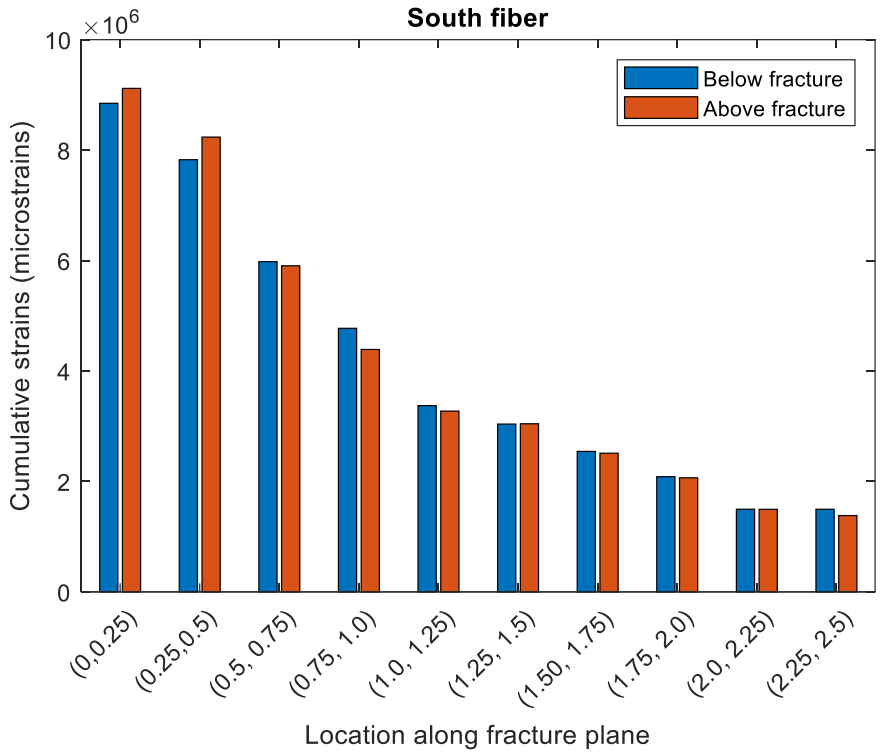

Figure 3.27 Above and below strains for the south fiber in one-fourth-inch increments around the fracture plane from 0 to 737 seconds.

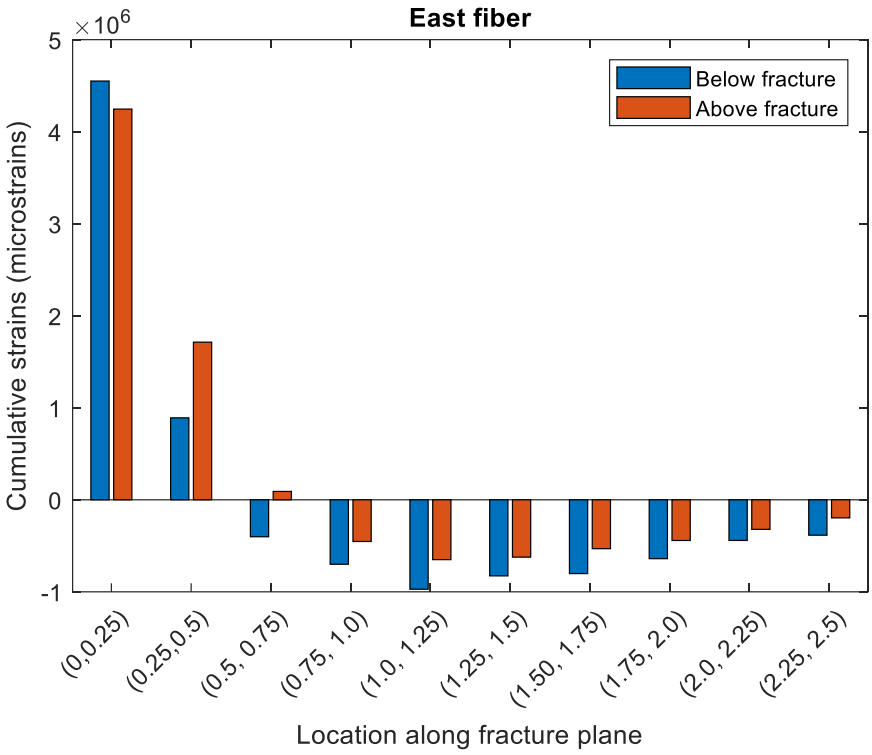

Figure 3.28 Above and below strains for the east fiber in one-fourth-inch increments around the fracture plane from 0 to 737 seconds.

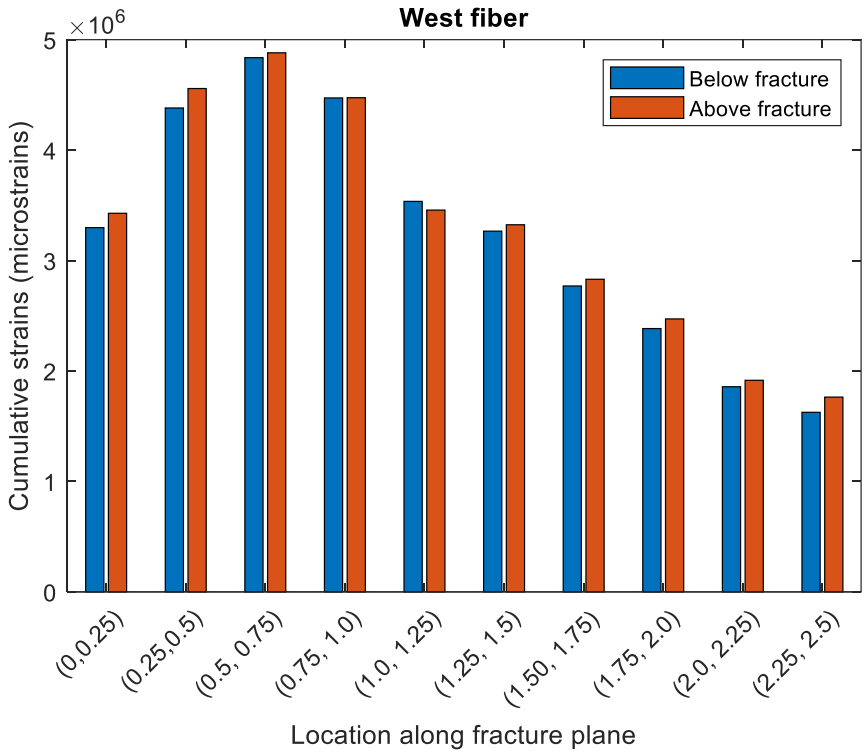

Figure 3.29 Above and below strains for the west fiber in one-fourth-inch increments around the fracture plane from 0 to 737 seconds.

The fracture hit fiber is again broken down into two separate time segments: before the fracture hit (Figure 3.30) and after the fracture hit (Figure 3.31).

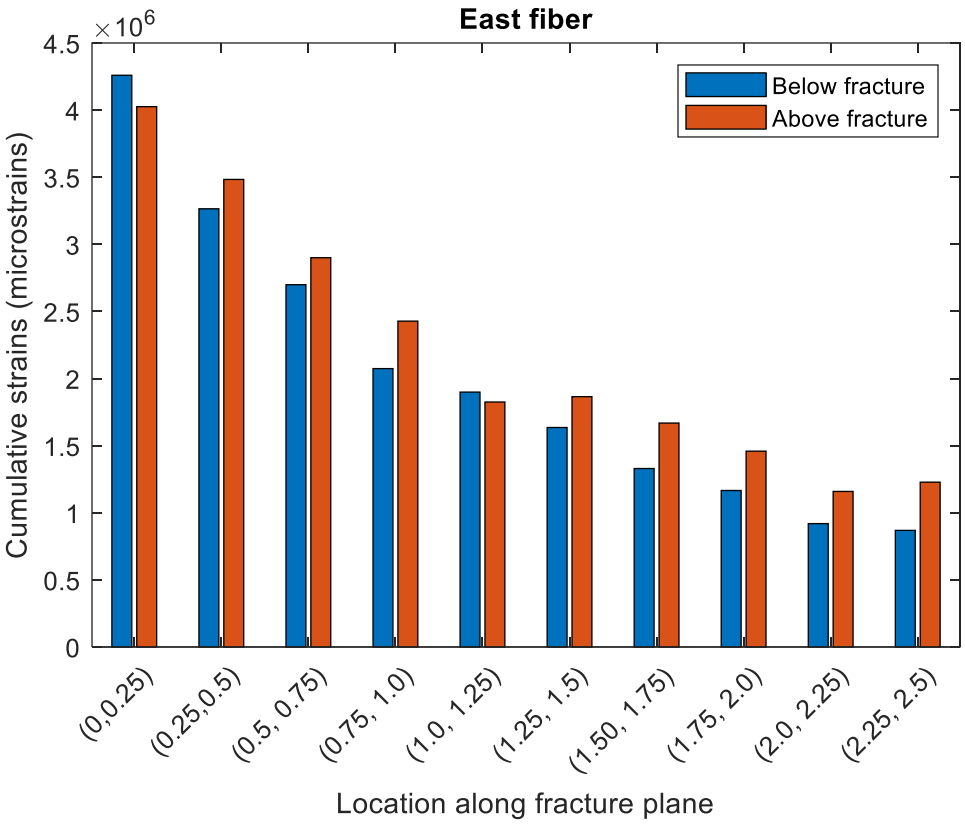

Figure 3.30 Above and below strains for the east fiber in one-fourth-inch increments around the fracture plane from 0 to 616 seconds.

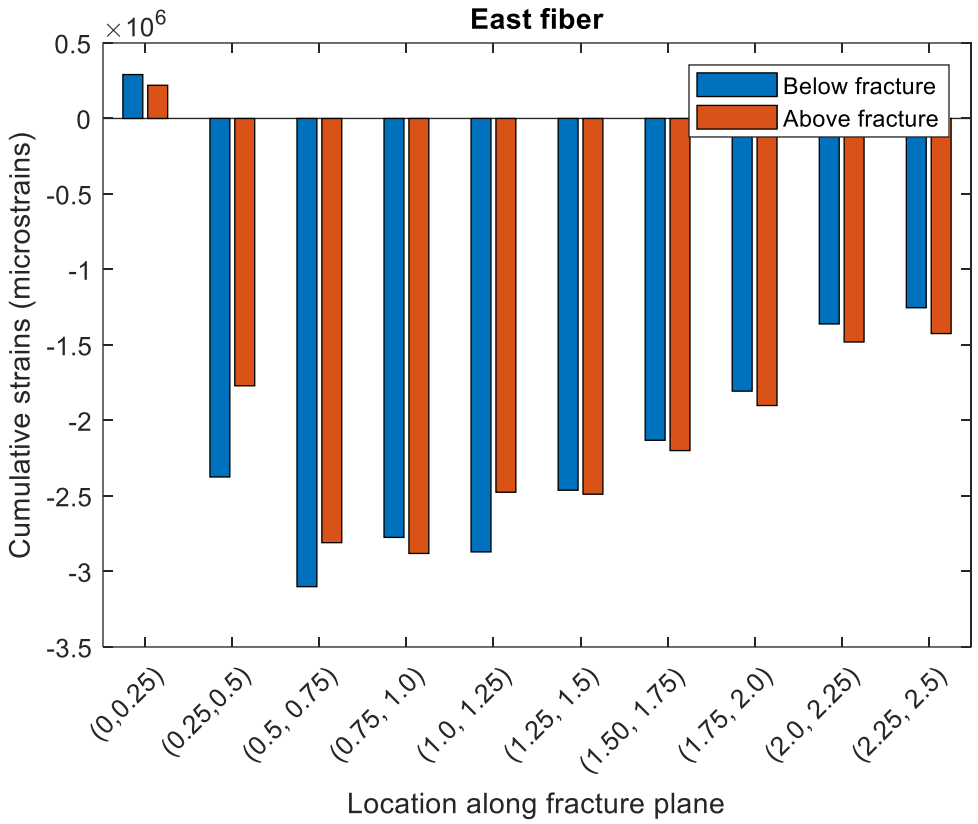

Figure 3.31 Above and below strains for the east fiber in one-fourth-inch increments around the fracture plane from 616 to 737 seconds.

3.4. Application of Zero-Strain Location Method

The zero-strain location method (Leggett et al., 2022) is applied to the zero-strain responses for the frac hit fiber. A series of example calculations are also presented.

3.4.1. Application of Zero-Strain Location Method to Experimental Results

Figure 3.32 is the strain waterfall plot for the east fiber and the black crosses represent the locations that the strain nearest to 0 strains. These are considered as the zero-strain location points. As indicated in the color scale bar to the right, these zero-strain locations are represented by the green color in the waterfall map. The depths at the respective

zero-strain locations are utilized in the zero-strain location method as inputs to the model for estimating the effective fracture radius and distance to the fracture front.

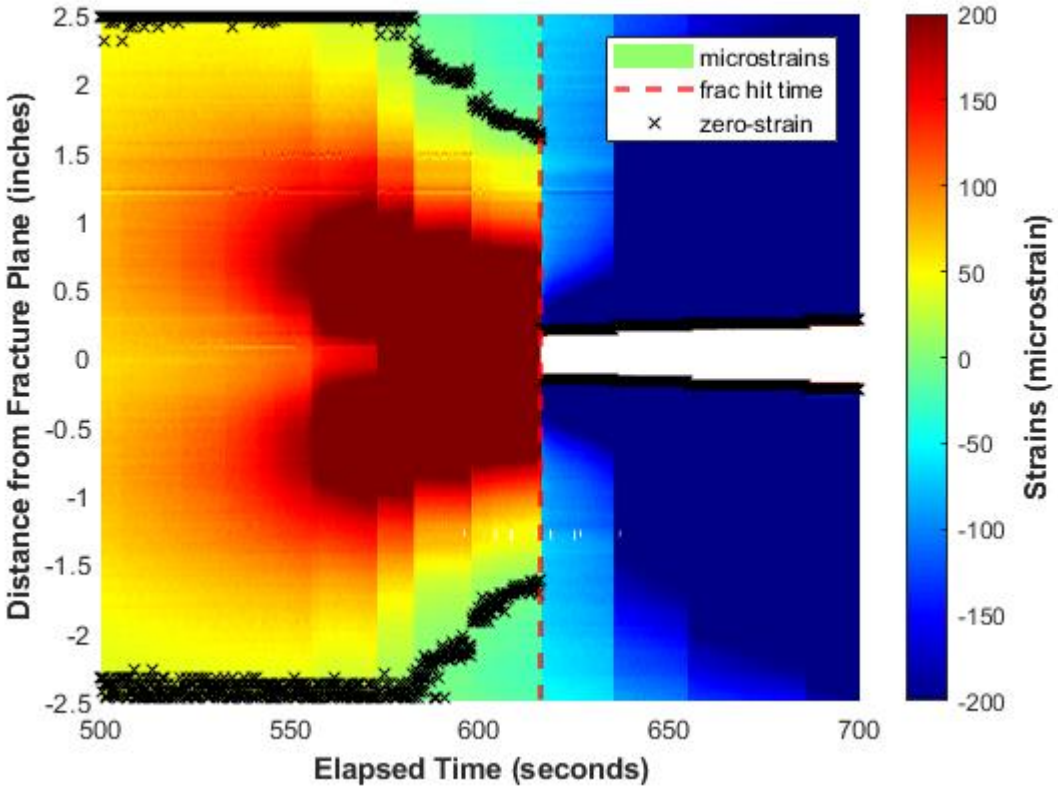

Figure 3.32 Strain waterfall with marked zero-strain locations (black x's) and the frac hit time (vertical red dashed line).

The zero-strain location method is applied for both the zero strains above the fracture plane and below the fracture plane. Figure 3.33 shows the results from the zero-strain location. The crosses represent the effective radii (Figure 3.33a) and distance to the front (Figure 3.33b) results against the experimentally measured effective radii and distance to the front, respectively. The blue crosses are the model results from using the zero strain locations above the fracture plane. The red crosses are the model results using the zero

strain locations below the fracture plane. The application of the zero-strain location method shows agreement with the measured results (in black line) for the zero-strain locations available prior to the fracture hit. The results between 580 seconds and 595 seconds suggest that the zero-strains from above the fracture plane overestimate the fracture effective fracture radius while underestimating the distance to the fracture front. Additionally, the model results from below the fracture plane in this section underestimate the effective radius while overestimating the distance to the fracture front. However, as the fracture propagates from 595 seconds to the time of fracture intersection at 616 seconds the model increases in accuracy for both the effective radius and distance to the fracture front.

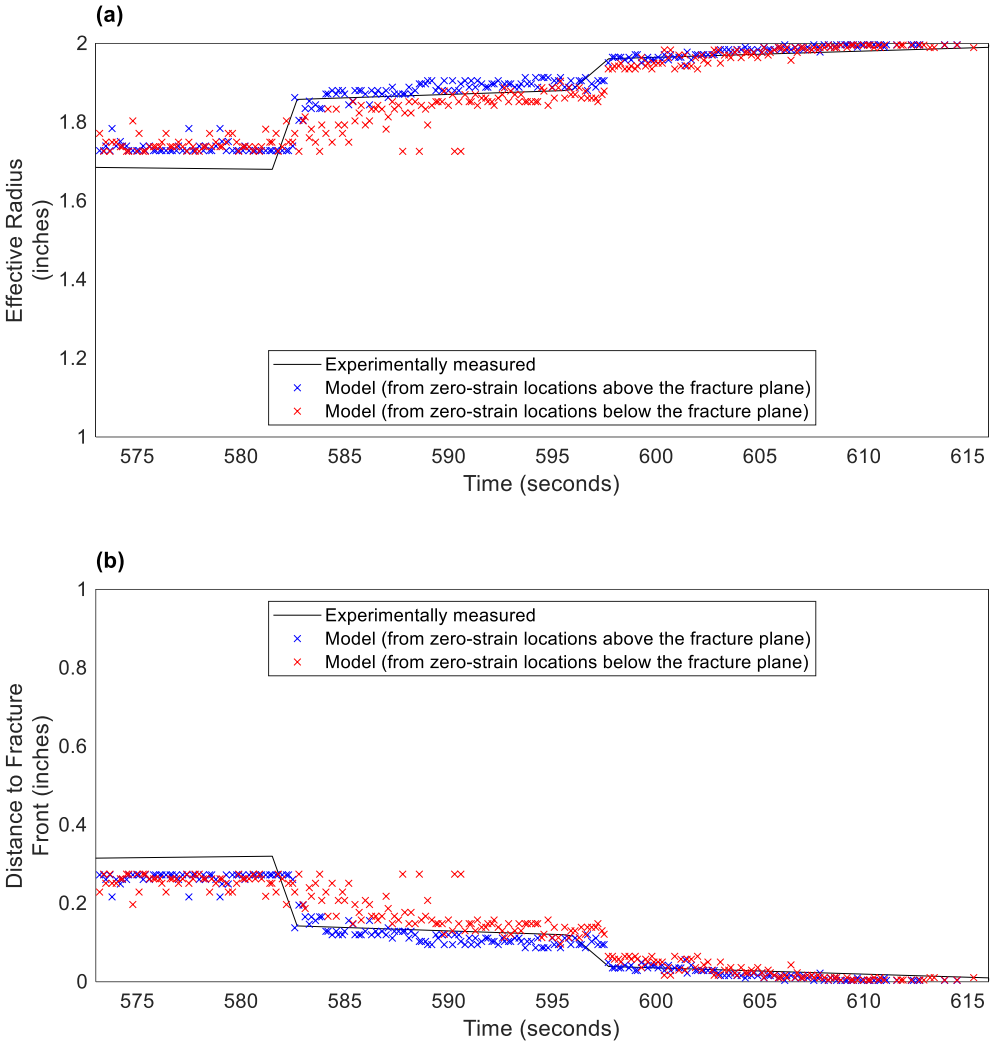

Figure 3.33 (a) Effective radius and (b) distance to fracture front versus time of the experimentally measured and modeled results from the zero-strain location method (using zero-strains above fracture plane in blue and using below zero-strain above fracture in red).

3.4.2. Example Illustrating the Zero-strain Location Method

A sample calculation of this method is performed for a series of the zero strain locations from the experimental data. First, the Poisson's ratio, distance of the fracture hit, and the radial offset distance of the fiber are assumed as outlined in Table 3.1. Then, the

zero-strain locations and respective times are selected from the strain-waterfall plot. A series of the zero-strain locations are selected for this example in

Table 3.2. Next, Equations 2.3 **to** 2.5**, as presented in Section 2.1, are used to calculate the dimensionless zero-strain locations, the constants (a, b, and c), dimensionless fracture radius, and the distance to the fracture front outlined in**

Table 3.3. The plotted results of the nearest distance to the fracture front are presented in Figure 3.34

Table 3.1. Example calculation parameters.

Depth of fracture hit	D_{hit}	0.0	inches
Radial offset	r	2	inches
Poisson's ratio	v	0.35	unitless

Table 3.2 Example calculation zero-strain locations.

Time (seconds)	z_0 **locations**
585	2.122
590	2.096
595	2.020
600	1.815
605	1.764
610	1.687
615	1.661

Table 3.3 Example calculations results of distance to the fracture front.

Time (seconds)	z_{0D}	a	b	c	R_D	d_f
585	1.06	-0.52	0.03	1.17	0.47	1.05
590	1.05	-0.52	0.03	1.17	0.50	1.00
595	1.01	-0.52	0.03	1.17	0.57	0.86
600	0.91	-1.14	0.74	0.95	0.71	0.58
605	0.88	-1.14	0.74	0.95	0.74	0.52

Table 3.3 Continued

610	0.84	-1.14	0.74	0.95	0.78	0.44
615	0.83	-1.14	0.74	0.95	0.79	0.42

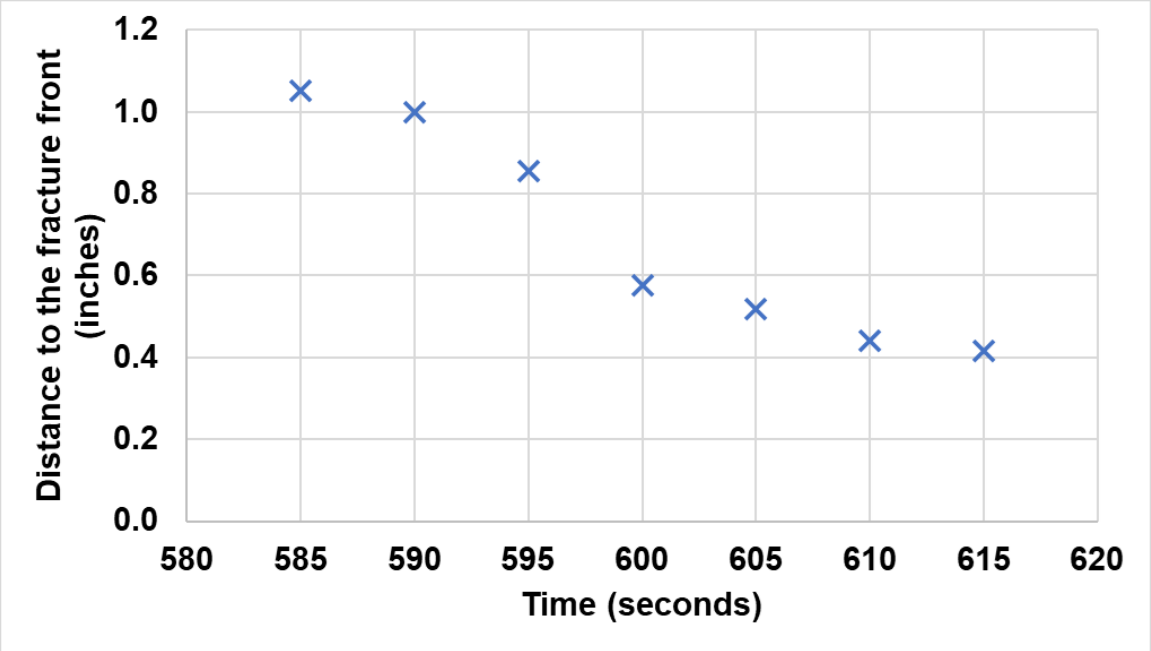

Figure 3.34. Example calculation result for the nearest distance to from the fiber to the fracture front.

3.5. Finite Element Modeling

ABAQUS, a Simulia software (Dassault Systems), was used to create a finite element model of the experiment conditions. To simulate the experiment, the angled fracture with applied load was reconfigured to an orthogonal fracture based on the theory of elasticity (Equation 3.1).

$$\widetilde{\boldsymbol{\sigma}}' = \widetilde{\boldsymbol{Q}}^{\boldsymbol{T}} \cdot \widetilde{\boldsymbol{\sigma}} \cdot \widetilde{\boldsymbol{Q}} \tag{3.1}$$

where rotation tensor, $\widetilde{\boldsymbol{Q}}$, is presented in Equation 3.2,

$$\widetilde{\boldsymbol{Q}} = \begin{bmatrix} 1 & 0 & 0 \\ 0 & cos\alpha & sin\alpha \\ 0 & -sin\alpha & cos\alpha \end{bmatrix} \tag{3.2}$$

and the stress tensor, $\widetilde{\boldsymbol{\sigma}}$, is presented in Equation 3.3,

$$\widetilde{\boldsymbol{\sigma}} = \begin{bmatrix} \sigma_{xx} & \tau_{xy} & \tau_{xz} \\ \tau_{yx} & \sigma_{yy} & \tau_{yz} \\ \tau_{zx} & \tau_{zy} & \sigma_{zz} \end{bmatrix} = \begin{bmatrix} 0 & 0 & 0 \\ 0 & \sigma_{yy} & 0 \\ 0 & 0 & 0 \end{bmatrix} \tag{3.3}$$

As a result, we get rotated stress tensor, $\widetilde{\boldsymbol{\sigma}}'$, as in Equation 3.4

$$\widetilde{\boldsymbol{\sigma}}' = \begin{bmatrix} 0 & 0 & 0 \\ 0 & \sigma_{yy}\cos^2\alpha & \sigma_{yy}cos\alpha sin\alpha \\ 0 & \sigma_{yy}cos\alpha sin\alpha & \sigma_{yy}\sin^2\alpha \end{bmatrix} \tag{3.4}$$

Given the experiment was conducted at $\alpha = 5.12°$ and $\sigma_{yy} = 250$ psi where α is the angle of the fracture plane offset to the vertical and σ_{yy} is the applied load on the surface of the sample. Figure 3.35 illustrates the set-up during the construction of the cube if the load were applied at the time.

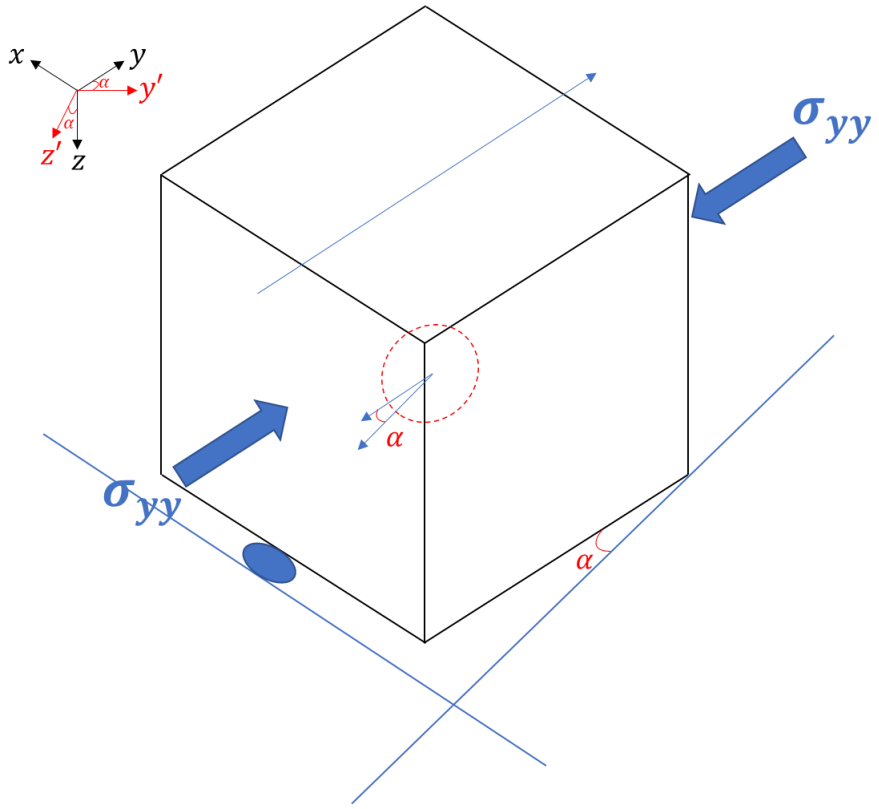

Figure 3.35 Schematic of the sample construction with respect to the angled fracture and the applied load.

The following are the stress components applied to the fracture:

$$\boldsymbol{\sigma_{y'y'}} = \sigma_{yy} \cos^2 \alpha \, 250 \, cos^2(5.12) = \mathbf{248.01} \, \boldsymbol{psi} \tag{3.5}$$

$$\boldsymbol{\sigma_{z'z'}} = \sigma_{yy} \sin^2 \alpha \, 250 \, sin^2(5.12) = \mathbf{1.99} \, \boldsymbol{psi} \tag{3.6}$$

$$\boldsymbol{\tau_{y'z'}} = \boldsymbol{\tau_{z'y'}} = \sigma_{yy} \cos(\alpha) \sin(\alpha) 250 \, cos(5.12) \, sin(5.12) = \mathbf{22.22} \, \boldsymbol{psi} \tag{3.7}$$

$$\boldsymbol{\sigma_{x'x'}} = \boldsymbol{\tau_{x'y'}} = \boldsymbol{\tau_{x'z'}} = \boldsymbol{\tau_{y'x'}} = \boldsymbol{\tau_{z'x'}} = \mathbf{0} \, \boldsymbol{psi} \tag{3.8}$$

The stress components from Equations **3.5** to **3.8** are used in the finite element model as shown in Figure 3.36.

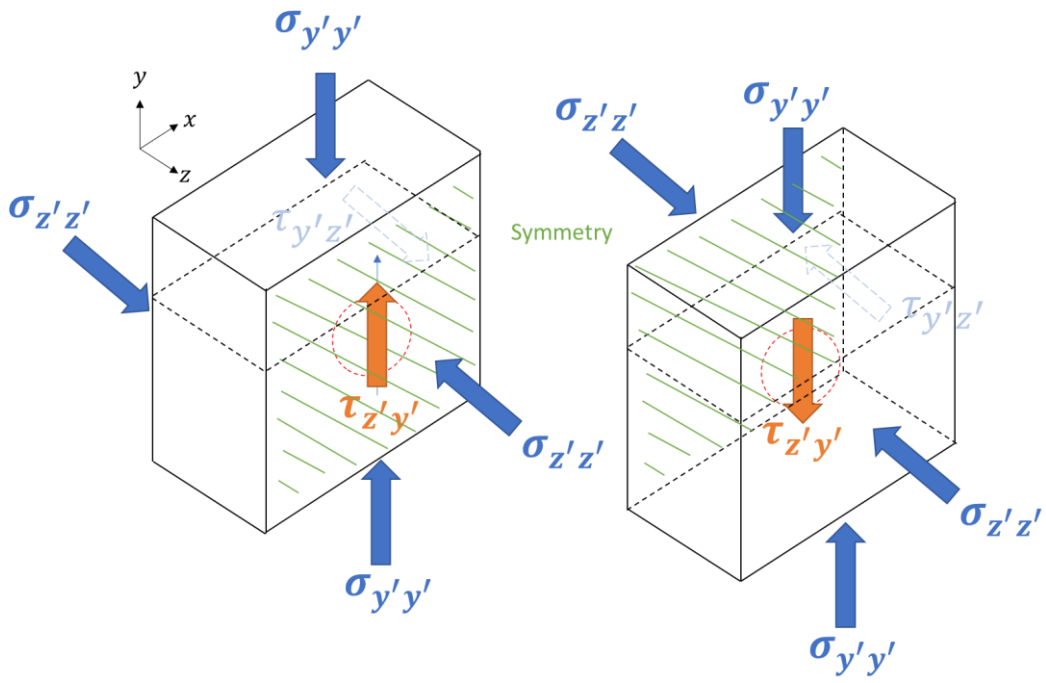

Figure 3.36 Schematic of the finite element model with the applied forces.

A screenshot of the finite element model with the loading and boundary conditions is presented in Figure 3.37. The modeled displacement is shown in Figure 3.38 for a 500-psi fracture pressure. The coloring represents the magnitude of displacement, where red is high displacement compared to the blue which is near zero. Figure 3.39 provides the modeled strain response in orange compared to the experimental result in blue. The agreement between the modeled and experimental data suggests that the experiment did induce a shear and normal stress on the fracture plane. Furthermore, the embedded fiber is representative of the modeled case.

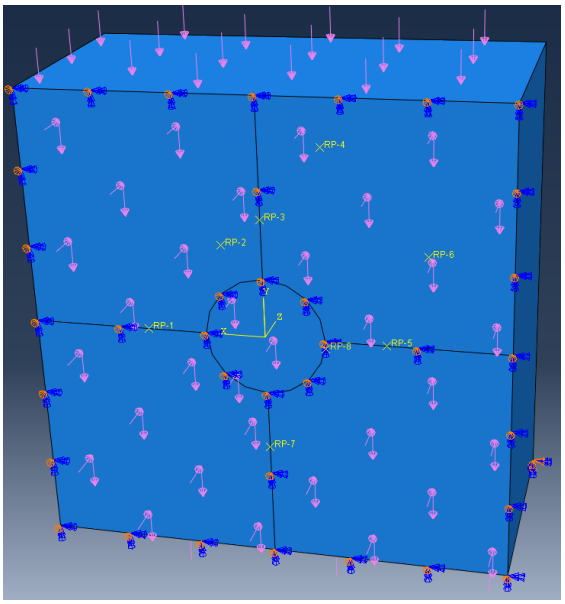

Figure 3.37 Finite element model in ABAQUS of half of the cube.

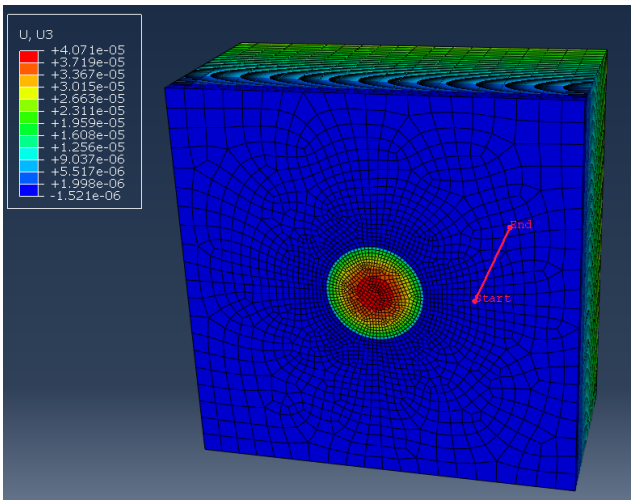

Figure 3.38 Displacement in the z-direction for the finite element model. The red line represents the location of the fiber where the strain is modeled.

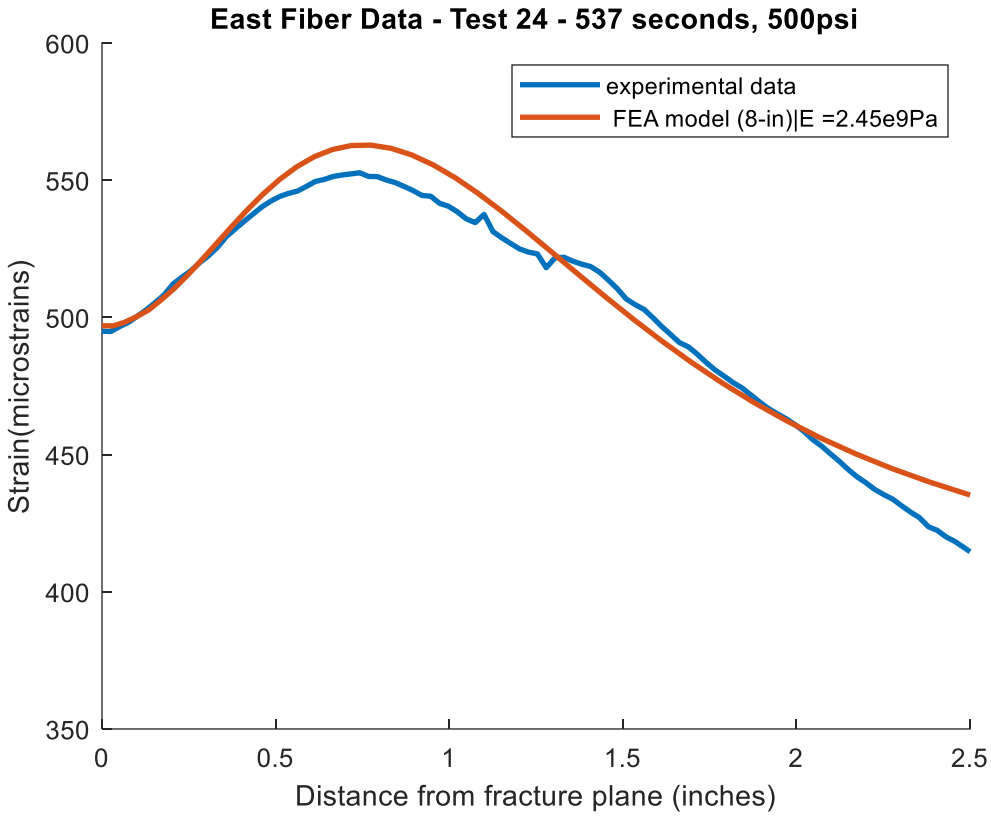

Figure 3.39 Modeled strain response (orange) compared to the experimental data (blue) using the finite element model.

4. CONCLUSIONS AND FINAL REMARKS

4.1. Conclusions

Low frequency distributed acoustic sensing was utilized in the laboratory setting to study the offset strain response to a propagating fracture with shear and normal stresses. The learnings of this work are listed below.

1. The LF-DAS response to a propagating fracture with shear and normal stresses on the plane that passes the fiber through an angled fracture experiment with a uniaxial load was successfully performed in a laboratory setting with an 8-inch cube of epoxy and embedded high-definition fiber optic cables.
2. The asymmetrical strain response over the fracture plane highlights the impact of the shear response when compared to previous experiments that claimed a symmetrical response with the presence of a purely normal stress.
3. The convergence of the heart-shape extension pattern on the LF-DAS waterfall plot for the fracture hit well aligned with the experimentally observed time of the fracture hit.
4. The zero-strain location method was also applied and to the experimental data and well-predicted the fracture radius and distance to the front using the strain data from the embedded fiber intersected by the fracture.

Furthering the understanding of LF-DAS enhances the technology as a diagnostic tool for optimizing hydraulic fracturing to produce in unconventional reservoirs.

4.2. Limitations of Work

The project limitations include that this work has been validated for a single experiment at a 5-degree angle from the vertical plane normal to the applied load. Further work may consist of varying the angle to further explore how that impacts the LF-DAS response. Additionally, this work is applied with a uniaxially-confined cube of epoxy; in the field, the reservoir is not uniaxially compressed. However, in the lab setting we are able to understand all of the boundary conditions introduced to diagnose the LF-DAS response as a function of known conditions. Lastly, the experimental findings have not yet been validated with a field case study. However, literature has suggested the asymmetrical LF-DAS responses to an angled propagating fracture (Shahri et al., 2021) and the zero-strain location model were previously validated (Leggett et al., 2022).

4.3. Final Remarks

This work has continued to shed light on the capabilities of LF-DAS applications for optimization of unconventional reservoirs. An extension of this research is to modify the angle of the fracture plane or adjust the magnitude of the applied load to create an altered extent of the shear and normal stress on the fracture plane. To increase the knowledge surrounding LF-DAS in practical applications, a multi-fracture experiment could be conducted. This would represent a two-cluster design in unconventional completions. Lastly, the ability for fiber optics to tell a story about the subsurface is changing the way operators are spending their capital and making an impact around the world.

REFERENCES

2018. Abaqus FEA, Dassault Systemes (Reprint). https://www.3ds.com/products-services/simulia/products/abaqus/.

2022. ODiSI V2.3.4 edition, LUNA (Reprint).

Chavarria, J. A., Ugueto, G., Oukaci, Y., & Laflame, L. (2022). *Assessing Single and Multiwell Fiber Optic Data for Microseismic Monitoring: An Example from HFTS2*. Paper presented at the SPE/AAPG/SEG Unconventional Resources Technology Conference. https://doi.org/10.15530/urtec-2022-3722235.

Chen, Z., Zhou, L., Walsh, R., & Zoback, M. (2018). *Case Study: Casing Deformation Caused by Hydraulic Fracturing-Induced Fault Slip in the Sichuan Basin*. Paper presented at the SPE/AAPG/SEG Unconventional Resources Technology Conference. https://doi.org/10.15530/URTEC-2018-2882313.

Cipolla, C., Wolters, J., McKimmy, M., Miranda, C., Hari-Roy, S., Kechemir, A., & Gupta, N. (2023). Observation Lateral Project: Direct Measurement of Far-Field Drainage in the Bakken. *SPE Production & Operations*, *38*(01), 20-34. doi:10.2118/209164-PA.

EIA. (2022). *Annual Energy Outlook*. Retrieved from https://www.eia.gov/outlooks/aeo/pdf/AEO2022_ChartLibrary_full.pdf.

ExxonMobil. (2022). *2022 Outlook for Energy*. Retrieved from https://corporate.exxonmobil.com/-/media/global/files/outlook-for-energy/2022/2022-exxonmobil-outlook-for-energy-executive-

summary.pdf?la=en&hash=C4942428B3F8375A47BB88122E148156DA38F6CA.

Gutierrez, G., Ramirez, L., Sierra, J. R., Medina, E., Gutierrez, L. J., & Salguero, J. (2014). *Improvements in Multistage Fracturing, Remolino Field, Mexico*. Paper presented at the SPE Hydraulic Fracturing Technology Conference. https://doi.org/10.2118/168576-MS.

Haustveit, K., Elliott, B., Haffener, J., Ketter, C., O'Brien, J., Almasoodi, M., . . . Deeg, W. (2020). *Monitoring the Pulse of a Well Through Sealed Wellbore Pressure Monitoring, a Breakthrough Diagnostic With a Multi-Basin Case Study*. Paper presented at the SPE Hydraulic Fracturing Technology Conference and Exhibition. https://doi.org/10.2118/199731-MS.

Haustveit, K., Elliott, B., & Roberts, J. (2022). *Empirical Meets Analytical-Novel Case Study Quantifies Fracture Stress Shadowing and Net Pressure Using Bottom Hole Pressure and Optical Fiber*. Paper presented at the SPE Hydraulic Fracturing Technology Conference and Exhibition. https://doi.org/10.2118/209128-MS.

Jin, G., & Roy, B. (2017). Hydraulic-fracture geometry characterization using low-frequency DAS signal. *The Leading Edge, 36*, 975-980. doi:10.1190/tle36120975.1.

Karrenbach, M., Cole, S., Ridge, A., Boone, K., Kahn, D., Rich, J., . . . Langton, D. (2019). Fiber-optic distributed acoustic sensing of microseismicity, strain and temperature during hydraulic fracturing. *GEOPHYSICS*.

Kerr, E., Haustveit, K., Scofield, R., Estrada, E., Johnson, A., Galuska, S., . . . Landry, M. (2022). *Multi-Pronged Diagnostics with Modeling to Improve Development Decisions-An Operator Case Study*. Paper presented at the SPE Hydraulic Fracturing Technology Conference and Exhibition. https://doi.org/10.2118/209140-MS.

Krohn, D. A., MacDougall, T., & Mendez, A. (2015). *Fiber optic sensors: Fundamentals and applications: Fourth edition*.

Leggett, S. (2022). *Investigations of the Low-Frequency Distraibuted Acoustic Sensing Response to a Propagating Hydraulic Fracture*. Petroleum Engineering. Texas A&M University.

Leggett, S., Reid, T., Zhu, D., & Hill, A. D. (2022). Experimental Investigation of Low-Frequency Distributed Acoustic Strain-Rate Responses to Propagating Fractures. *SPE Journal, 27*(06), 3814-3828. doi:10.2118/209135-PA.

Leggett, S., Sakaida, S., Zhu, D., Hill, A. D., & Kerr, E. (2023). *Interpretation of Fracture Initiation Points by in-Well LF-DAS in Horizontal Wells*. Paper presented at the SPE Hydraulic Fracturing Technology Conference and Exhibition. https://doi.org/10.2118/212328-MS.

Molenaar, M. M., & Cox, B. E. (2013). *Field Cases of Hydraulic Fracture Stimulation Diagnostics Using Fiber Optic Distributed Acoustic Sensing (DAS) Measurements and Analyses*. Paper presented at the SPE Unconventional Gas Conference and Exhibition. https://doi.org/10.2118/164030-MS.

Pudugramam, S., Irvin, R. J., McClure, M., Fowler, G., Bessa, F., Zhao, Y., . . . Zoback, M. D. (2022). *Optimizing Well Spacing and Completion Design Using Simulation Models Calibrated to the Hydraulic Fracture Test Site 2 (HFTS-2) Dataset*. Paper presented at the SPE/AAPG/SEG Unconventional Resources Technology Conference. https://doi.org/10.15530/urtec-2022-3723620.

Raterman, K., Liu, Y., Roy, B., Friehauf, K., Thompson, B., & Janssen, A. (2020). *Analysis of a Multi-Well Eagle Ford Pilot*. Paper presented at the SPE/AAPG/SEG Unconventional Resources Technology Conference. https://doi.org/10.15530/urtec-2020-2570.

Richter, P., Parker, T. E., Woerpel, C., Wu, Y. G., Rufino, R., & Farhadiroushan, M. (2019). Hydraulic fracture monitoring and optimization in unconventional completions using a high-resolution engineered fibre-optic Distributed Acoustic Sensor. *First Break.*

Salah, M., Gabry, M., & El-Sebaee, M. (2017). *Evaluation of Multistage Fracturing Stimulation Horizontal Well Completion Methods in Western Desert, Egypt*. Paper presented at the SPE Middle East Oil & Gas Show and Conference. https://doi.org/10.2118/183785-MS.

Shahri, M., Tucker, A., Rice, C., Lathrop, Z., Ratcliff, D., McClure, M., & Fowler, G. (2021). *High Fidelity Fibre-Optic Observations and Resultant Fracture Modeling in Support of Planarity*. Paper presented at the SPE Hydraulic Fracturing Technology Conference and Exhibition. https://doi.org/10.2118/204172-MS.

Smith, M. B., & Montgomery, C. T. (2015). *Hydraulic fracturing*: CRC Press.

Sneddon, I. N. (1946). The distribution of stress in the neighbourhood of a crack in an elastic solid. *Proceedings of the Royal Society of London. Series A. Mathematical and Physical Sciences, 187*, 229 - 260.

Ugueto, G. A., Todea, F., Daredia, T., Wojtaszek, M., Huckabee, P. T., Reynolds, A., . . . Chavarria, J. A. (2019). *Can You Feel the Strain? DAS Strain Fronts for Fracture Geometry in the BC Montney, Groundbirch*. Paper presented at the SPE Annual Technical Conference and Exhibition. https://doi.org/10.2118/195943-MS.